공학박사 학위논문

Structural Refinement Using Nanowire and Micro-patterned Substrate for Si- or Sn-based Li-alloying Material in Li-ion Batteries

리튬 이온 전지용 실리콘 혹은 주석계 리튬 합금 물질을 위한
나노 와이어 및 마이크로 패턴 기판을 이용한 구조 개선

2017년 8월

서울대학교 대학원

화학생물공학부

김 명 호

Structural Refinement Using Nanowire and Micro-patterned Substrate for Si- or Sn-based Li-alloying Material in Li-ion Batteries

리튬 이온 전지용 실리콘 혹은 주석계 리튬 합금 물질을 위한
나노 와이어 및 마이크로 패턴 기판을 이용한 구조 개선

지도교수 김 재 정

이 논문을 공학박사 학위논문으로 제출함
2017년 5월

서울대학교 대학원
화학생물공학부
김 명 호

김명호의 공학박사 학위논문을 인준함
2017년 6월

위 원 장 ＿＿＿＿＿＿＿ (인)

부 위 원 장 ＿＿＿＿＿＿＿ (인)

위 원 ＿＿＿＿＿＿＿ (인)

위 원 ＿＿＿＿＿＿＿ (인)

위 원 ＿＿＿＿＿＿＿ (인)

ABSTRACT

As demand for environmental-friendly energy and high energy density has increased, research on Li-ion batteries has been actively carried out. Graphite (372 mAh/g), which is widely used, has a relatively low capacity as an anode, thus it is highly possible to increase the capacity of anode. For this purpose, studies on alloying materials with high capacity have been conducted, but the main issue was deterioration of the electrode due to the severe volume change. So, various attempts have been made to reduce this deterioration phenomenon by manufacturing nano-sized particles, rods, tubes and relaxing the stress induced by volume change to create space between the active materials. However, these approach had also required the addition of large amounts of conducting agent and binder to maintain the contact between the active materials, thereby lowering the energy density. In addition, the self-aggregation occurred due to the high surface energy which leaded to increase the size of the particles and as the number of contacts between the active materials increased, the contact resistance became large, which was a disadvantage for conductivity. In this study, to overcome these problems, the electrode was fabricated using Si (4200 mAh/g) and Sn (994 mAh/g) which showed large capacity among alloying materials, and structural refinement was carried out to enhance the

characteristics.

Microelectromechanical system process, which is mainly used in semiconductor processing, was applied to make micro-sized sawtooth and pyramid-like patterns on the Si wafer substrate. The substrates with sawtooth and pyramid-like patterns showed the increased surface area by 10% and 40%, respectively. On the substrate, Si active material was deposited in the form of a film by physical vapor deposition method. Stress induced during cycling was relieved in the space of the pattern and the capacity retention increased by 500 mAh/g at 50th cycle. Furthermore, since the substrate shape was maintained during charging and discharging, the pattern effect could continuously alleviate the stress. Particularly, in the concave region of the pattern, the deterioration of active material was diminished, so that the coverage of the Si active material at 20th cycle reached 65% with the pyramid-patterned electrode and enhanced rate capability was obtained.

In addition, the nano-scale refinement with nanowire structure was attempted to improve cycle performance. In the case of nano-structure, instead of Si, which is difficult to handle structurally, Sn alloying material was used. CuO nanowires were prepared by anodization of Cu and Sn/CuO nanowire structure was fabricated by electrodeposition. Not only Sn but also CuO which can be used as an active material

in anode was also synthesized. CuO nanowires can increase the energy density of battery to eliminate conducting agent and binder. Moreover, one dimensional structure enhanced the electrical conductivity. Compared with Sn film electrodes, Sn/CuO nanowires electrode showed improved capacity retention, 89% up to 70th cycle. The rate capability of Sn/CuO nanowires electrode also showed about 56% at 16 C- rate.

However, deterioration of nanowire-structured electrode was observed in the long-term cycle. Up to 200th cycle, the specific capacity was maintained about 68%, and in particular, abrupt capacity fading was observed at 100th cycle. In the electrode manufacturing process, the nanowires were squeezed and pressed during the pressing process, and the structure of the nanowires was broken down during cycling. In order to improve this problem, the nanowires were fabricated on the patterned substrate previously made. As a result, the capacity retention was maintained at 92% up to 200th cycle and there was no rapid deterioration of the electrode. Through combination of micro-scale and nano-scale structure refinement for alloying material as anode in Li-ion batteries, it was possible to successfully improve the cell performance.

TABLE OF CONTENTS

LIST OF TABLES

LIST OF FIGURES

CHAPTER I. Introduction

1.1. Energy trend

Since the fossil fuel used as primary energy sources from the industrial revolution is prospectively limited and global warming due to greenhouse gas emissions has intensified, a number of energy sources have been researched to store and utilize efficient and nature friendly energy. Several kinds of systems including fuel cell, solar cell, battery, etc. have been developed, and batteries are one of the most widely used today. As shown in Figure 1.1, the battery performance was continuously developed to meet demand increasing volumetric and gravimetric energy density. In Table 1.1, the various types of secondary batteries and their chemistries are shown. Among them, Li-ion battery is one of the most widely used batteries in the real life because it has a high energy density and easily reacts at room temperature. Over the past several decades, electrode materials and packing technologies have been studied extensively to improve the performance of Li-ion batteries and they have now been nearly optimized for packing. In addition, research on energy storage systems that store over-produced power in batteries has been active. Therefore, the necessity of the electrode material having a high capacity for the improvement of the capacity

has arisen.
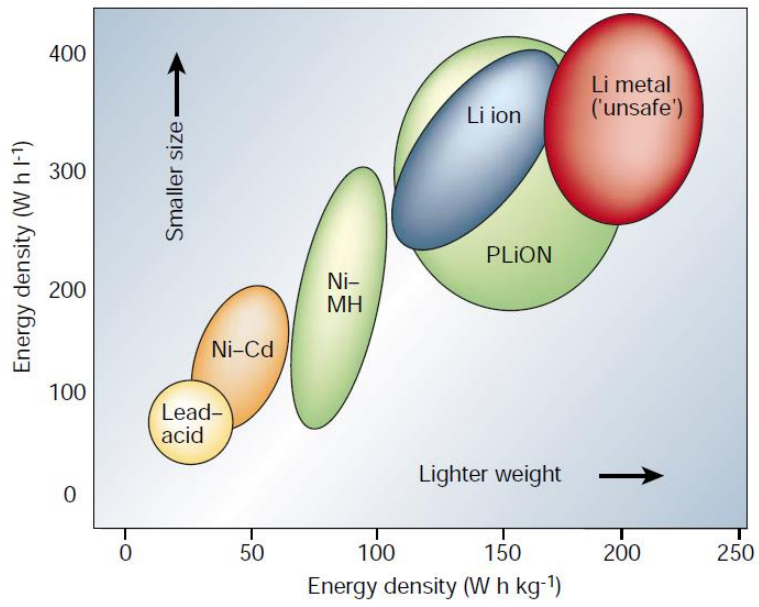
Figure 1.1. Comparison of various energy storage devices in terms of volumetric and

gravimetric energy density [1].

Table 1.1. Various Types of Secondary Batteries and Their Chemistries [2]

Table 1	Battery chemistries	
Battery type	**Features**	**Environmental impact**
Ni–MH (established)	Low voltage, moderate energy density, high power density Applications: portable, large-scale	Nickel not green (difficult extraction/unsustainable), toxic. Not rare but limited Recyclable
Lead–acid (established)	Poor energy density, moderate power rate, low cost Applications: large-scale, start-up power, stationary	High-temperature cyclability limited Lead is toxic but recycling is efficient to 95%
Lithium ion (established)	High energy density, power rate, cycle life, costly Applications: portable, possibly large-scale	Depletable elements (cobalt) in most applications; replacements manganese and iron are green (abundant and sustainable) Lithium chemistry relatively green (abundant but the chemistry needs to be improved) Recycling feasible but at an extra energy cost
Zinc–air (established)	Medium energy density, high power density Applications: large-scale	Mostly primary or mechanically rechargeable Zinc smelting not green, especially if primary Easily recyclable
Lithium–organic (future)	High capacity and energy density but limited power rate. Technology amenable to a low cost Applications: medium- and large-scale, with the exception of power tools	Rechargeable Excellent carbon footprint Renewable electrodes Easy recycling
Lithium–air (future)	High energy density but poor energy efficiency and rate capability Technology amenable to a low cost Applications: large-scale, preferably stationary	Rechargeability to be proven Excellent carbon footprint Renewable electrodes Easy recycling
Magnesium–sulphur (future)	Predicted: high energy density, power density unknown, cycle life unknown	Magnesium and sulphur are green Recyclable Small carbon footprint
Al–CF$_x$ (future)	Predicted: moderate energy density, power density unknown	Aluminium and fluorine are green but industries are not Recyclable
Proton battery (future)	Predicted: all organic, low voltage, moderate energy density, power density unknown	Green, biodegradable

1.2. History of battery

The term 'battery' was first used by Benjamin Franklin (1706 ~ 1790) in 1749. At that time, the generic meaning of battery was "a group of two or more similar objects functioning together" in an artillery battery in military organizations. He used 'battery' to express a set of linked capacitors. It came to be used for from the devices in which many electrochemical cells were connected together like Franklin's capacitors and even a single electrochemical cell as well. After that, the first true battery, voltaic pile, was invented by Alessandro Volta (1745 ~1827) in 1800. The voltaic pile consisted of a stack of copper and zinc plates with brine-soaked paper between the plates. It was able to produce continuous electricity and stable current, but there was a limit to get enough value of voltage. Also, it was not fully understood that the voltage was generated by the chemical reaction.

Since then, Daniell cell was invented by John Frederic Daniell (1790 ~ 1845) in 1836, which consisted of copper pot filled with a copper sulfate and earthenware container filled with sulfuric acid and a zinc electrode. The earthenware container was immersed in the copper pot. The Daniell cell made great strides in battery development in the early days and was the first battery as a practical source of

electricity. At anode and cathode, oxidation of zinc and reduction of copper occur per the following reactions:

(Eq 1.1) $Zn^{2+}(aq) + 2e^- \rightarrow Zn(s)$ $\qquad\qquad E^0 = -0.76\,V\ (vs.\,NHE)$

(Eq 1.2) $Cu^{2+}(aq) + 2e^- \rightarrow Cu(s)$ $\qquad\qquad E^0 = 0.34\,V\ (vs.\,NHE)$

(Eq 1.3) $Zn(s) + Cu^{2+}(aq) \rightarrow Zn^{2+}(aq) + Cu(s)$ $\qquad E^0_{cell} = 1.1\,V$
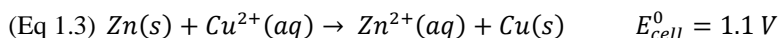
Since the electromotive force of the cell is $E_{cell} = E^c_{eq} - E^a_{eq}$, $E^0_{cell} = 0.34 - (-0.76) = 1.1\,V$ is obtained in standard state from above equations. On this occasion, Gibbs' free energy, $\Delta G^0 = -nFE^0_{cell}$ becomes negative, so that spontaneous zinc oxidation and copper reduction can occur. The operating voltage of the Daniell cell was used as the industry standard at that time.

As described above, a cell that generates electrical energy through an electrochemical reaction of compound only once is called a primary cell or primary battery. While a rechargeable battery which was also called by secondary battery or secondary cell can be charged and discharged many times. In 1859, the first rechargeable battery was invented by Gaston Planté (1834 ~ 1889) which was a lead-acid battery. It consisted of a lead anode and a lead dioxide cathode immersed in sulfuric acid.

(Eq 1.4) $PbSO_4(s) + 2e^- + H^+(aq) \rightarrow Pb(s) + HSO_4^-(aq)$

$$E^0 = -0.32\ V\ (vs.\ NHE)$$

(Eq 1.5) $PbO_2(s) + 3H^+(aq) + HSO_4^-(aq) + 2e^- \rightarrow PbSO_4(s) + 2H_2O(l)$

$$E^0 = 1.75\ V\ (vs.\ NHE)$$

(Eq 1.6) $Pb(s) + PbO_2(s) + 2H_2SO_4(l) \rightarrow 2PbSO_4(s) + 2H_2O(l)$
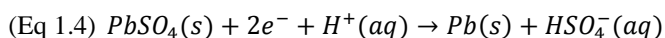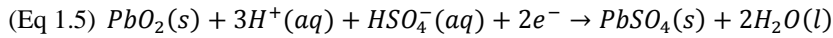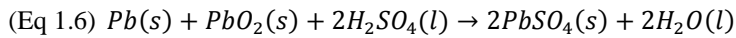
$$E^0_{cell} = 2.07\ V$$

Despite of a low energy-to-weight ratio, high current can be obtained with large power-to-weight ratio. So, this cell was used in automobile starter motor requiring high current. In 1899, the nickel-cadmium (Ni-Cd) battery was invented by Waldemar Jungner (1869 ~ 1924). It was widely used because of its relatively long cycle life and high reliability. The half reactions at each electrode are shown as in the following:

(Eq 1.7) $Cd(OH)_2(s) + 2e^- \rightarrow Cd(s) + 2OH^-(aq)$ $\quad E^0 = -0.81\ V\ (vs.\ NHE)$

(Eq 1.8) $2NiOOH(s) + 2H_2O(l) + 2e^- \rightarrow 2Ni(OH)_2(s) + 2OH^-(aq)$

$$E^0 = 0.47\ V\ (vs.\ NHE)$$

(Eq 1.9) $Cd(s) + 2NiOOH(s) + 2H_2O(l) \rightarrow 2Cd(OH)_2(s) + 2Ni(OH)_2(s)$
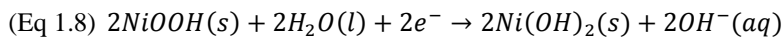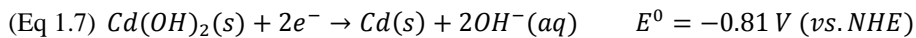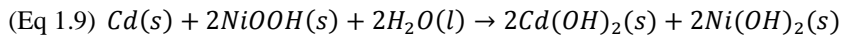
$$E^0_{cell} = 1.28\ V$$

However, the memory effect of the battery was observed. The memory effect was phenomenon that when the battery was repeatedly charged while being partially

discharged, the maximum capacity couldn't be obtained and the capacity gradually

decreased. The exact mechanism of memory effect was unknown, but it was

presumably due to the crystal growth of Cd and the formation of Ni-Cd alloy formed

on the negative electrode. This problem was solved by nickel-metal hydride (Ni-MH)

battery in 1989. Ni-MH battery was analogous to Ni-Cd battery with the exception

of using a hydrogen-absorbing alloy as a negative electrode. At negative electrode,

the following half reaction occurred during discharge:

(Eq 1.10) $M(s) + H_2O(l) + e^- \rightarrow MH(s) + OH^-(aq) \quad E^0 = -0.83\,V\,(vs.\,NHE)$
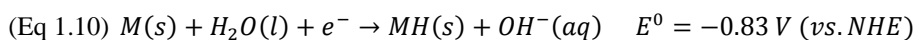
where MH(s) is the metal alloy in which hydrogen is stored, and M(s) is the alloy in

which hydrogen is desorbed. Although it showed the problem of an inadequate

charging ability at high rate owing to adsorption of hydrogen at metal alloy,

technological advances solved this problem. So, Ni-MH battery was used as a power

source for portable electronic devices and hybrid electric vehicles. Nevertheless, the

market share has gradually been decreased due to the emergence of Li-ion battery.

Li is the lightest metal and has the lowest standard reduction potential. So it is

very attractive material in terms of energy. In 1912, Gilbert Newton Lewis (1875 ~

1946) conducted the first Li battery-related experiments and Li metal battery was

first commercialized in the 1970s. Thereafter, attempts have been made for

secondary batteries using Li metal, but there was a problem that Li-ions were reduced with dendrite shape on the surface of the Li anode during charge and discharge cycle leading to the electrical short. So, various materials were studied as electrode materials. In 1980, as $LiCoO_2$ was invented by John Bannister Goodenough (1922 ~) and graphite for secondary battery was discovered by Rachild Yazami (1953 ~), Li-ion battery was commercialized by Sony in 1991. In the Li-ion battery, Li-ion was not reduced to Li metal, but charging and discharging proceeded through the reaction between the positive and negative electrode materials, thereby solving the short problem. Commercial Li-ion battery consisting of $LiCoO_2$ cathode and graphite anode follows below reaction at each electrode.

(Eq 1.11) $CoO_2(s) + Li^+ + e^- \rightarrow LiCoO_2(s)$ $\quad\quad\quad$ $E \approx 4.2\ V\ (vs.\ Li/Li^+)$

(Eq 1.12) $C_6(s) + Li^+ + e^- \rightarrow LiC_6(s)$ $\quad\quad\quad\quad$ $E \approx 0.05\ V\ (vs.\ Li/Li^+)$
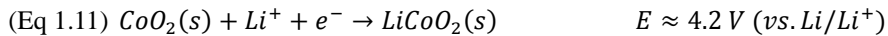
The standard reduction potential is generally shown based on the NHE, but in the Li-ion battery, the reaction potential is compared with the standard reduction potential of Li. So, the lithiation potential of CoO_2 can be expressed as ~1.16 V (vs. NHE) as well as ~4.2 V (vs. Li/Li$^+$). $LiCoO_2$ reversibly reacts with Li to Li_xCoO_2 (0.5 $\leq$ x $\leq$ 1) and the theoretical capacity is ~140 mAh/g. Graphite forms LiC_6 and has a capacity of 372 mAh/g. Recently, various types of batteries such as a solar cell, a

fuel cell, a Li-air battery, and a Na-ion battery are being studied as a next-generation

battery.

1.3. Li-ion battery

Li-ion batteries are one of the most widely used these days and intensively investigated to extend range of application. Such Li-ion battery is mainly composed of cathode, anode, electrolyte, and separator. Figure 1.2 shows the schematic of Li-ion battery system. At discharging, the Li-ions are extracted from positive electrode and inserted to the negative electrode through the electrolyte and separator. When charging, the Li-ions move in reverse. Before describing each component, it is necessary to sort out some terms. In secondary battery, the terms of cathode and anode can be confused because they are switched during charging and discharging. So, from now on, the terms of cathode and anode will be used based on discharge state. Then, the anode means the negative electrode.

1.3.1. Cathode

Cathode is an electrode having a higher reaction potential with Li-ion among the two electrodes. The cathode is mainly composed of transition metal oxide and there are layer, spinel, and olivine according to the structure, as shown in Figure 1.3.

$LiCoO_2$ and $LiNiO_2$ are typical layered metal oxide. In the layered structure, the Li-ions are positioned between the layered metal oxides and had 2-D diffusion pathway. Depending on the transition metal in the Li metal oxide, electrode has various characteristics. $LiNiO_2$ has the theoretical specific capacity about 20% larger than that of $LiCoO_2$. However, there is a problem that Ni-ion moves to the Li position due to similar ion size and blocks the Li-ion path way [5]. So, $LiCoO_2$ having good cycle performance is widely used although Co is expensive and toxic [6].

$LiMn_2O_4$ has spinel structure which gives Li-ion to 3-D space, so it shows high electrical conductivity. However, dissolution of Mn-ion to electrolyte was observed during cycling resulting in decrement of capacity. To solve this dissolution problem, studies have been carried out to replace some Mn with Ni, Co, and Al. Among them, $LiNi_{0.5}Mn_{1.5}O_4$ shows high potential of Li reaction [7,8]. $LiMePO_4$ (Me = Fe, Mn, Co, Ni) have the olivine structure. It has 1-D Li-ion pathway, so it shows low electrical conductivity. In order to improve the performance, carbon coating or metal coating has been investigated [10].

1.3.2. Anode

Li metal was used as an anode for the first time in Li primary battery. Li is an alkaline metal that has the lowest atomic number in periodic table and theoretically has a high energy density of 3830 mAh/g due to the reaction potential matched with Li-ion itself. However, during charging and discharging, Li-ions have been found to grow in the form of dendrite on the Li metal, causing electrical short passing through the separator. The safety of Li metal batteries has been developed, and eventually Li-ion batteries came into the world. Unlike a Li metal battery, a Li-ion is not reduced during charging and discharging, just passing between a cathode and an anode in the form of Li-ion. This is called rocking chair mechanism as shown in Figure 1.2. The first commercialized anode in Li-ion battery was a graphite. The graphite electrode had a small volume change about 10% during cycling and the capacity retention was also excellent, so it was successfully commercialized. The theoretical specific capacity of graphite is 372 mAh/g which is low compared with other anode materials.

In its early years, Li-ion batteries were applied to portable devices and small-sized devices. However, it was required increasingly higher energy to apply to electric vehicles and energy storage systems. Therefore, anode materials with high capacity are actively investigated. Representatively, there are three reactions with Li-ion which are insertion, conversion, and alloying reaction. The three reactions can be

expressed as following equations.

(Eq 1.13) Insertion reaction: $Li + MX_2 \rightarrow LiMX_2$

(Eq 1.14) Conversion reaction: $2Li + MX \rightarrow Li_2X + M$

(Eq 1.15) Alloying reaction: $xLi + M \rightarrow Li_xM$
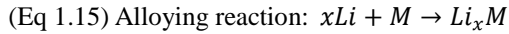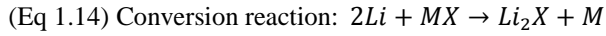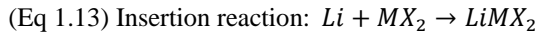
Figure 1.4 exhibits the schematics of the three reactions. The alloying materials include Si (4200 mAh/g for $Li_{4.4}Si$) [11-16], Sn (994 mAh/g for $Li_{4.4}Sn$) [17-20], Ge (1600 mAh/g for $Li_{4.4}Ge$) [21], Sb (660 mAh/g for Li_3Sb) [22], and Bi (386 mAh/g for Li_3Bi) [23]. Among them, Si has the largest specific capacity for alloying materials with up to 4.4 Li-ions and the theoretical specific capacity is about 4200 mAh/g. Si reacts with Li-ion to form several phases with $Li_{12}Si_7$, $Li_{14}Si_6$, $Li_{13}Si_4$, $Li_{15}Si_4$, $Li_{22}Si_5$ at high temperature, whereas it is hard to make $Li_{22}Si_5$ phase in room temperature, so the reaction takes place up to $Li_{15}Si_4$ in practice (theoretical capacity: 3580 mAh/g) [24]. However, as the capacity is large, the volume change is also serious due to the alloy reaction with Li-ion, and the volume is expanded up to 300% at fully lithiated state [25]. The stress formed by the volume change needs to be relaxed because it leads to the degradation of the electrode, and a lot of research has been carried out. Generally, if the surface area is wide, the amount of active material to be loaded per area decreases, so that the absolute volume change can be reduced.

1 4

Based on this, there are many studies on the formation of nano-structures such as nanoparticle [26], nanowire [27-29], 3-D hollow structure [30], and porous structure [31,32], etc. Sn has been also actively studied due to its high theoretical capacity. Sn also reacts with Li-ion to form various phases with Li_2Sn_5, Li_7Sn_3, Li_5Sn_2, $Li_{13}Sn_5$, Li_7Sn_2, $Li_{22}Sn_5$ [33]. Compared with Si, Sn has a good electrical conductivity and low melting point, so it is easy to synthesize and operate.

1.3.3. Separator

A separator is a membrane located between positive and negative electrodes preventing contact (short circuit) of active materials of each electrode and allows the transport of ionic charge carriers. It has microporous structure and the ion moves through the pore space. The separator must have various properties in the battery, which are chemical stability, mechanical property, thinness, current shutdown capability, and electrolyte holding capacity. Representatively, polyethylene microporous membranes are widely used as separator. Following equation shows the resistance that affects battery performance.

(Eq 1.16) $R_{total} = R_{solution} + R_{separator} + R_{circuit}$

Among them, $R_{separator}$ is the most dominant. So, in terms of resistance and energy density, the thickness of the separator is preferably small. However, it should have adequate thickness for safety and generally has a thickness of 15 ~ 30 μm. The multilayer membrane of polyethylene-polypropylene is widely used because polypropylene has good mechanical property.

1.3.4. Electrolyte

Electrolyte acts as a channel for Li-ions between the positive and negative electrodes of the cell and forms a close loop with the external circuit. The electrolyte has to be ionically conductive and electronically insulating. Also, in order to lower the overpotential, η, that occurs during charging and discharging, it is better to use electrolyte with high ionic conductivity and dielectric constant. Furthermore, it must be electrochemically stable at the anode and cathode of the cell. The stability of the electrolyte is called an electrochemical stability window, which indicates that the electrolyte has a stable electrochemical potential range. In addition, it is required to meet wettability to polyolefin separator, low toxicity and low cost. The electrolyte consists of solvent and salt. Currently, the carbonate-based solvents are generally

used. However, it is impossible for a single solvent to meet high dielectric constant and low viscosity. So, the mixture of a cyclic carbonate (ethylene carbonate (EC) and propylene carbonate (PC)) possessing high dielectric constant with linear carbonate (dimethyl carbonate (DMC), ethylmethyl carbonate (EMC), and diethyl carbonate (DEC)) having low viscosity are used. The Li salt should dissolve well in the non-aqueous solvent. The fluorinated inorganic anions are preferred due to their high solubility, dissociation characteristics and passivation ability to positive electrode surface. The most widely used material among the Li slats is $LiPF_6$. However, fluorinated inorganic anion based Li salts are moisture sensitive and more reactive at high temperature. So, in the laboratory, an Ar-atmosphere glove box is used to prevent contact with oxygen and moisture in the air during cell preparation.

In general, the decomposition of the electrolyte can not be avoided because the operating potential range of the anode and cathode of the cell is not included in the electrochemical stability window described above. In the case of anode, the graphite undergoes the reaction around 0.15 V (vs. Li/Li^+) and out of the stable potential range of carbonate, so that the electrolyte is decomposed on the surface of the anode. Figure 1.5 shows various anode and cathode materials used in Li-ion batteries. The horizontal dot lines around 1 V and 4 ~ 5 V indicate electrochemical window

boundaries of standard electrolyte solutions. The lines also mean energy levels of

highest occupied molecular orbital (HOMO) and lowest unoccupied molecular

orbital (LUMO). The decompositions of electrolytes mostly occur during the first

several cycles of a cell and the decomposed compounds form passivating layer

between the electrode and the electrolyte. This layer was first called solid electrolyte

interphase (SEI) by Peled [35] and it has been found to have a significant effect on

the cell performance. Various additives are added to form a high-quality SEI, and

these additives were decomposed in a higher potential range than the electrolyte

forming a stable SEI [36].
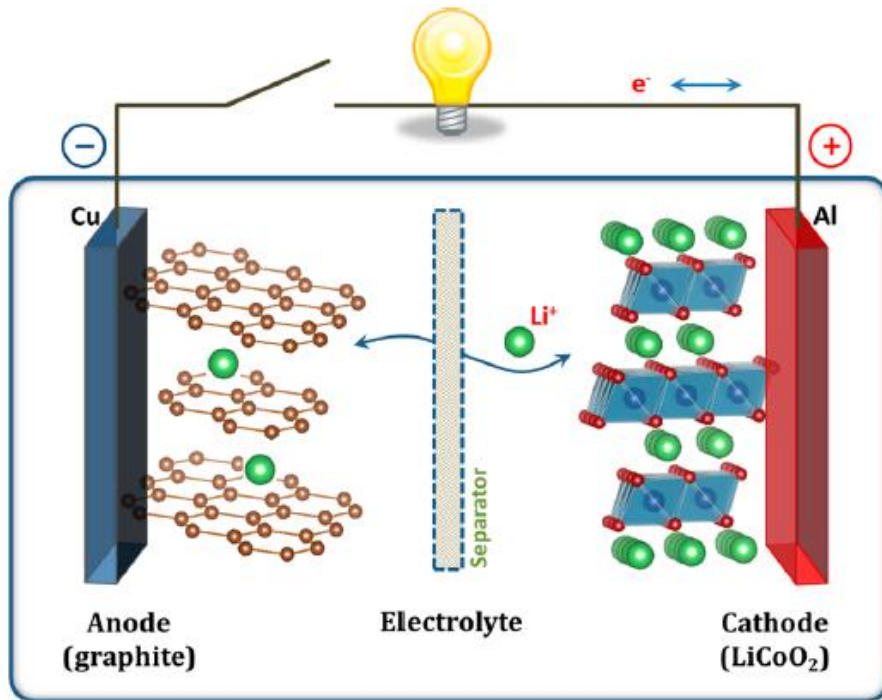
Figure 1.2. Schematic diagram of Li-ion battery with $LiCoO_2$ and graphite electrode

[3].
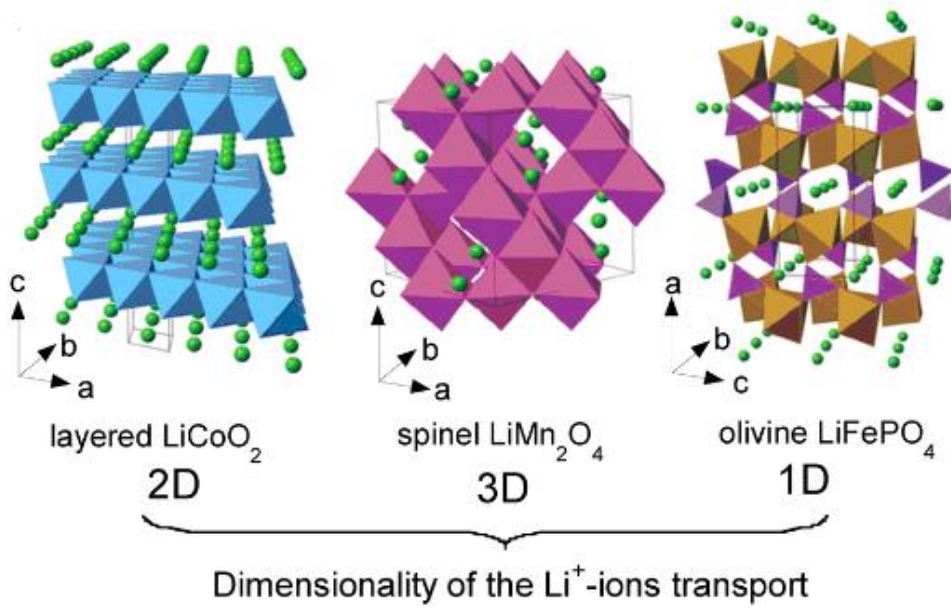
Figure 1.3. Crystal structures of layered $LiCoO_2$ (2-D), spinel $LiMn_2O_4$ (3-D), and

olivine $LiFePO_4$ (1-D) frameworks [4].
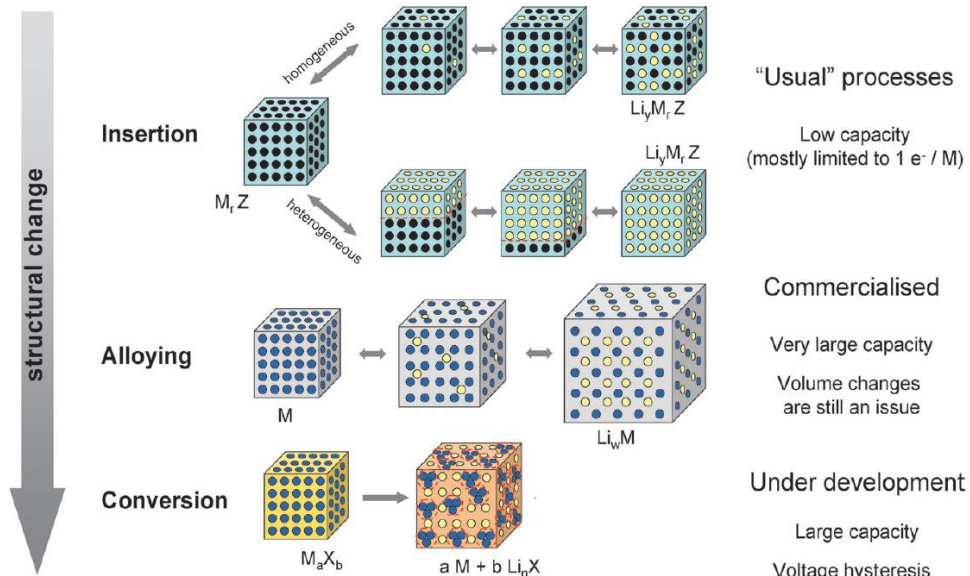
Figure 1.4. Schematic diagrams of insertion, alloying, and conversion reaction [9].
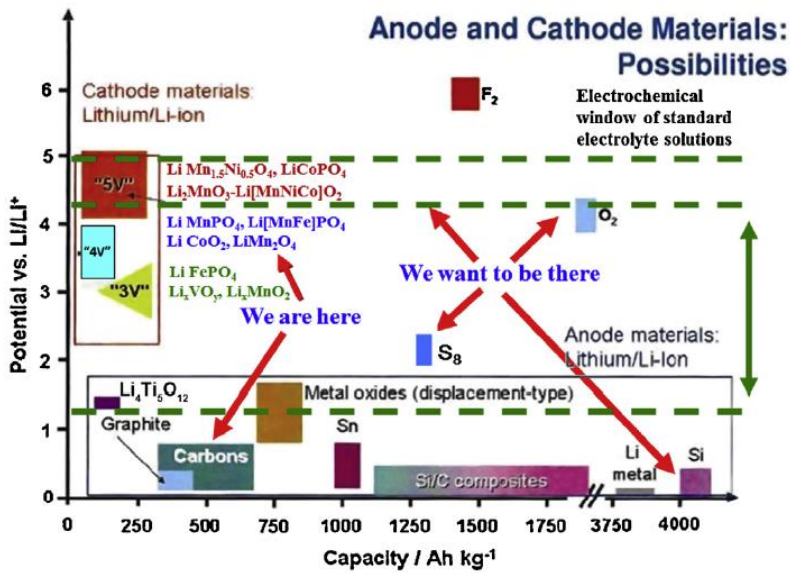
Figure 1.5. Various anode and cathode materials according to the theoretical specific

capacity and potential range reacting with Li-ions [34].

1.4. Microelectromechanical systems process

In order to alleviate the rapid degradation of the alloy material for anode described before, the micro-scale structure modification of anode was conducted by microelectromechanical systems (MEMS). MEMS is micrometer- or millimeter-scale fabrication techniques based on semiconductor process technology. In this study, these semiconductor processes to obtain patterned substrate and Si negative electrode were used. There are three steps of procedures which are deposition, patterning, and etching.

Deposition process is for obtaining the thin film. There are two main types of deposition which are chemical vapor deposition (CVD) and physical vapor deposition (PVD). CVD utilizes one or more volatile precursors reacting on the substrate surface. It shows low substrate damage, mass production, low cost, and proper step coverage. However, the harmful gases were used. By comparison, PVD is a vacuum deposition methods in which the materials go from a condensed phase to a vapor phase and then back to a thin film phase. The common PVD methods are sputtering and evaporation. In this research, the sputtering having the advantage of forming high quality film was focused. There are mainly two methods in sputtering,

radio frequency (RF) sputtering and direct current (DC) sputtering. RF sputtering

can use non-conductor target as well as conductors. Though DC sputtering restricted

to apply only conducting materials, it is very simple and easy to use. So, conductive

targets with DC sputtering was used. The principle of sputtering is that the target

metal is deposited by forming plasma in the vacuum chamber with Ar. Figure 1.6

shows the schematic diagram of DC sputtering equipment used in this study. The

system consists of pump, power supply, gun, target, substrate, gas system. Pump

adjusts the degree of vacuum in the chamber to create an environment for obtaining

plasma, and the power supply generates power to the cathode. Gun is the part where

water flows for the cooling of the target and connecting area between power supply

and target. Target is the materials to deposit on the substrate. Using the magnetron,

the yield of the DC sputtering can be improved by focusing the plasma.

Patterning is a method of forming a photoresist pattern on a Si wafer, mainly using

a photolithography process. Photolithography literally means making a shape like a

photograph. By creating a pattern of exposed or unexposed portions of the light,

pattern shape formed on the Si substrate. The procedures can be simplified as follows.

First, the substrate is cleaned to remove organic substances or impurities on the

surface. Then, a hexamethyldisilazane (HMDS) material is entirely coated on the

surface using a spin coater to improve adhesion between the substrate and photoresist. Then, photoresist is uniformly coated by spin coater with appropriate spin rate and loading amount according to the characteristics of photoresist. After photoresist coating, soft baking procedure is conducted to drive off excess photoresist solvent. After soft baking, the photoresist is exposed to UV light. Because the light pass through the photo mask, specific pattern area can be exposed. There are two types of photoresist, positive and negative. Positive photoresist becomes soluble in the developer after exposure to UV light. The photo-generated acid by UV light incapacitates photoresist component to be soluble in alkali developer. On the contrary, negative photoresist becomes insoluble in the developer after exposure to UV light. Negative photoresist makes crosslinking chain by UV light to create an insoluble structure. After developing using the suitable photoresist, the exposed substrate of Si oxide can be etched with etchant, so that desired pattern can be obtained. Finally, all remaining photoresist is removed by PR stripping and the substrate which was etched only at the desired region can be obtained.

Up to this point, Si oxide layer where pattern is engraved is blocking the surface of the Si substrate. To form final pattern shape on Si substrate, Si etching step is needed. There are two type of Si etching including dry etching and wet etching. The

dry etching uses plasma to anisotropically etch the substrate. In wet etching, liquid phase etchants are used immersing the wafer in the bath until the desired time. Generally, the etching conditions are generalized according to the kind of the substrate, the desired etching shape and size. In the case of Si oxide, etching is performed using a diluted hydrofluoric acid (HF) or buffered oxide etch (BOE) solution. Si is etched using nitric acid (HNO_3) + HF or potassium hydroxide (KOH). Selectivity and isotropy can be important parameters in etching, so it is needed to select etchant well matched in experimental condition.
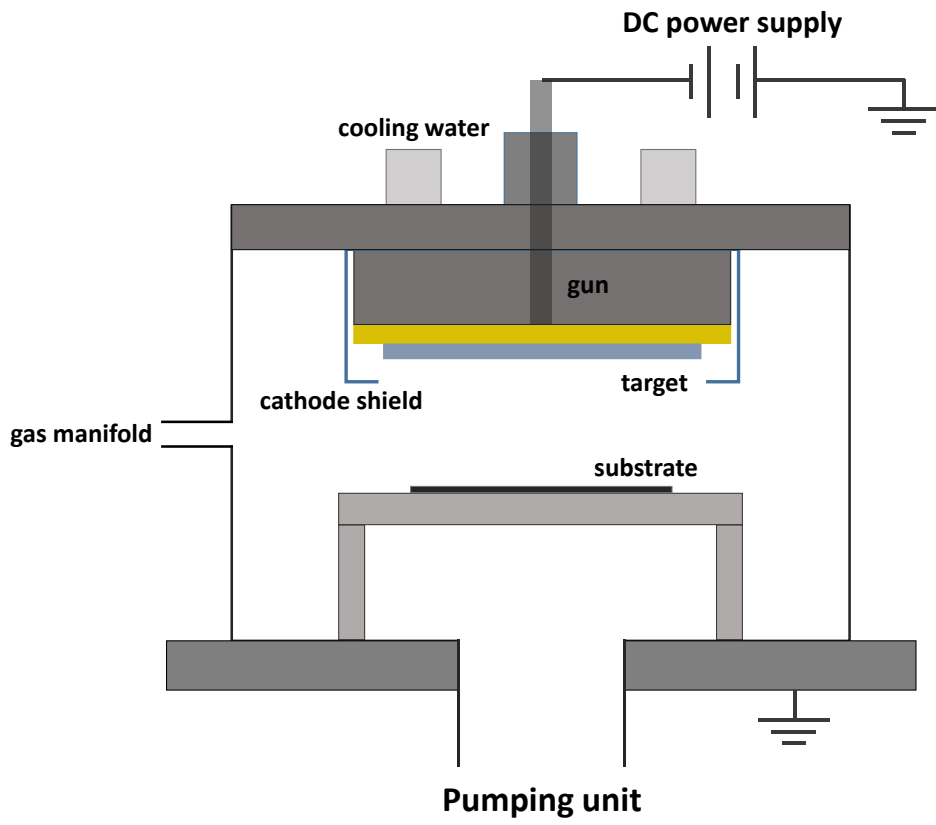
Figure 1.6. Schematic diagram of DC sputtering system.

1.5. Electrochemical process

Not only micro-scale modification with MEMS process but also nano-scale modification with nanowires structure was carried out using electrochemical process. Electrochemical methods refer to an oxidation or reduction reaction involving electrons. It has advantages of relatively simple control the reduction and oxidation reaction by potential or current. To form the nanowires structure of Sn material, Cu anodization and Sn electrodeposition were used. These two methods were controlled electrochemically by applied current.

Anodization of Cu in basic condition generated $Cu(OH)_2$ nanowires. Depending on the experimental conditions which are temperature, pH, electrolyte, potential, the various shapes of $Cu(OH)_2$, CuO, or Cu could be formed [37-52].Cu ions dissolved by oxidation current react with OH ions in the solution to form $Cu(OH)_2$. The $Cu(OH)_2$ converted to CuO with heat treatment by dehydration reaction.

Similar to Si, Sn is also one of the high-capacity alloying anode materials and environment-friendly, low-cost, and easy to handle. As mentioned earlier, however, pure Sn electrode expands nearly up to 300% during the insertion of Li-ion and it attributes to the pulverization and exfoliation of Sn. Ultimately the cell with Sn

electrode is likely to fade.

Sn is easily dissolved in the ionic state and reduced at room temperature to facilitate electrodeposition unlike Si, which requires high temperature (generally above 800°C). Sn could be electrodeposited evenly on the surface exposed to the solution. In addition, the morphology can be controlled by adjusting the current or voltage. Therefore, several studies have been conducted more flexibly than those using Si. Many approaches have been made to overcome the fading problems with Sn, including a nano-scale modification; nanoparticles [53-59], nanowires [60-66], composite [67-75], and nanoporous structure [76]. Based on these methods, in order to reduce the pulverization caused by volume change as mentioned above, a new type of Sn-based anode material having a heterogeneous nano-structure is proposed in this study; CuO nanowires decorated with Sn (Sn/CuO NWs). CuO has attracted much attention as anode material, owing to its moderate theoretical capacity (675 mAh/g), non-toxicity, and low price [77-84]. Unlike Sn or Sn oxide, the reaction of Li-ion with CuO is governed by a conversion mechanism, and thus it is relatively free of expansion. In addition, the efficient charge transfer is expected, due to intrinsic advantage of 1-D nano-material providing a direct electronic pathway connected to the current collector. Furthermore, the heterogeneous nano-structure

can manifest an additive- and binder-free electrode, leading to the high ratio of active material and enhancement of energy density. At last, the structure contributes to reduce the electrical resistance, due to formation of Cu nodes between CuO NWs with Sn. This can be accomplished because CuO at the marginal area of the nanowire is simultaneously reduced during Sn deposition. For above reason, CuO NWs as a structure framework as well as active material for Li-ion batteries was used. To be summarized, an effective fabrication of CuO NWs can lead to higher capacity and higher rate capability as an electrode for Sn, by reducing the over-potential and accelerating reaction kinetics at the electrode surface.

1.6. Purpose of this study

In this study, micro-scale and nano-scale refinement of substrate were introduced with microelectromechanical systems process and electrochemical methods. The improved cycle performance of alloying materials as anode was expected by forming nanowires structure on a patterned substrate. Sn/CuO NWs were fabricated by anodization on patterned substrate prepared by microelectromechanical systems process. The patterned substrate gave increased surface area and created a space which could alleviate the stress induced by volume change of active material during cycling. The nanowires structure synthesized by electrochemical methods had features the large surface area, the low electrical conductivity, and the high energy density by not using conductive agent and binder, so that good capacity retention and stable long-term cycling was expected.

CHAPTER II. Experimental

2.1. Preparation for Si patterned electrode

2.1.1. Preparation of patterned substrate

Double side polished p-type (110)- and (100)-oriented Si wafers were used. A Si oxide layer with 500 nm thickness was grown on surface of wafers by wet oxidation. The wafer was treated with sulfuric acid peroxide mixture (SPM; $H_2SO_4 : H_2O_2 = 4 : 1$ vol%) for 10 min at 120°C to eliminate the organic substances on the surface. Then, HMDS and positive photoresist (AZ 1512, AZ Electronic Materials) were coated onto the wafer in sequence by spin coating. After soft baking was conducted on hot plate for 30 s at 95°C, the wafer was exposed to UV light (365 nm, i-line) using aligner (MA-6 II, Karl-suss) for 15 s. Photo mask for sawtooth- and pyramidal-shape patterns was used for this process to transfer the pattern onto the wafer. To remove the exposed region of photoresist, the wafer was developed in the solution (AZ 300 MIF : D.I. water = 6 : 1 vol%) for 90 s and transferred to the hotplate and heated for additional 60 s at 95°C to enhance the rigidity of photoresist and adhesion with substrate. The patterns were formed using wet etching process. First, the exposed Si

oxide layer was etched with a buffered etch solution (BOE; $NH_4F : HF = 7 : 1$ vol%)

for 15 min. The residual photoresist on the wafer was removed by cleaning with

SPM solution for 10 min at 120°C. Second, Si was etched with 30 wt% KOH solution

for 50 min at 80°C. Prior to this, the native Si oxide layer was instantly etched by 1

vol% HF solution for 60 s. Finally, the residual oxide on the Si wafer was eliminated

by dipping itself in BOE solution for 15 min. The schematic diagram of MEMS

process is summarized in Figure 2.1.

2.1.2. Preparation of Si electrode

For using the patterned substrate as an electrode, it was cut into 1×1 cm^2 with a

dicing saw (DAD3350, Disco). Current collector and active material were prepared

by PVD. The patterned Si substrate was loaded in DC sputter chamber. The chamber

was vacuumed below 1.0×10^{-5} torr. Before sputtering, each target was pre-sputtered

for 2 min to remove oxides and other impurities presenting on the target surface. The

sputtering was conducted in order of TaN/Ta/TaN, Cu, and Si on the substrate. TaN

and Ta layers were sputtered alternatively at 500 V and 4 A in Ar : $N_2 = 4 : 1$ and Ar

atmosphere with 50 standard cubic centimeter per minute (sccm), so that

TaN/Ta/TaN layer as Cu diffusion barriers were deposited on both side of patterned

Si substrate. After that, Cu layer as a current collector was deposited on both side of

TaN/Ta/TaN layer deposited patterned Si substrate at 500 V and 4 A in Ar atmosphere.

Finally, Si layer as an active material was deposited on patterned surface at 600 V

and 2.5 A in Ar atmosphere. Figure 2.2 shows the schematic diagram of whole

process for patterned electrode preparation. To remove the residual water, the

electrodes were dried at 120°C for 12 h in vacuum oven before put into the glove

box.

  2032-type coin-cells with the plain (non-patterned), sawtooth, and pyramidal-

shape electrode were assembled in an Ar-filled glove box, as shown in Figure 2.3.

The different pattern sizes of sawtooth- (width of 85 and 170 μm) and pyramidal-

shape electrode (width of 50 and 100 μm) were prepared. The deposited amounts of

the Si on the electrodes were 0.15 mg/cm^2 in all the electrodes. Li metal foil (Cyprus)

and polypropylene–polyethylene–polypropylene (PP–PE–PP, Celgard) were used as

the counter electrode, and separator, respectively. The electrolytes used in this study

consisted of 1.3 M of LiPF$_6$ in ethylene carbonate (EC) : diethyl carbonate (DEC) at

a volume ratio of 3 : 7.

2.1.3. Electrochemical measurement and characterization

The electrochemical performance of the cell was measured using a cycler (Wonatech, WBCS-3000) at room temperature after 24 h of rest. The cycling behavior of Li/Si half-cell was performed at 0.1 C-rate for the formation step, followed by 0.5 C-rate for cycle step, where a 1 C-rate corresponds to the current density for an 1 hr fully charge or discharge. The boundaries of cut-off voltage during the cycle step was 0.08 and 1.4 V (vs. Li/Li$^+$), respectively. For analyzing the electrodes, the cells were disassembled in an Ar-filled glove box to block the contact with oxygen and water. The electrodes were rinsed with dimethyl carbonate (DMC) to remove the residual electrolyte and the salts on the surface. Field emission scanning electron microscope (FE-SEM, JEOL, JSM-6701F) was used to observe the surface and the cross-sectional images of the electrode before and after the cycling.

Si wafer

Thermal oxidation & Cleaning

PR coating (positive PR) & Soft baking

UV light

mask

Exposure

Development & Hard baking

Thermal oxide etching

Thermal oxide etching

Si etching

PR stripping
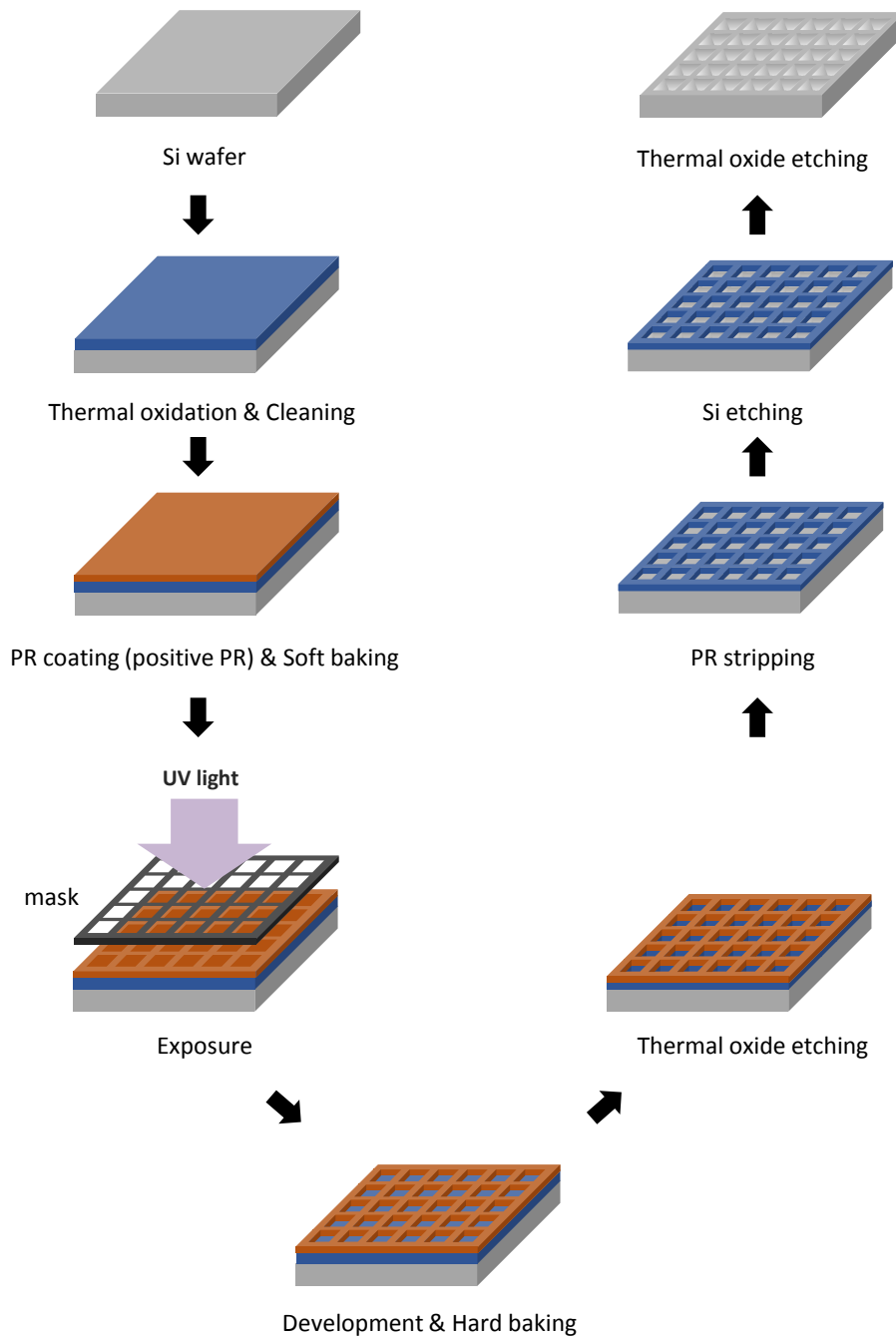
Figure 2.1. Schematic diagram of MEMS process for the fabrication of patterned Si

substrate.

3 6
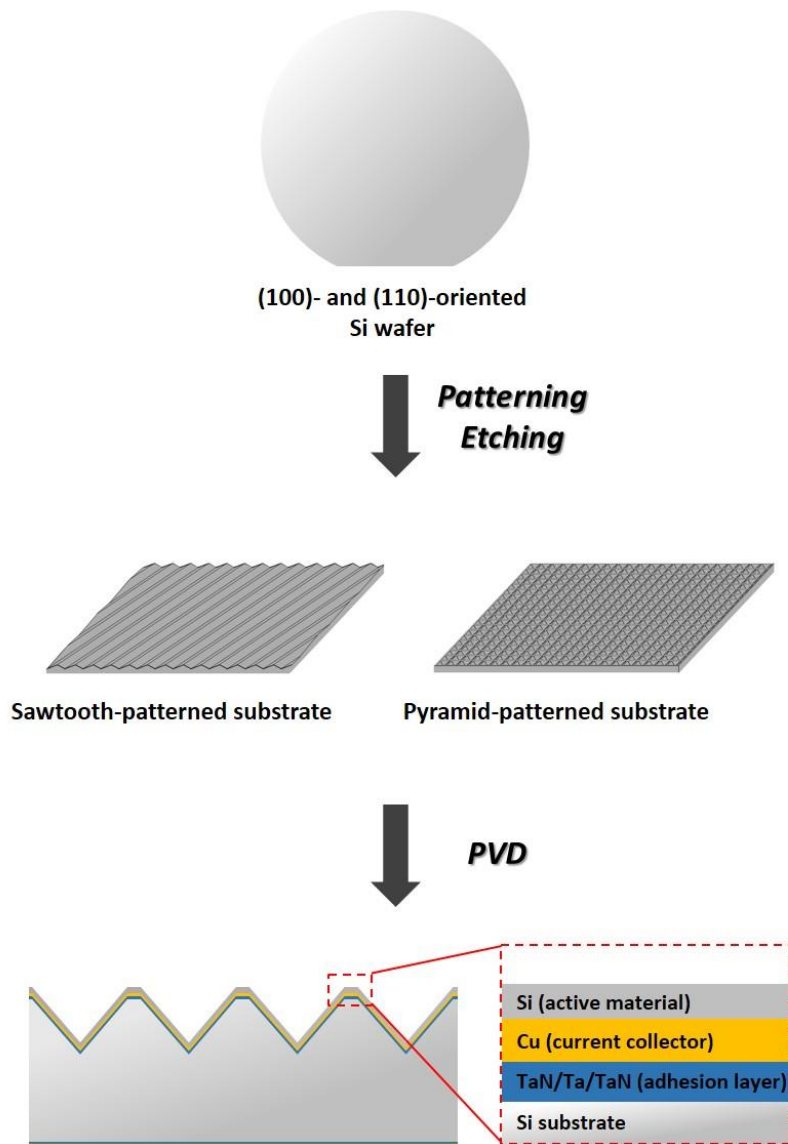
Figure 2.2. Schematic diagram of patterned electrode preparation by MEMS process.
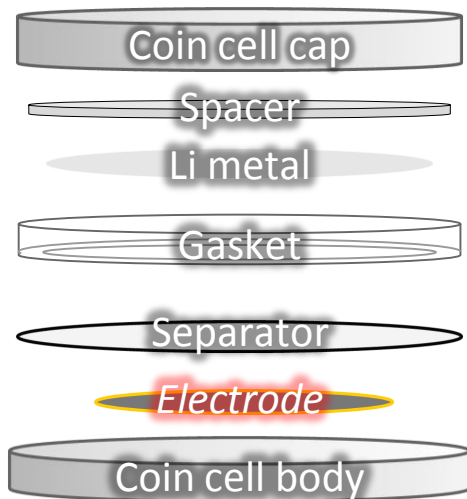
Figure 2.3. Schematic diagram of 2032 type cell made up of each component.

2.2. Synthesis of Sn/CuO nanowires electrode on Cu foil

2.2.1. Preparation of Sn/CuO nanowires electrode

Table 2.1 shows the abbreviations of terms appearing in this section for convenience. To form a 1-D NW structure, Cu foil (thickness = 10 μm) was anodized with three steps of galvanostatic methods in basic condition. 2 M of NaOH (Daejung, 98%) was dissolved in D.I. water and maintained at 5°C with stirring and N_2 gas purging for 1 hr. The three steps were applied with 5 mA/cm^2 for 10 s, -5 mA/cm^2 for 20 s, and 5 mA/cm^2 for 300 s, sequentially. After the three steps of galvanostatic methods, the f_Cu(OH)$_2$ NWs were electrode obtained. Pt mesh and Ag/AgCl (KCl sat.) were used as a counter electrode and reference electrode, respectively, as shown in Figure 2.4. The f_Cu(OH)$_2$ NWs electrode was rinsed with D.I. water for 15 s and blown with N_2 gas to remove the residual water. After heat treatment with 250°C for 1 hr in Ar atmosphere, the f_Cu(OH)$_2$ NWs was converted to f_CuO NWs with dehydration. Sn was electrodeposited on f_CuO NWs electrode with -10 mA/cm^2 for 50 s in the solution of 0.07 M of $Sn_2P_2O_7$ (Sigma Aldrich, 98%) and 0.36 M of $K_4P_2O_7$ (Sigma Aldrich, 97%) in D.I. water. After the Sn electrodeposition,

f_Sn/CuO NWs electrode was rinsed with D.I. water for 15 s and blown with N_2 gas.

A f_Sn film electrode was also prepared. Cu foil was pretreated with 0.5 M of H_2SO_4

(Daejung, 95%) for 1 min to eliminate the native oxide layer and rinsed with D.I.

water. With the solution of 0.07 M of $Sn_2P_2O_7$ and 0.36 M of $K_4P_2O_7$, Sn was

electrodeposited on Cu foil with -10 mA/cm^2 for 50 s. The electrodes were cut in the

diameter of 11 mm and dried at 120°C for 12 h under vacuum before put into glove

box to remove residual water.

2.2.2. Characterization and electrochemical measurement

The prepared samples were characterized by X-ray diffraction (XRD, Bruker D8-

Advance, Cu Ka, λ = 0.15406 nm) with a step rate of 2θ = 5 degrees/min. Field

emission scanning electron microscope (FE-SEM, JEOL, JSM-6701F) at 10 kV

accelerating voltage and energy-dispersive X-ray spectra (EDS, Oxford instruments

analytical, INCA Energy) were employed to observe the surface morphology and

composition of the electrode. For high magnitude image and lattice structure,

transmission electronic microscopy (TEM, JEOL, JEM-ARM200F) at 200 kV

accelerating voltage was conducted. The cross-sectional images were observed by

using an Ar-ion beam polisher (JSM-09010) with constant power of 0.5 W under vacuum condition below 2.0×10^{-6} torr. X-ray photoelectron spectroscopy (XPS, Thermo, Sigma probe) was carried out with Al Ka (1486.6 eV) anode operating at constant power of 100 W to assess the surface composition and chemical state. The amount of Sn and CuO were measured by inductively coupled plasma atomic emission spectroscopy (ICP-AES) using 1 vol% of HNO_3 for CuO dissolution and 2 vol% of aqua regia (HNO_3 : HCl = 3: 1 vol%) for Sn dissolution.

The 2032-type coin-cell was assembled in Ar-atmosphere glove box. Li metal foil (Cyprus) as a counter electrode and polypropylene-polyethylene-polypropylene (PP-PE-PP, Celgard) of multilayer separator were used. A mixture of 1.3 M of $LiPF_6$ in ethylene carbonate (EC) and diethyl carbonate (DEC) at a ratio of 3:7 vol% was used as the electrolyte solution. The electrochemical behavior of the cell was monitored using a cycler (Wonatech, WBCS-3000) at 25°C after impregnation of electrolyte for 24 hr. The cycling of the cell was performed at 0.1 C-rate for the formation cycle, followed by 1 C-rate cycling. The regions of cut-off voltages during cycling were between 0.01 and 3.0 V (vs. Li/Li^+). The cyclic voltammetry (CV) were carried out at a scan rate of 0.1 mV/s between 0.01 and 3.0 V (vs. Li/Li^+). Electrochemical impedance spectra (EIS, Princeton Applied Research, Parstat 2273) were measured

in the frequency range from 0.01 Hz to 100 kHz with an AC voltage amplitude of 5 mV. The rate capability test was also conducted from 0.1 C to 16 C-rate for 5 cycles at each rate condition. After electrochemical observation, the cells were dismantled in an Ar-filled glove box to prevent the reaction with oxygen and water in atmosphere. The electrodes were rinsed with dimethyl carbonate (DMC) to remove the residual electrolyte and salts on the electrode surface.

Table 2.1. The Abbreviations of Nanowire, Sn Film on Cu Foil, Cu(OH)$_2$ Nanowires on Cu Foil, CuO Nanowires on Cu Foil, and Sn-electrodeposited CuO Nanowires on Cu Foil

Abbreviation	Explanation
NW	nanowire
f_Sn film	Sn film on Cu foil
f_Cu(OH)$_2$ NWs	Cu(OH)$_2$ nanowires on Cu foil
f_CuO NWs	CuO nanowires on Cu foil
f_Sn/CuO NWs	Sn-deposited CuO nanowires on Cu foil
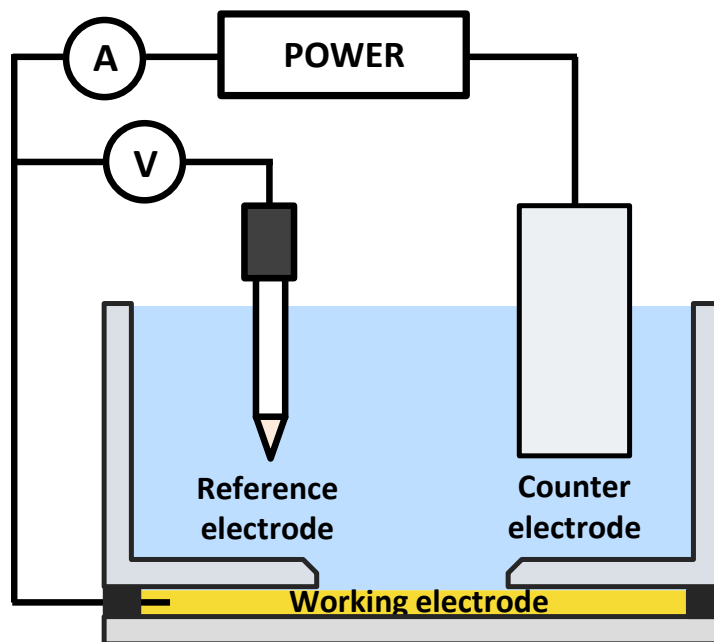
Figure 2.4. Schematic diagram of the three-electrode system for electrochemical experiment with Cu foil.

2.3. Synthesis of Sn/CuO nanowires on pyramid-patterned substrate

2.3.1. Preparation of pyramid-patterned substrate

Table 2.2 also shows the abbreviations of terms appearing in this section for convenience. The overall procedure of experimental condition were similar with the method for preparing Si patterned electrode and f_Sn/CuO NWs electrode. The different point is combining the two method, which means Sn/CuO NWs were synthesized on the pyramid-patterned substrate covered by Cu layer. For the patterned substrate with pyramid shape, the double side polished p-type (100)-oriented Si wafer was prepared. Si oxide layer with 500 nm thickness was also grown on the surface by wet oxidation. After SPM for 10 min at 120°C, HMDS and AZ 1512 photoresist were coated sequentially on the wafer. After soft baking for 30 s at 95°C, the wafer was exposed to UV light with pyramid-pattern mask. Then the wafer was developed in the developer for 90 s and soft baking for 60 s at 95°C was conducted. Si oxide etching and photoresist removal were carried out with BOE and SPM. After native Si oxide etching with 1 vol% HF, Si was etched with 30 wt%

KOH solution for 50 min at 80°C, so that the pyramid-pattern was formed. Finally, the residual Si oxide was eliminated by BOE for 15 min. For using the patterned substrate as an electrode, it was cut into 1×1 cm^2 with a dicing saw (DAD3350, Disco). Current collector was prepared by PVD. The patterned Si substrate was loaded in DC sputter chamber. The chamber was vacuumed below 1.0×10^{-5} torr. Before sputtering, each target was pre-sputtered for 2 min to remove oxides and other impurities presenting on the target surface. The sputtering was conducted in order of TaN/Ta/TaN, Cu on the substrate. TaN and Ta layers were sputtered alternatively at 500 V and 4 A in Ar : N_2 = 4 : 1 and Ar atmosphere with 50 sccm, so that TaN/Ta/TaN layer as Cu diffusion barriers were deposited on both side of patterned Si substrate. After that, Cu layer as a current collector was deposited on both side of TaN/Ta/TaN layer deposited patterned Si substrate at 500 V and 4 A in Ar atmosphere.

2.3.2. Sn/CuO nanowires formation on pyramid-patterned substrate

To form NW structure on the patterned substrate, down holder system was used, as shown in Figure 2.5. The solution consisted of 2 M of NaOH (Daejung, 98%) in

D.I. water and maintained at 5°C with stirring and N_2 gas purging for 1 hr. As mentioned before in section 2.2.1, the three steps were applied to Cu layer-covered patterned substrate with 5 mA/cm^2 for 10 s, -5 mA/cm^2 for 20 s, and 5 mA/cm^2 for 300 s, sequentially. After the three steps of galvanostatic methods, p_Cu(OH)$_2$ NWs electrode was obtained. Pt mesh and Ag/AgCl (KCl sat.) were used as a counter electrode and reference electrode, respectively. The p_Cu(OH)$_2$ NWs electrode was rinsed with D.I. water for 15 s and blown with N_2 gas to remove the residual water. After heat treatment with 250°C for 1 hr in Ar atmosphere, the p_Cu(OH)$_2$ NWs was converted to p_CuO NWs with dehydration. Sn was electrodeposited on p_CuO NWs electrode with -10 mA/cm^2 for 50 s in the solution of 0.07 M of $Sn_2P_2O_7$ (Sigma Aldrich, 98%) and 0.36 M of $K_4P_2O_7$ (Sigma Aldrich, 97%) in D.I. water. Then, the p_Sn/CuO NWs electrode was rinsed with D.I. water for 15 s and blown with N_2 gas. The electrodes were dried at 120°C for 12 h under vacuum before put into glove box to remove residual water.

2.3.3. Electrochemical measurement and characterization

The 2032-type coin-cell with p_Sn/CuO NWs electrode was assembled in Ar-

atmosphere glove box. Li metal foil (Cyprus) as a counter electrode and polypropylene-polyethylene-polypropylene (PP-PE-PP, Celgard) of multilayer separator were used. A mixture of 1.3 M of $LiPF_6$ in ethylene carbonate (EC) and diethyl carbonate (DEC) at a ratio of 3:7 vol% was used as the electrolyte solution. The electrochemical behavior of the cell was monitored using a cycler (Wonatech, WBCS-3000) at 25°C after impregnation of electrolyte for 24 hr. The cycling of the cell was performed at 0.1 C-rate for the formation cycle, followed by 1 C-rate cycling. The voltage region during cycling was between 0.01 and 3.0 V (vs. Li/Li^+). After electrochemical observation, the cells were dismantled in an Ar-filled glove box to prevent the reaction with oxygen and water in atmosphere. The electrodes were rinsed with dimethyl carbonate (DMC) to remove the residual electrolyte and salts on the electrode surface. To observe the surface morphology and composition of the electrode, field emission scanning electron microscope (FE-SEM, JEOL, JSM-6701F) at 10 kV accelerating voltage was employed.

Table 2.2. The Abbreviations of Pyramid-patterned Substrate Covered by Cu Layer

and Cu(OH)$_2$ Nanowires, CuO Nanowires, and Sn-electrodeposited CuO Nanowires

on Pyramid-patterned Substrate Covered by Cu Layer

Abbreviation	Explanation
p_Cu layer	pyramid-patterned substrate covered by Cu layer
p_Cu(OH)$_2$ NWs	Cu(OH)$_2$ nanowires on pyramid-patterned substrate covered by Cu layer
p_CuO NWs	CuO nanowires on pyramid-patterned substrate covered by Cu layer
p_Sn/CuO NWs	Sn-deposited CuO nanowires on pyramid-patterned substrate covered by Cu layer
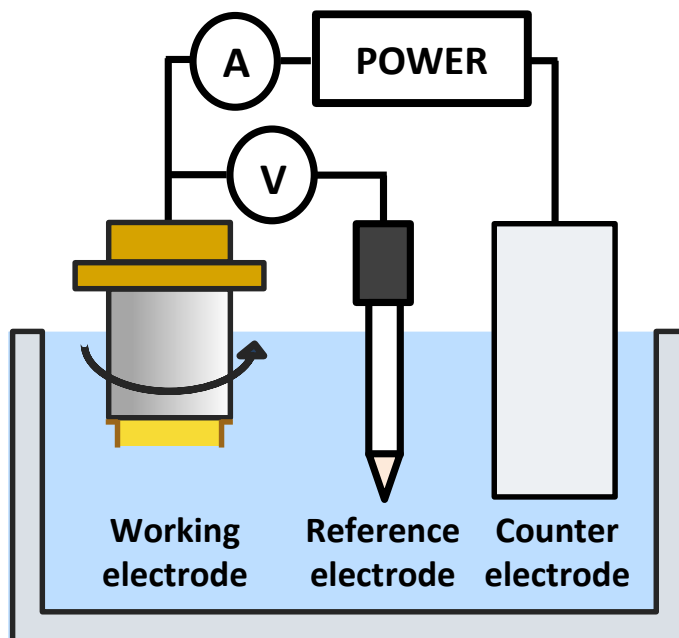
Figure 2.5. Schematic diagram of the three-electrode system for electrochemical

experiment with patterned substrate.

CHAPTER III. Results and Discussion

3.1. Sawtooth- and pyramidal-shape patterned Si anode

3.1.1. Patterning on Si wafer substrate

The sawtooth- and the pyramidal-shape patterning on Si wafer substrate was carried out by anisotropic Si wet etching. Si has different etch rate depending on its crystalline orientation. For instance, the (110) and (100) plane could be etched up to 600 and 400 times faster than the (111) plane, when KOH was used as etchant [85]. Therefore, the etching rate remarkably reduced when the (111) plane was exposed to etchant. These different etching rates enabled us to fabricate the structures such as sawtooth- and pyramidal-shape patterns on the wafer surface. Table 3.1 shows the top and cross-sectional view of (110)-oriented Si wafer during wet etching. In (110)-oriented Si wafer, the (111) plane has the slope of the oblique side was 35.25° compared to the horizontal surface. In addition, the reason of etching area like hexagonal shape is also due to the location of vertical (111) plane. Area ratio of base plane to newly exposed plane can be calculated by orthogonal projection. Because, the angle between base plane and exposed plane is 35.25°, the area of interesting

planes has a different ratio of cos 35.25° times. Therefore, if the base plane is set by 1, the newly exposed plane is 1/cos 35.25° = 1.225. The etched and exposed plain shows sawtooth-shape pattern. In the same manner, in (100) oriented Si wafer, the (111) plane has the slope of the oblique side was 54.7° as shown in Table 3.2. If base plane is set by 1, the exposed plane is 1/cos 54.7° = 1.731. The etched plain shows the concave pyramidal-shape pattern.

As a result of MEMS and etching process, five different electrodes (N-0, S-85, S-170, P-50, and P-100) were prepared as shown in Figure 3.1 (a). The detail physical dimensions of the electrodes are summarized in Table 3.3. When the etching process was completed, TaN/Ta/TaN, Cu, and Si layers were sequentially deposited on the patterned substrates by sputtering as a Cu barrier layer, current collector, and active material, respectively. The TaN/Ta/TaN and Cu layers were sputtered on the entire of the outer surface of patterned substrate for electrical contact. The Si was deposited on the top surface of the substrate and the deposited film was verified by the cross-sectional FE-SEM analysis as shown in Figure 3.1 (b). The thicknesses of the Si layers were 750, 650, and 450 nm for plain, sawtooth, and pyramidal electrodes, respectively. The different thicknesses of Si were due to the straight feature of sputtering and slope of the patterns. The deposit amount of Si was controlled as the

same for all the electrodes.

Table 3.1. The Top and Cross-sectional View of (110)-oriented Si Wafer during Wet

Etching and Area Ratio of Base Plane and Newly Exposed Plane
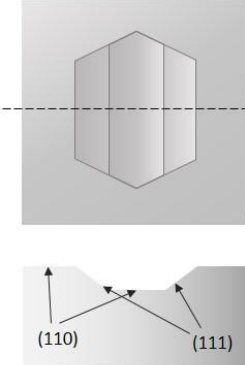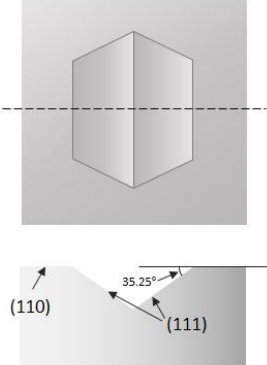
(110)-oriented Si substrate

Etching shape			
Area ratio	Base plane	1	1
	Exposed plane	<1.225	1.225

Table 3.2. The Top and Cross-sectional View of (100)-oriented Si Wafer during Wet

Etching and Area Ratio of Base Plane and Newly Exposed Plane
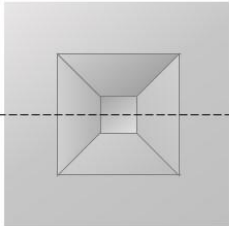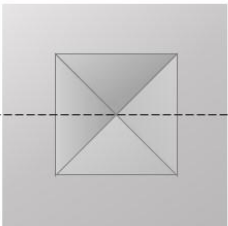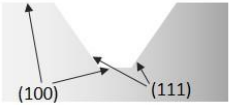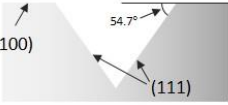
(100)-oriented Si substrate		
Etching shape		
Area ratio	Base plane	1	1
	Exposed plane	<1.731	1.731

Table 3.3. The Detailed Physical Dimension of Plain and Sawtooth and Pyramid-

patterned Electrodes

Sample label	Pattern shape	Pattern width / depth	Thickness of Si film
N-0	Plain	- / -	0.75
S-85	Sawtooth	85 / 30	0.65
S-170	Sawtooth	170 / 60	0.65
P-50	Pyramid	50 / 35	0.45
P-100	Pyramid	100 / 70	0.45

*unit: μm

(a)

N-0

100 μm

100 μm

S-85

85 μm

S-170

170 μm

P-50

50 μm

100 μm

P-100

(b)

Si: 0.75 μm

Cu: 1.5 μm

2 μm

Si: 0.65 μm

Cu: 1.3 μm

Si: 0.45 μm

Cu: 0.9 μm
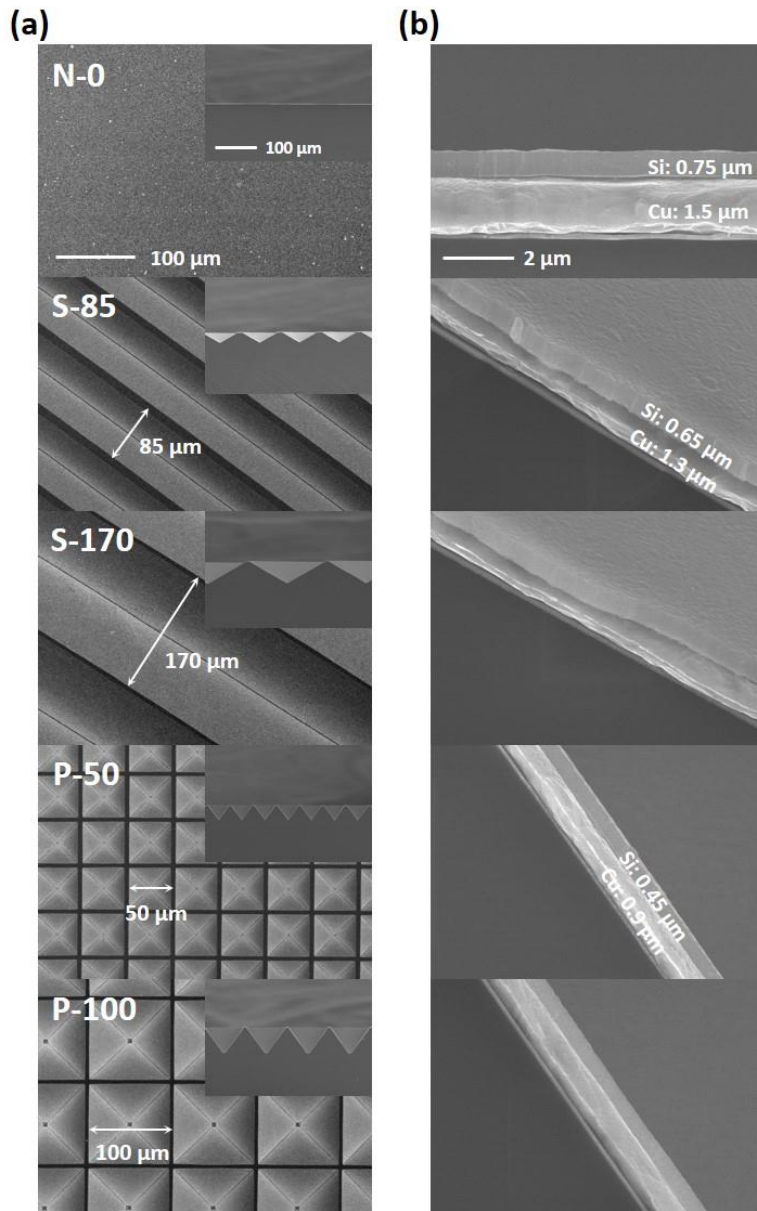
Figure 3.1. (a) FE-SEM surface and cross-sectional images of substrate (inset), (b)

magnified cross-sectional images of deposited layers of TaN/Ta/TaN, Cu, and Si on

each substrates.

5 7

3.1.2. Electrochemical behavior of patterned electrodes

Figure 3.2 displays voltage profiles of the five electrodes for the formation step. The discharge capacities of the electrodes were ranged from 2500 to 2800 mAh/g, and the typical two-phase reaction of crystalline Si was absent. In addition, the Coulombic efficiency of the first cycle resided was in the range 70 ~ 80%. This observation shows that the Si film made by PVD was amorphous. It was also supported by a low cut-off voltage (80 mV) applied in this study, indicating that the crystallization during the lithiation could hardly occur. The discharge capacity of N-0 electrode was 2480 mAh/g, and the Coulombic efficiency was 87%. However, the patterned electrodes showed a greater discharge capacity, approximately 2700 mAh/g, and their Coulombic efficiencies (approximately 93%) were far greater than that of N-0 electrode, indicating that more irreversible capacity was required for the plain electrode than the patterned electrodes. In general, the irreversible capacity loss seen from the very first cycle is attributed to the formation of a solid electrolyte interphase (SEI). It seemed that the electrolyte decomposition was more severe on N-0 electrode than the patterned electrodes.

To investigate the effect of pattern structure on the cycle performance, the charge

and discharge capacities of the electrodes were compared, as shown in Figure 3.3 (a). The initial specific discharge capacities increased in order of N-0, S-85, S-170, P-50, and P-100. Notably, N-0 electrode faded rapidly within first few cycles. It was presumed that the early deterioration of N-0 electrode was ascribed to the stress during Li insertion and extraction and successive pulverization of Si. In the process of pulverization, the isolated dead Si must have been formed, which could not contribute to the discharge capacity in the later stage [86]. The sawtooth electrodes (S-85 and S-170) also showed a drastic degradation, but with a slightly improved initial discharge capacity. However, the pyramid-patterned electrodes (P-50 and P-100) showed better capacity retention than any other electrodes according to the cycle number. These electrodes maintained their capacity until the 10th cycle, still exhibiting 2260 mAh/g capacity. The major reason of the improved retention is the enlarged surface area of the pyramid-patterned electrode (+40% vs. plain). The large surface area could dissipate the stress induced by the volume change during the charge and discharge, because of the decrease in the Si layer thickness [87]. In addition, the concave regions, which exist only in sawtooth and pyramidal patterns, accommodated the volume expansion as well. Moreover, the pattern density also seemed to affect the capacity retention. Both patterned electrodes with large pattern

size, S-170 and P-100, showed a greater discharge capacity than S-85 and P-50, respectively, over cycling. In short, the electrodes with a low pattern density performed better than those with high pattern density. The relationship between the pattern density and the capacity will be explained in more detail in the later section.

Figure 3.3 (b) exhibits the Coulombic efficiencies of the five electrodes. The common characteristics of the electrodes can be summarized as follows: (1) In the beginning cycles, the capacity and the efficiency of the electrode slightly increased, because of the activation of Si as Li ions diffused, as notably observed in the pyramid-patterned electrodes. (2) The capacity started to decrease drastically when the efficiency showed a hump. (3) In the later cycles, the efficiency was recovered with the disappearance of the hump even though the capacity kept decreasing and remained low. The characteristic is often called a hump behavior [88]. The capacity and the efficiency rapidly decreased at the hump, because the electrode surface was exposed due to cracking and successive Si exfoliation, accompanied with the contact loss between the current collector and Si. The recovered efficiency at the extended cycle resulted from the contribution of the remaining Si attached on Cu after all. The deterioration of the electrode can be distinguished by the position of hump. In other words, the earlier a hump appears, the shorter cycle-life the cell has.

The tolerance against the volume changes during the lithiation and delithiation can be represented by the remaining Si on the electrode. The FE-SEM images of the Si film after the 20th cycle in the plain and patterned electrodes are presented in Figure 3.4 (a, b), and the corresponding coverages were measured (Table 3.4). The surface coverages of Si increased in the order of N-0 < S-85 < S-170 < P-50 < P-100, which coincided with the order of capacity retention. This emphasized that the pattern structures were effective to increase the endurance against the volume change by the release of stress between Si and substrate.

In the sawtooth and pyramid-patterned electrodes, it seemed that the Si in the convex area rapidly reacted with Li ions, thus triggering a rapid exfoliation. As shown in Figure 3.4, a few amounts of Si islands were retained around the convex area in the patterned electrodes. The Li flux on the Si at the convex area must be greater than the concave area, because it is largely exposed to the electrolyte, and thus suffer from the relatively more severe volume change during the charge and discharge process. It was definite that the high-density patterned electrode contained a larger convex area than the low-density pattern. Therefore, the low density pattered electrodes showed a better cycle performance.

Actually, there are possibility of not only the pattern shape effect but also the film

6 1

thickness effect of the Si active material on the cell performance. In general, it has been reported that the thinner the film, the better the performance of the electrode [8,87]. Figure 3.5 shows the thickness effect of Si film on specific capacity. As the thickness decreased, the capacity retention was improved. However, compared to the cycle performance of P-100, the capacity could not be maintained. Therefore, the pattern shape effect was confirmed.

The patterned electrodes obviously affected the rate capability. Because the sawtooth and pyramid-patterned electrodes had 1.1 and 1.4 times larger active area for the lithiation and delithiation, respectively, and they must be favorable for alleviating the stress under harsh condition. Figure 3.6 shows the cycle retention during the charge and discharge cycle with a C-rate from 0.5 to 2. The cycle retention of P-100 retained approximately 80% of its initial capacity at 2 C-rate, whereas the plain electrode could only retain 10% of its initial value. Furthermore, P-100 possessed a moderate reversibility, exhibiting 80% of the initial capacity, whereas the plain electrode could not. The patterns on the substrate not only helped to improve the cyclability but also the rate capability of the Si film electrode.

In summary, the effect of electrode structure on the electrochemical performance of Li-ion battery was investigated. Two types of sawtooth and pyramidal patterns

were investigated to confirm the effect of surface area of the active material and stress release during the lithiation and delithiation. The patterned electrodes showed better cycle retention and rate capability compared to the plain electrode. Especially, P-100 electrode with a large surface area and deep depth of the pattern improved the rate capability as well as the capacity retention. The patterned electrodes reduced the stress originated from the volume change during the charge and discharge process and also enhanced the adhesion between the active material and current collector. These results suggest that the modification of the electrode structure overcame the problems of Si anode related to severe volume changes and finally not only improved the capacity retention but also the rate capability.

Table 3.4. The Capacity, Capacity Retention, and Si Coverage on the Surface of Five

Electrodes after 20th Cycle

Sample label	Capacity / mAh/g	Retention / %	Coverage / %
N-0	9.8	0.6	0
S-85	277.2	12.9	9.7 ± 2.3
S-170	521.7	22.3	21.2 ± 4.6
P-50	1110.6	47.0	57.0 ± 3.9
P-100	1242.8	52.0	65.6 ± 3.6
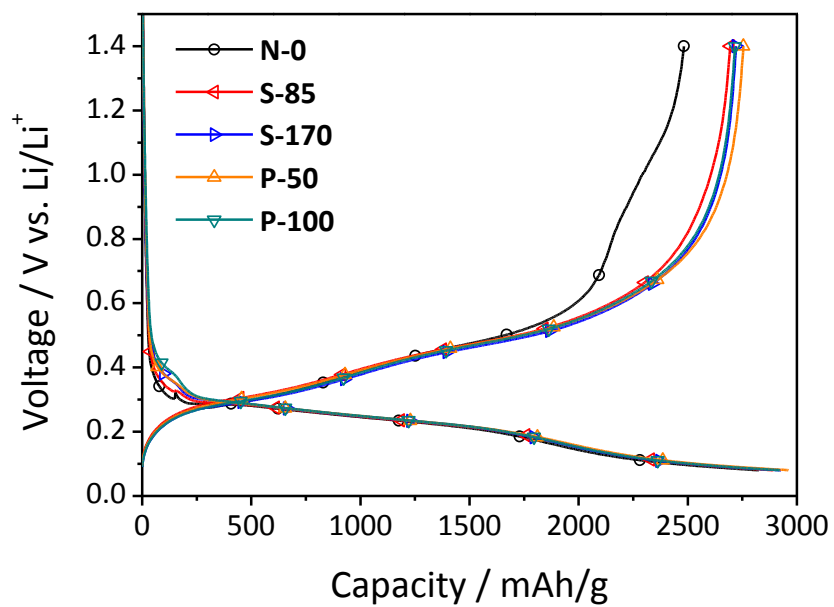
Figure 3.2. Voltage profiles for N-0, S-85, S-170, P-50, and P-100 at formation step

(0.1 C-rate).

(a)

(b)
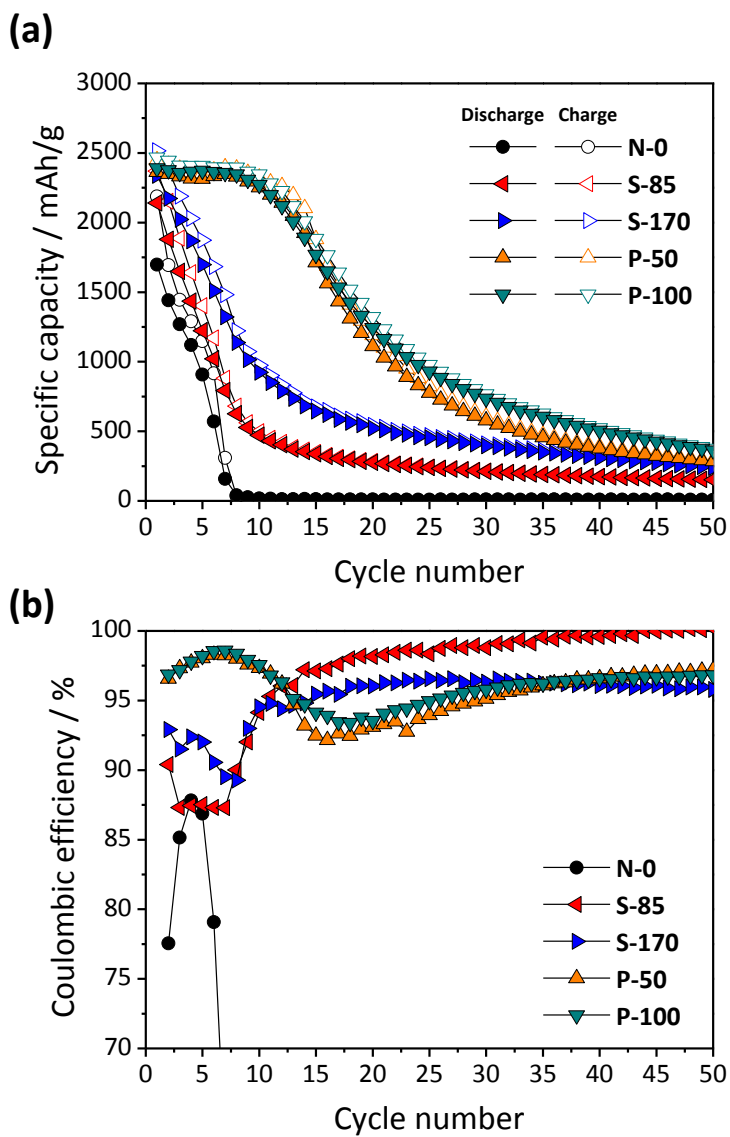
Figure 3.3. (a) Specific capacity with charge (open)/discharge (solid) and (b) coulombic efficiency of N-0, S-85, S-170, P-50, and P-100 during 50 cycles (0.5 C-rate).

66
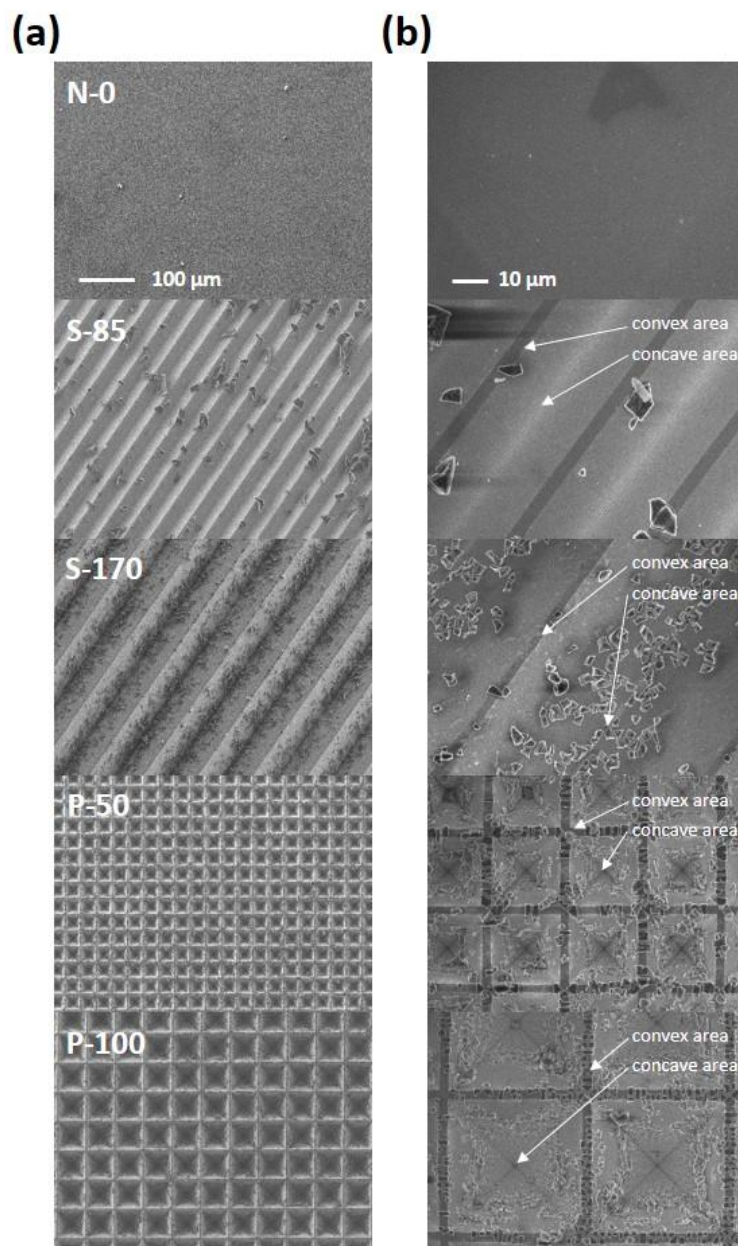
Figure 3.4. (a) FE-SEM images of electrode surface after 20th cycle in order of N-0,

S-85, S-170, P-50, and P-100 and (b) their magnified surface images.
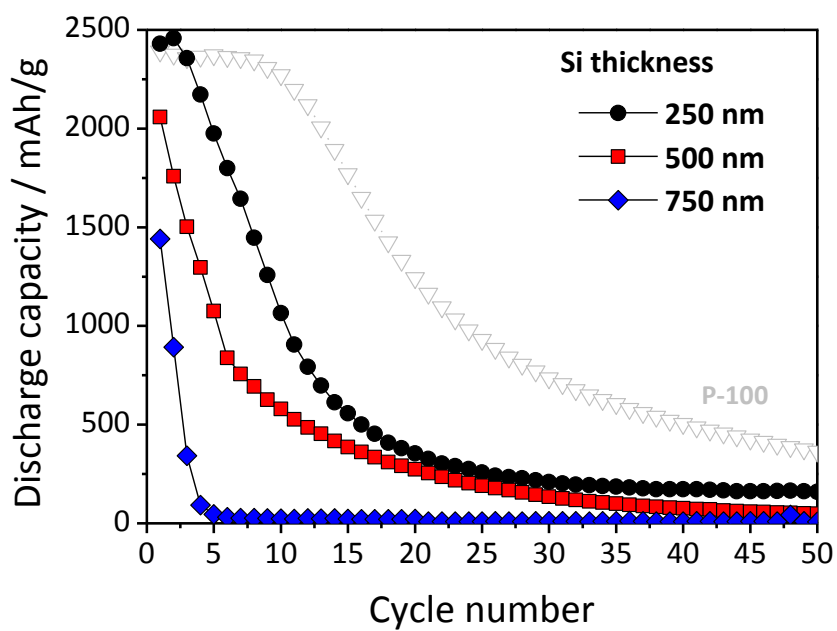
Figure 3.5. Cycle performance of 250, 500, and 750 nm thick Si films upon 50th cycle

at 0.5 C-rate.
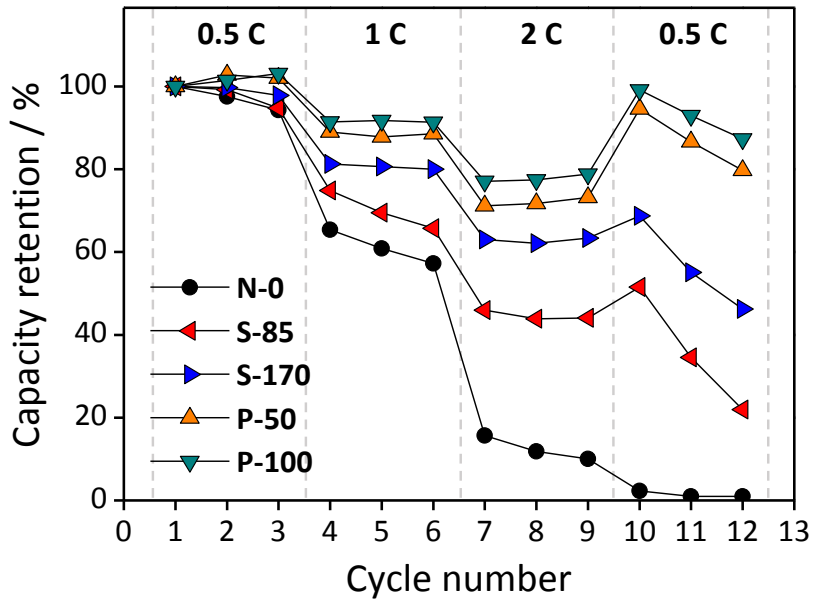
Figure 3.6. Rate capability of N-0, S-85, S-170, P-50, and P-100 with 0.5, 1, 2 C-

rate.

3.2. Sn/CuO nanowires electrode on Cu foil

3.2.1. Preparation of Sn/CuO nanowires on Cu foil

The f_Cu(OH)$_2$ NWs electrode was synthesized with electrochemical methods. The Cu foil was electrochemically anodized with three steps of galvanostatic method in three-electrode system as shown in Figure 3.7 (a, b). The first step in the region (1) was for Cu oxidation on Cu foil with anodic current of 5 mA/cm^2 for 10 s to diminish an uneven native Cu oxide layer. In the next step, the Cu oxide removal was carried out with -5 mA/cm^2 for 20 s in the region (2). Finally, the Cu foil was anodized to form Cu(OH)$_2$ NWs in basic solution in the region (3):

(Eq 3.1) $Cu^{2+} + 2OH^- \rightarrow Cu(OH)_2$
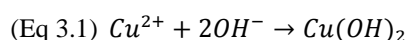
The dissolved Cu ion was reacted with hydroxyl ion in aqueous solution, so that Cu(OH)$_2$ nanoparticles were formed. The Cu(OH)$_2$ nanoparticles got together and formed nanowires on the Cu foil by oriented attachment [88]. In this study, the anodization of Cu foil was conducted at 5°C. The shape of nanowires was changed according to the temperature of the solution, as shown in Figure 3.8. When the temperature increased by 10°C, a hedgehog-like shape was observed on the surface.

This confirms that nanowire shape varies with temperature, as reported in other literature [79]. So, the experiment was performed at 5°C to obtain a uniform nanowires shape. The formed $Cu(OH)_2$ NWs were below 300 nm of diameter.

After heat treatment at 250°C for 1 hr in Ar atmosphere, the light blue $Cu(OH)_2$ NWs turned into black CuO NWs with curved and rough surface. The curved morphology of CuO NWs was due to the stress induced by the dehydration of $Cu(OH)_2$. In the orthorhombic crystal structure of $Cu(OH)_2$, Cu(II) has a pentahedral surrounding with five OH- ions forming square pyramid. At elevated temperature, relatively long Cu-O bond could be weak and square planar entities $Cu(OH)_4$ linked together reversibly [89]. Due to the stability of structure depending on network of hydrogen bonds, feasible shift of CuO_4 or Cu can be possible. In short, at the temperature of 250°C, the dehydration of $Cu(OH)_2$ is accomplished by an oxolation mechanism. The length of the CuO NWs was around 5 μm and the diameter was 218.4 (± 27.9) nm.

Finally, the Sn was covered onto the CuO NWs electrode with electrodeposition in aqueous solution. The f_Sn/CuO NWs electrode was obtained which was entirely covered by Sn. Figure 3.9 exhibits the deposition time for 50 s was optimum. Above 75 s, the nanowires adhered each other and the agglomerated Sn which connected

with nearby nanowires were observed. The diameter of Sn/CuO NWs deposited for

50 s was 227.6 ($\pm$ 26.2) nm. Figure 3.10 exhibits the cross-sectional images of f_CuO

NWs and f_Sn/CuO NWs electrodes. The surface of Sn/CuO NW was rougher than

CuO NW due to deposited Sn on the surface. The boundary of CuO NWs and Sn

regions was not clearly observed, so it was hard to measure the thickness of the

deposited Sn layer. This was assumed that the Sn was melted by heat during the

cutting by Ar-ion beam because Sn has relatively low melting point of 231.9°C.

In summary, the scheme of preparation procedures for f_Sn/CuO NWs electrode

is exhibited in Figure 3.11. The f_Sn/CuO NWs electrode was synthesized with

electrochemical methods. The Cu foil was electrochemically anodized with

galvanostatic method. After heat treatment, $Cu(OH)_2$ NWs were converted to CuO

NWs and finally the CuO NWs were covered by Sn with electrodeposition. Figure

3.12 (a-c) show the FE-SEM surface images of the $Cu(OH)_2$ NWs, CuO NWs after

heat treatment and Sn/CuO NWs electrode, respectively. As shown in Figure 3.12

(d), the EDS mapping of Sn on the Sn/CuO NWs electrode indicated evidence of the

successful Sn loading and its uniform distribution over CuO NWs. TEM-EDS

mapping of Sn/CuO NW was also carried out, as shown in Figure 3.13. The elements

of Sn, Cu, and O were detected along the nanowire.
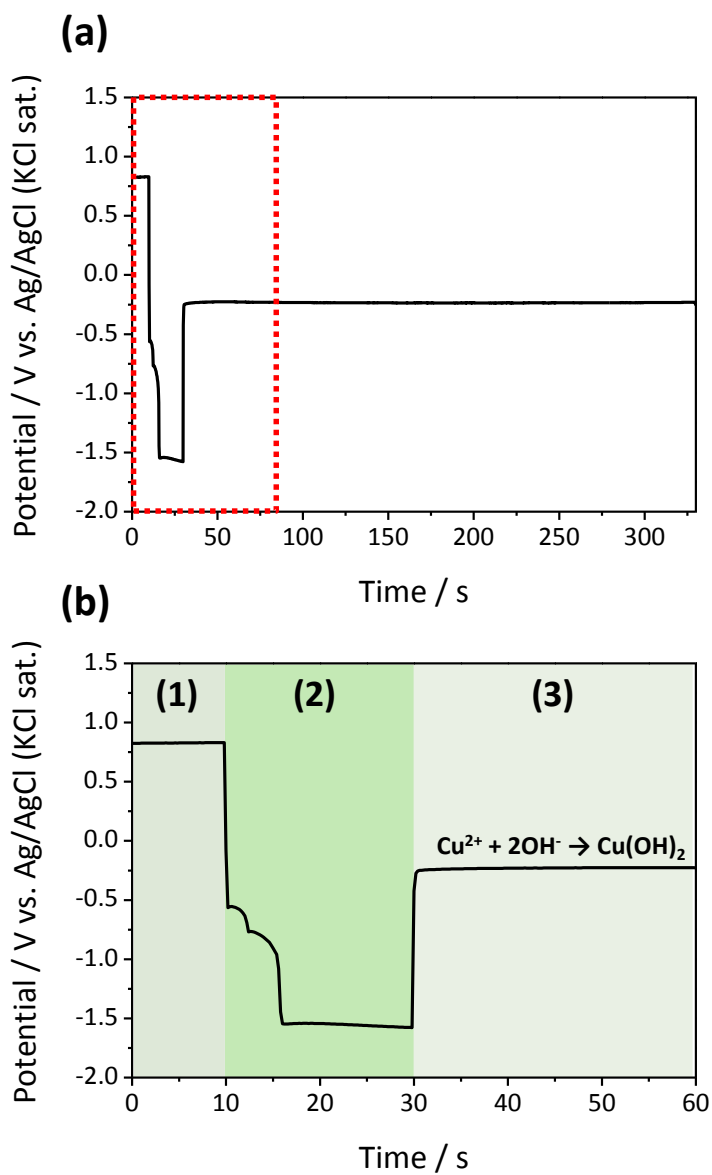
Figure 3.7. (a) Potential profile of galvanostatic method and (b) magnification in the

region of initial 60 s during three steps with (1) 5 mA/cm^2 for 10 s, (2) -5 mA/cm^2

for 20 s, and (3) 5 mA/cm^2 for 300 s.
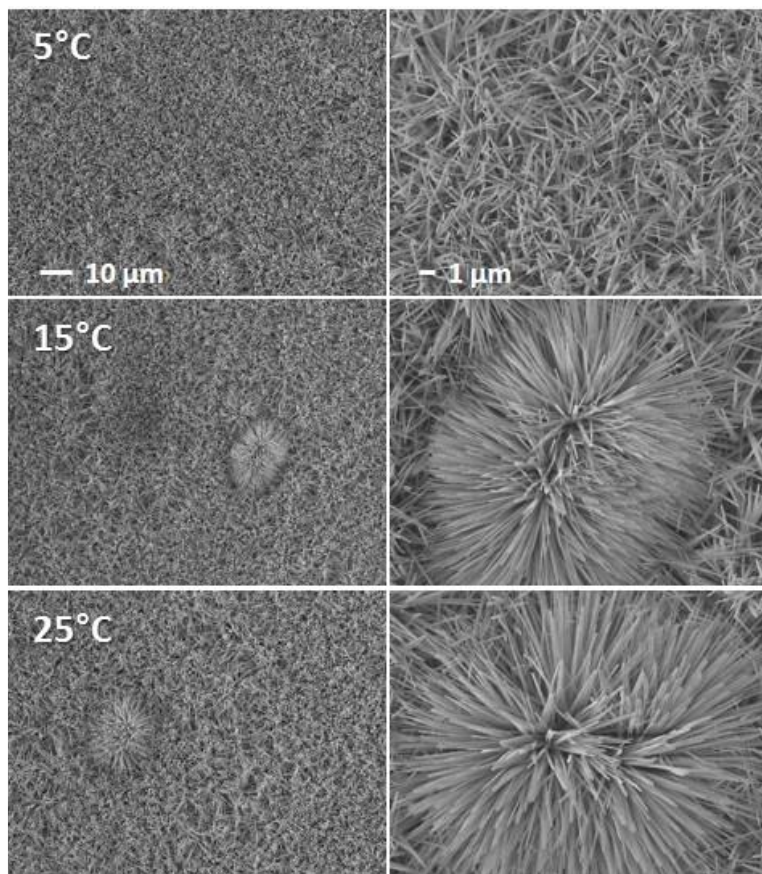
Figure 3.8. FE-SEM surface images of f_Cu(OH)$_2$ NWs electrode anodized at 5, 15, and 25°C.
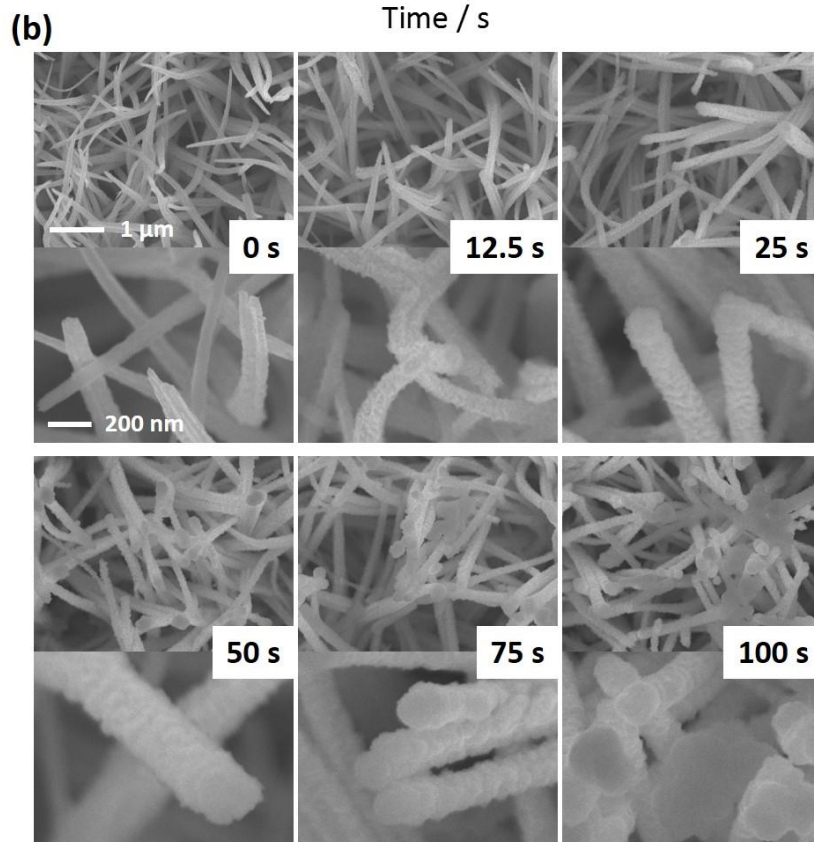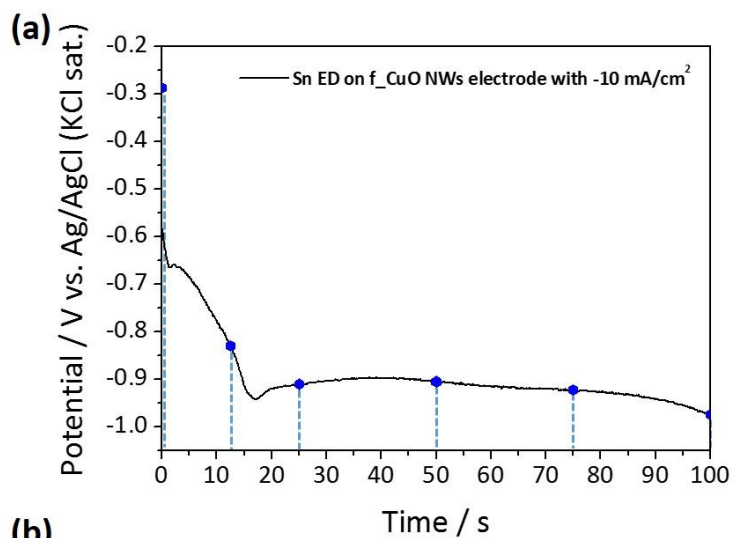
Figure 3.9. FE-SEM surface images of f_Sn/CuO NWs electrode according to the

Sn ED time from 0 s to 100 s.
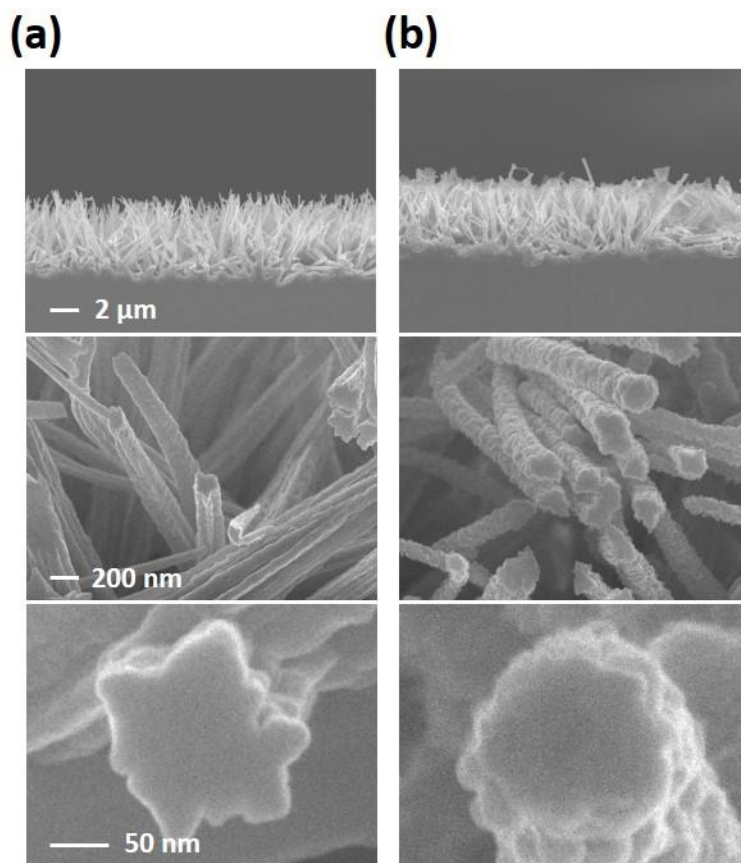
Figure 3.10. FE-SEM cross-sectional images of (a) f_CuO NWs electrode and (b)

f_Sn/CuO NWs electrode.
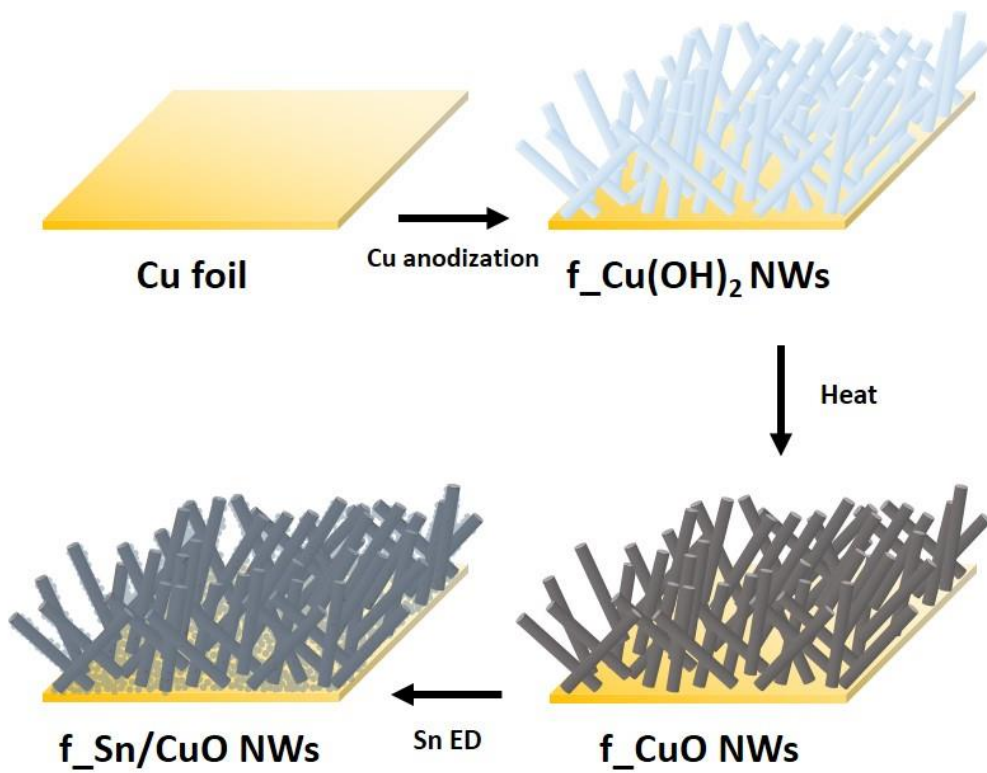
Figure 3.11. Schematic diagrams of the fabrication process of f_Sn/CuO NWs electrode.
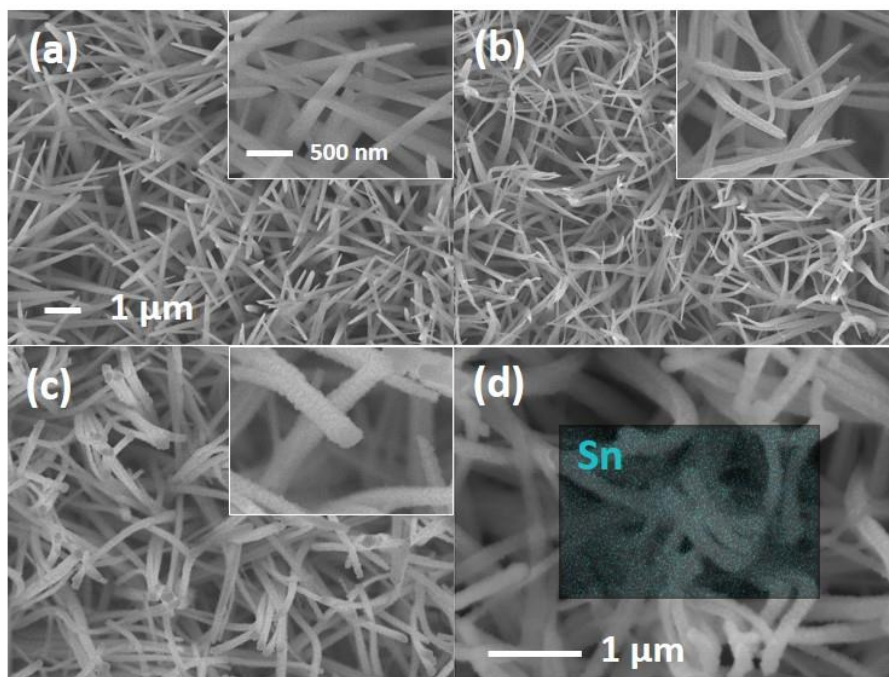
Figure 3.12. FE-SEM surface images of (a) f_Cu(OH)$_2$ NWs electrode, (b) f_CuO NWs electrode, (c) f_Sn/CuO NWs electrode and (d) EDS mapping of Sn on f_Sn/CuO NWs electrode.
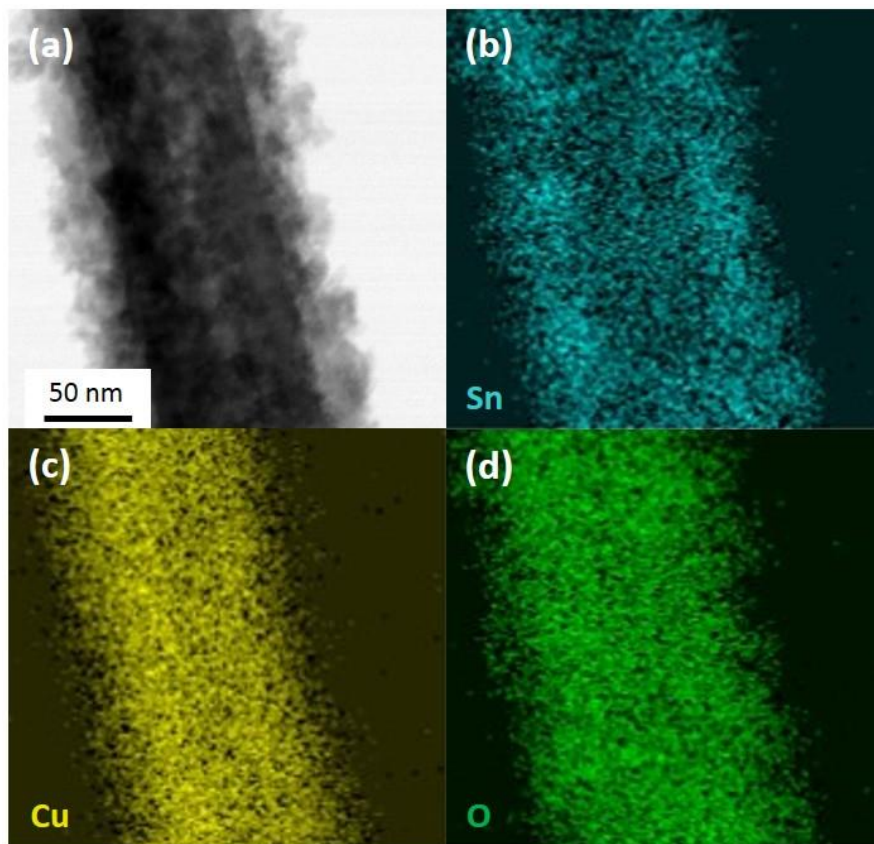
Figure 3.13. (a) TEM image and EDS maps of (b) Sn, (c) Cu, and (d) O of Sn/CuO

NW.

3.2.2. Characterization and electrochemical behavior of Sn/CuO nanowires on Cu foil

First of all, the amounts of Sn and CuO on f_Sn/CuO NWs electrode were measured by ICP-AES. When measuring the amount of CuO, it was hard to obtain the amount directly because Cu dissolved from CuO NWs and Cu foil could not be distinguished. Therefore, the genuine CuO content was measured by using the different dissolution rate between CuO and Cu. Figure 3.14 (a) displays Pourbaix diagram of Cu. According to the graph, CuO is unstable under acidic condition, so it dissolves in acidic solution. However, Cu foil could be also slowly dissolved. In order to distinguish the amount of Cu, the following methods were used. The f_Sn/CuO NWs electrode was immersed in 5 ml of 1 vol% HNO_3. To measure the concentration of Cu, 1 ml was sampled at specific time intervals. At the same time, 1 ml of fresh 1 vol% HNO_3 was replenished to maintain 5 ml. From ICP-AES results, the dissolution amount of Cu was calculated in each time and the cumulative amount of the Cu content was obtained. Figure 3.14 (b) indicates the cumulative amount of Cu sampled at specific time according to the Sn electrodeposition time. To distinguish the Cu originated from CuO and Cu, samples were taken until a saturated

slope was observed. When the slope becomes constant, the slope at that time means the dissolution speed of Cu from Cu foil. By plotting trend lines with this slope and calculating the difference of the y-axis values, the amount of Cu ion from CuO was obtained as seen in Figure 3.14 (c). Unlike CuO, the amount of Sn was directly measured with ICP-AES by dissolving the whole of f_Sn/CuO NWs electrode under strongly acidic condition (aqua regia). In the f_Sn/CuO NWs electrode prepared by electrodeposition of Sn for 50 s, the amount of Sn was 0.079 mg/cm^2 and the amount of CuO was 0.273 mg/cm^2.

The crystal structures of the Sn film, Cu(OH)$_2$ NWs, CuO NWs, and Sn/CuO NWs were characterized by XRD observed in Figure 3.15. There are three strong diffraction peaks in all samples; 43.3°, 50.4° and 74.1° which originated from the Cu foil substrate (JCPDS 04-0836) of (111), (200) and (220), respectively. The Sn film on Cu foil shows both tetragonal Sn (JCPDS 04-0673) and monoclinic Cu$_6$Sn$_5$ alloy (JCPDS 45-1488). It was confirmed that at initial state of Sn electrodeposition, Sn becomes alloyed with Cu. However, the Cu$_6$Sn$_5$ crystalline structure was not observed at low current density (-5 mA/cm^2) during electrodeposition. For the Cu(OH)$_2$ NWs, the diffraction peaks indexed to orthorhombic Cu(OH)$_2$ (JCPDS 80-0656) could be identified. Both of the CuO NWs and Sn/CuO NWs, the broad

diffraction peaks at 35.5° and 38.9° could be assigned to the ($\bar{1}$11) and (200) plane of monoclinic CuO phase (JCPDS 48-1548). Also, the cubic Cu_2O (JCPDS no. 05-0667) peaks appear on 36.4°, 42.3° and 61.3° correspond to (111), (200) and (220), respectively. The Cu_2O could be formed with incomplete dehydration and reduction of $Cu(OH)_2$ with X-ray exposure [90]. The broad diffraction peaks of CuO and Cu_2O suggest the small crystallite size in the nanowires. The diffraction peak of Sn crystallinity was not particularly observed with Sn/CuO NWs, indicating that the electrodeposited Sn on CuO NWs was in amorphous phase. In addition, interestingly, the peak of Cu_6Sn_5 alloy was not detected due to reduced current density on Sn electrodeposition originated from enlarged surface area and CuO reduction.

The XPS spectra of f_Cu(OH)$_2$ NWs, f_CuO NWs and f_Sn/CuO NWs electrodes were recorded to analyse the surface composition and chemical state. The C_{1s} peaks with the main peak at 284.8 eV was adjusted to calibrate all of the binding energies. In Figure 3.16, the strong peaks at 934.8 eV and 932.9 eV correspond to Cu^{2+} $2p_{3/2}$ and Cu $2p_{3/2}$, respectively [91]. The Cu^+ $2p_{3/2}$ signal can also appear near Cu $2p_{3/2}$ area. However, because there is no Cu^+ in f_Cu(OH)$_2$ NWs, the peak at 932.9 eV is originated from only Cu $2p_{3/2}$ on Cu substrate. The two extra signals at 942 and 944.5 eV are also observed corresponding to shake-up satellite peaks from Cu^{2+}. In the

f_CuO NWs electrode, the peak at 932.9 eV contains Cu^+ $2p_{3/2}$ signal from Cu_2O as well as Cu $2p_{3/2}$ as detected in Figure 3.15.

In Table 3.5, the percentage of Cu, Cu^+, and Cu^{2+} elements in f_Cu(OH)$_2$ NWs, f_CuO NWs, and f_Sn/CuO NWs electrode were estimated. Shake-up satellite peaks at (1), (2) and the main $2p_{3/2}$ peaks at (3), (4) were represented at three graphs, respectively in Table 3.5. The shake-up satellite peaks are originated from the spectra of d^9 Cu^{2+} and not in d^{10} Cu or Cu^+. The shake-up peaks could occur when the outgoing electron interacts with a valence electron and excites it to a higher energy level in d-orbital. Therefore, the kinetic energy reduction of the outgoing electron occurs and generates satellite structure like possessing high binding energy in Cu $2p_{3/2}$. Because the shake-up satellite peaks are originated from Cu^{2+}, the area of the shake-up satellite peaks should be included in Cu^{2+} when quantitative analysis is conducted.

In Cu $2p_{3/2}$ signal of f_Cu(OH)$_2$ NWs, the area of (1) + (2) + (3) represents Cu^{2+} species and the area of (4) is Cu. After heat treatment in Ar atmosphere, the Cu^+ was formed as detected in XRD results (Figure 3.15). So, both Cu and Cu^+ species were contained in the peak of (4). Because the Cu^+ was originated from Cu^{2+} in Cu(OH)$_2$, the ratio of Cu should be maintained. So, the (4) peak having 21.9% of area in Cu

8 3

2p$_{3/2}$ include 14.5% of Cu (the ratio of Cu at Cu(OH)$_2$ 2p$_{3/2}$) and 7.4% of Cu$^+$ (newly formed from Cu(OH)$_2$) in f_CuO NWs.

During preparation of f_Sn/CuO NWs, the Cu$_2$O and CuO were electrochemically reduced to Cu, so the ratio of Cu$^+$ and Cu^{2+} should be also decreased. The area percentage of (1) + (2) + (3) in f_Sn/CuO NWs was 68.3% which is also the ratio of Cu^{2+}. However, because it is hard to distinguish between Cu and Cu$^+$ in Cu 2p$_{3/2}$, the atomic percentage of Cu and Cu$^+$ were estimated. The Cu in f_Sn/CuO NWs seemed above 24.3%, which was calculated from summation with 14.5% (Cu) and 9.8% (78.1% - 68.3%, Cu^{2+}). Cu$_2$O was also reduced, so it existed below 7.4%.

From above calculation, the percentage of Cu$^+$ in Cu$_2$O at f_CuO NWs electrode seemed 7.4% which was 9.5% of CuO. So, it was confirmed that most of copper oxide existed with CuO. In addition, the main O 1s peak at 531.1 eV is attributed to -OH in the Cu(OH)$_2$ lattice. The core level XPS of O 1s presents two peaks in CuO sample, which can be ascribed to oxygen in CuO lattice and hydroxyl group of outer surface of CuO originated from the Cu(OH)$_2$, as seen in Figure 3.17. In Figure 3.18, the Sn 3d peaks show that the existence of Sn and Sn^{4+} on f_Sn/CuO NWs [92,93].

Figure 3.19 presents the TEM images of Sn/CuO NWs. The nanowires were loaded on Mo grid by scratching the f_Sn/CuO NWs electrode. The bright field

images show spherical grains with a dimension around 8 nm of Sn on CuO NWs in Figure 3.19 (b, c). When the Sn was electrodeposited on CuO NWs, the CuO could also be reduced to Cu at the potential during Sn deposition. From high-resolution TEM images of outer region on Sn/CuO NWs in Figure 3.19 (d-f), the Cu (111) and CuO ($\bar{1}$11) lattice planes were observed, which was coincided with the result of XRD peaks in Figure 3.15. Lattice morphology could not be verified in the Sn-deposited area, indicating that Sn was in an amorphous state. The result presents that partial area of CuO surface is converted to Cu during Sn deposition (Figure 3.20 (a)). So, the reduced Cu acts as a node anchoring CuO and Sn between CuO and Sn can enhance the electrical conductivity during cycling. Figure 3.20 (b) exhibits the preferable electron pathway in the Sn/CuO NW. Because the electrical conductivity of Cu is higher compared to CuO, the electron can move easily. After CuO reduction with linear sweep voltammetry (20 mV/s, OCP $\rightarrow$ -1.8 V vs. Ag/AgCl (KCl sat.), twice) and chronopotentiometry (-10 mA/cm^2 for 50 s, twice), the lithiation peaks of CuO were remarkably reduced as shown in Figure 3.21. Therefore, it was able to confirm existence of Cu between CuO and Sn indirectly when Sn electrodeposition was conducted.

The shape of electrodeposited Sn was investigated according to the CuO NWs

reduction. In Figure 3.22, without CuO reduction, Sn was deposited on CuO NWs like film. However, after CuO reduction with -10 mA/cm^2 for 50 s, the Sn was deposited like bunch of grapes. The difference of deposited Sn shape was originated from existence of reduced Cu nodes. Without CuO reduction, coulomb consumption at Sn deposition was low due to simultaneous CuO reduction. On the other hand, after CuO reduction, there were reduced Cu nodes and Sn deposition could easily occur on the Cu nodes compared to CuO surface. So, dominant growth on the Cu nodes generated bunch of grapes shape of Sn. This shape difference also indicated the existence of reduced Cu on CuO NW.

To confirm the activities of Sn and CuO with Li-ion in f_Sn/CuO NWs electrode, cyclic voltammetry was conducted. Figure 3.23 presents the voltammograms of f_Sn film, f_CuO NWs, and f_Sn/CuO NWs electrodes at 1st ~ 5th cycles. The CV of f_Sn film and f_CuO NWs electrodes show the cathodic and anodic peaks corresponding to the multistep Li-ion reaction. In Figure 3.23 (a), the reduction curves from 0.01 to 0.4 V corresponding to the Li intercalation processes of Sn and Cu_6Sn_5 to form the $Li_{4.4}Sn$ and Cu. The oxidation peaks from 0.4 to 0.8 V correspond to the reformation of Cu_6Sn_5 [57]. The existence of Cu_6Sn_5 was previously confirmed by X-ray diffraction (Figure 3.15). Figure 3.23 (b) shows the CV curve of f_CuO NWs

electrode. At the 1st cathodic scan, there appeared mainly three peaks at 2.11 V, 1.09

V and 0.85 V. The peak at 2.11 V for the CuO NWs corresponds to solid solution

formation of Li_xCuO. The peaks at 1.09 V and 0.85 V are associated with the

generation of Cu_2O, followed by reduction into Cu and Li_2O. After the 1st cyclic

curve, the peak shift was observed from 1.18 V to 1.25 V. It was usual phenomenon

for metal oxide and elucidated textual modification, indicating good structural

stability and redox reversibility [80,94]. The anodic peak around 2.48 V correspond

to the formation of Cu_2O and oxidation of Cu_2O into CuO [82,95]. The CV of

f_Sn/CuO NWs electrode was shown in Figure 3.23 (c). The peaks of f_Sn/CuO

NWs electrode coincide with f_Sn film and f_CuO NWs electrodes. The weak

reduction peak at near 0.5 V is related to Eq 3.2 and the peak at about 0.15 V is

associated with the alloying in the form of Eq 3.3.

(Eq 3.2) $SnO_2(s) + xLi^+ + xe^- \rightarrow Sn + 2Li_{x/2}O(s) \qquad E \approx 0.5\ V\ (vs.\ Li/Li^+)$

(Eq 3.3) $Sn(s) + xLi^+ + xe^- \rightarrow Li_xSn(s) \qquad\qquad E \approx 0.15\ V\ (vs.\ Li/Li^+)$
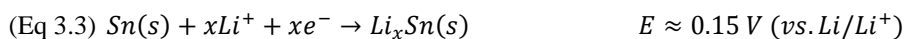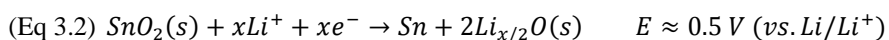
During the anodic curve, the peak at 0.5 V corresponds to the de-alloying of Li_xSn.

Oxidation of Sn into SnO and further into SnO_2 occur at about 1.25 V and 1.9 V

[65,96]. It seemed that the SnO_2 was formed in oxygen environment because the

deposition potential of Sn is close to the reduction potential of CuO during Sn

deposition (Figure 3.24). In addition, Li$_2$O originated from lithiation of CuO reacts with Sn during delithiation process, so SnO$_2$ can be formed. This combination reaction with Sn and Li$_2$O occurs in the boundary region and enough to observe the peak intensities due to the large surface area. After the 1st cycle of f_Sn/CuO NWs electrode, the CV curves were maintained, thus the NW alleviated the stress induced by volume change and fading of active materials.

To investigate the effect of nanowires on the cycle performance, the specific capacity and Coulombic efficiency of the electrodes were observed. The theoretical capacity of f_Sn/CuO NWs electrode was calculated by following equation.

(Eq 3.4) $C_{Sn/CuO\ NWs} = C_{Sn} * X_{Sn} + C_{CuO} * X_{CuO}$

C$_{Sn}$ and C$_{CuO}$ are theoretical capacity of Sn (994 mAh/g) and CuO (675 mAh/g), respectively. X$_{Sn}$ and X$_{CuO}$ are mass ratio of Sn and CuO in f_Sn/CuO NWs electrode. The amounts of Sn and CuO were 0.079 and 0.273 mg/cm^2 on the f_Sn/CuO NWs electrode. So, C$_{Sn/CuO\ NWs}$ was obtained 746.8 mAh/g. Figure 3.25 shows the specific capacity and Coulombic efficiency of f_Sn film and f_Sn/CuO NWs electrodes. The initial discharge capacity of f_Sn film electrode was 296.4 mAh/g and Coulombic efficiency was 82.7%. The low reversible capacity of f_Sn film electrode compared to the theoretical capacity (994 mAh/g) is originated from the thickness of Sn layer

[97]. As the thickness increased, severe deterioration of f_Sn film electrode exacerbates capacity and retention. The thickness of Sn film was estimated about 1 μm from calculation. However, the f_Sn/CuO NWs electrode showed the discharge capacity of 1048.3 mAh/g for the 1st cycle. The Coulombic efficiency of f_Sn/CuO NWs electrode (78.9%) was little lower than that of Sn film electrode, indicating that more irreversible capacity was required. The irreversible capacity loss seen from the 1st cycle is generally attributed to the formation of a solid electrolyte interphase (SEI). It indicated that electrolyte was consumed in f_Sn/CuO NWs electrode due to the large surface area of nanowires. After the 1st formation cycle, the Coulombic efficiency was recovered up to 98%. The discharge capacity of f_Sn/CuO NWs electrode at 70th cycle was 729.0 mAh/g which was 89% retention compared to initial capacity with 1 C-rate. This result is comparable to the Sn-based electrodes that have been recently reported in other literatures (Figure 3.26). Generally, if the surface area is increased to relieve the stress during cycling, the initial efficiency is lowered because irreversible capacity from SEI formation is enlarged. Figure 3.26 (c) is a graph summarizing Figure 3.26 (a) and (b). Although the capacity at 70th cycle and the Coulombic efficiency at formation cycle are inversely proportional to each other, the results of this study showed that the capacity was enlarged with high Coulombic

efficiency at formation cycle on the dotted line in Figure 3.26 (c).

The f_Sn film electrode showed increasing tendency of capacity until 50th cycle due to activation of Sn with Li-ion during cycling and the capacity decreased afterwards. It was presumed that the effect of Sn activation was predominant at the early cycles, whereas deterioration of Sn film overwhelmed the activation effect at later cycles, resulting in the capacity fading. The fading was mostly ascribed to the stress during the insertion/extraction of Li-ion and successive pulverization. Meanwhile, f_Sn/CuO NWs electrode showed better capacity retention than f_Sn film electrode. It was expected that 1-D nanowire secured the efficient charge transport, and the large surface area dissipated the stress induced by the volume change during cycling.

Based on the experimental results, the theoretical capacity was compared with the experimental capacity to see if CuO and Sn in the electrode reacted properly with Li-ion. As shown in Figure 3.14, the mass of CuO and Sn in the Sn/CuO NWs electrode was 0.273 mg/cm^2 and 0.079 mg/cm^2, respectively. By multiplying the theoretical capacity (CuO: 675 mAh/g and Sn: 994 mAh/g), CuO and Sn showed 1843 mAh/cm^2 and 0.0785 mAh/cm^2, respectively, which were 70.1% and 29.9% of the total capacity. The potential ranges of Sn and CuO to react with Li-ion was

examined to obtain practical capacity. Figure 3.23 shows the CV results of the Sn electrode and CuO NWs electrode. It was confirmed that Sn reacted mainly at 0.5 V or lower and CuO reacted at 0.5 V or higher. In addition, some CuO reacted at less than 0.5 V, indicating that about 13.2% of the total capacity reacted through the potential profile in Figure 3.27. Therefore, it can be expected that 100/86.8 times of the capacity of Sn/CuO NWs electrode reacted above 0.5 V was for CuO, and the remainder was capacity for Sn. This showed in Figure 3.27 (b) and practical capacity ratio of CuO and Sn were 72.4% and 27.6%, respectively. Therefore, it was confirmed that CuO and Sn in the Sn/CuO NWs electrode reacted well with Li-ion.

Figure 3.28 shows the EIS results of f_Sn film, f_CuO NWs and f_Sn/CuO NWs electrodes at the 1st and the 50th cycle. The f_Sn/CuO NWs have 1-D nano-structure, so the diffusion length of Li-ion is short and the Cu located between CuO and Sn enhances the electrical conductivity as confirmed in XPS and TEM results. Table 3.6 represents the resistance values of three electrodes at 1st and 50th cycle. The charge transfer resistance of f_Sn/CuO NWs electrode was much lower than that of f_Sn film electrode. Moreover, the resistance of f_Sn film electrode was increased remarkably after the 50th cycle due to the exfoliation of f_Sn film electrode and unceasing formation of SEI at exposed surface, whereas the charge transfer

resistance of f_Sn/CuO NWs electrode was almost unchanged.

Figure 3.29 displays the FE-SEM surface images of f_Sn film and f_Sn/CuO NWs electrodes before and after cycling. In Figure. 3.29 (c), the f_Sn film electrode was pulverized after 70th cycle and the rough surface of Sn and cracked area could be observed. However, the f_Sn/CuO NWs electrode maintained the initial morphology of nanowire shape after 70th cycle, as shown in Figure 3.29 (d). The diameter of Sn/CuO NWs after 70th delithiation was 415.1 ($\pm$ 53.1) nm associated with 182% of initial length.

The nanowire structure of Sn/CuO markedly affects the rate capability by increasing the active site of Li-ion insertion, as shown in Figure 3.30. Because the low internal resistance (Figure 3.28) assists the capacity retention at high current charge and discharge, the nanowire structure maintained the capacity better in harsh condition. The reversible discharge capacity decreases to 1001, 889, 828, 754, 671, 560, and 424 mAh/g at 0.1 C, 0.5 C, 1 C, 2 C, 4 C, 8 C, and 16 C-rate, respectively. The cycle retention of f_Sn/CuO NWs electrode retained about 56% of capacity at 16 C-rate and recovered the capacity as high as 909 mAh/g (91% retention) when the C-rate returned to 0.1 C.

In summary, the binder-free f_Sn/CuO NWs electrode by means of anodization

and electrochemical deposition was successfully fabricated. The 1-D nanowire consists of CuO, Sn, and Cu enhancing the electron pathway. The f_Sn/CuO NWs electrode showed outstanding cycle retention during 70 cycles and from the CV result, Sn was well reacted with Li-ion during cycles. The electrode has good rate capability compared to f_Sn film electrode.

Table 3.5. Area Percentage of Peaks Measured in XPS Results (Figure 3.16) and

Calculated Atomic Percentage of Cu, Cu^+ and Cu^{2+}

	Area percentage / %		Atomic percentage / %		
	(1) + (2) + (3)	(4)	Cu	Cu^+	Cu^{2+}
f_Cu(OH)$_2$ NWs Cu 2p	85.5	14.5	14.5	-	85.5
f_CuO NWs Cu 2p	78.1	21.9	14.5	7.4	78.1
f_Sn/CuO NWs Cu 2p	68.3	31.7	>24.3	<7.4	68.3
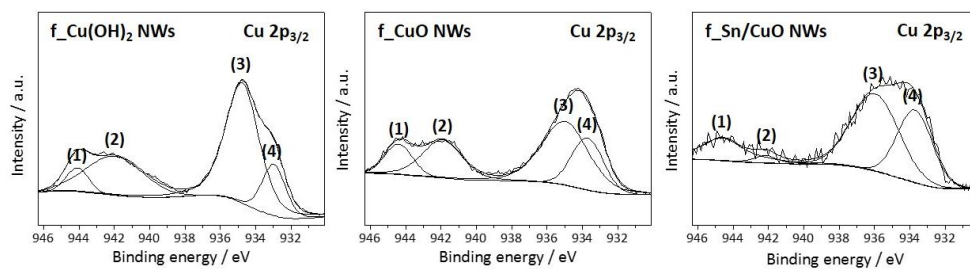
Table 3.6. Resistance Values of f_Sn film Electrode, f_CuO NWs Electrode, and

f_Sn/CuO NWs Electrode at 1st and 50th Cycle

Resistance (Ω)	Cycle	R$_{sol}$	R$_{SEI}$	R$_{CT}$
f_Sn film	1st	4.92	1.85	157.5
	50th	3.53	48.51	500.1
f_CuO NWs	1st	5.08	6.98	147.8
	50th	3.44	26.66	254.5
f_Sn/CuO NWs	1st	4.88	7.5	87.58
	50th	3.27	13.43	234.5
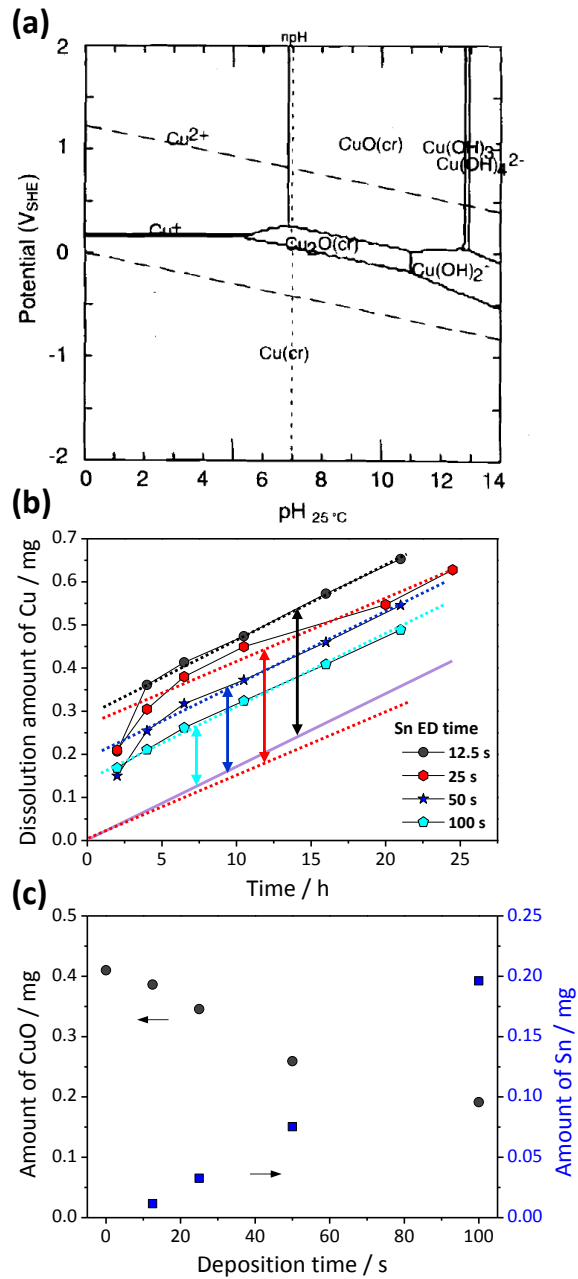
Figure 3.14. (a) Pourbaix diagram of Cu [104] and (b) ICP-AES results of Cu

elements amount in f_Sn/CuO NWs electrode according to the dissolution time in 1

vol% HNO$_3$ and (c) the amount of CuO and Sn elements according to Sn ED time.
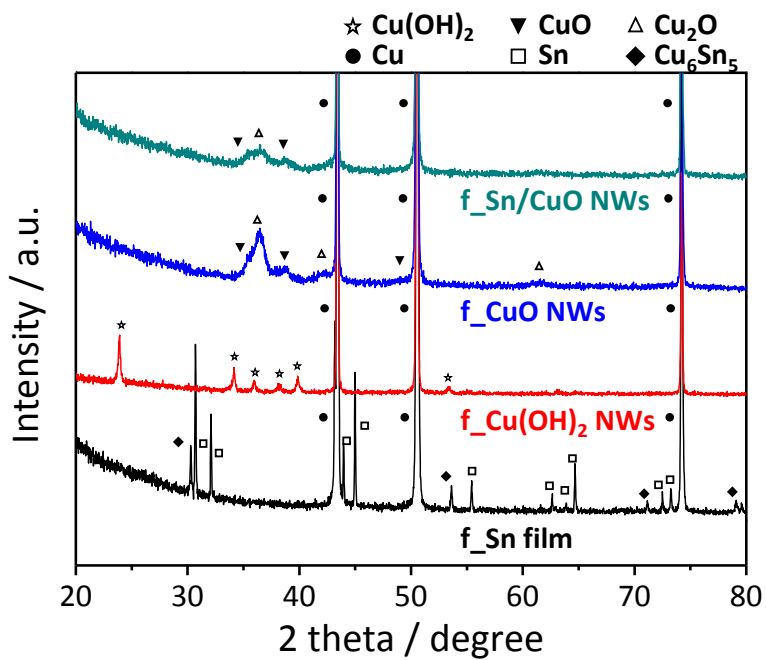
Figure 3.15. XRD patterns of f_Sn film electrode, f_Cu(OH)$_2$ NWs electrode, f_CuO

NWs electrode, and f_Sn/CuO NWs electrode.
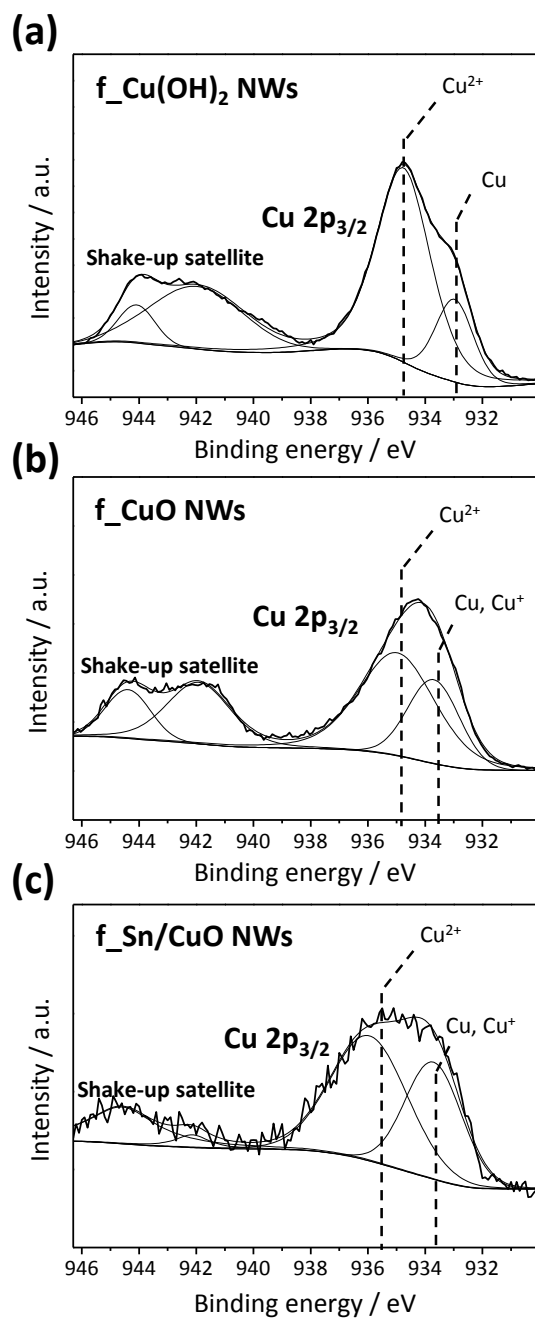
Figure 3.16. XPS Cu 2p spectrum of (a) f_Cu(OH)$_2$ NWs electrode, (b) f_CuO NWs

electrode, and (c) f_Sn/CuO NWs electrode.
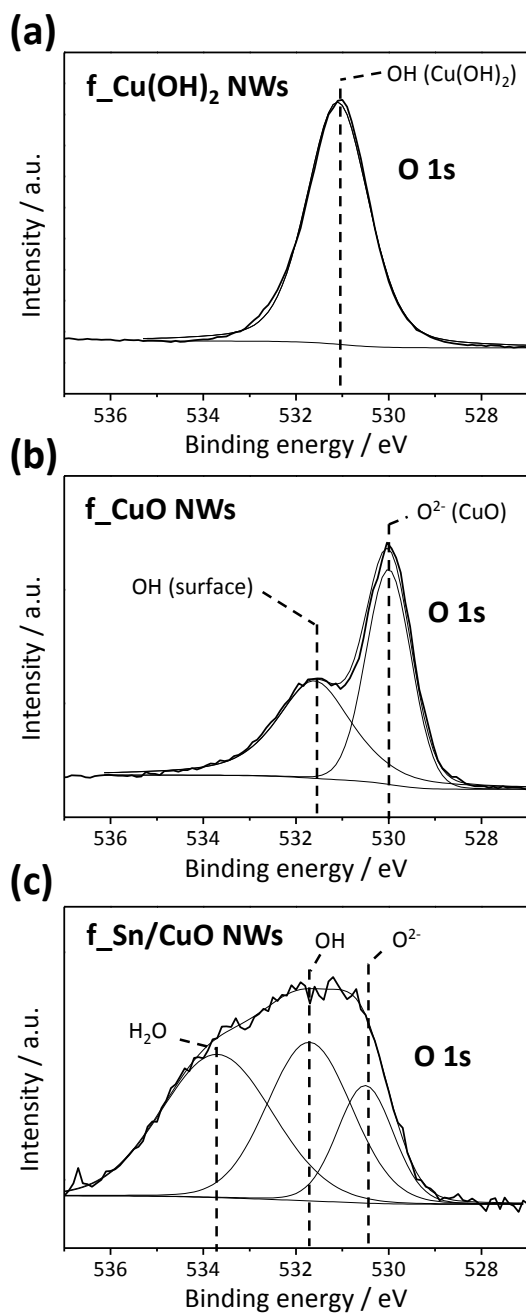
Figure 3.17. XPS O 1s spectrum of (a) f_Cu(OH)₂ NWs electrode, (b) f_CuO NWs

electrode, and (c) f_Sn/CuO NWs electrode.
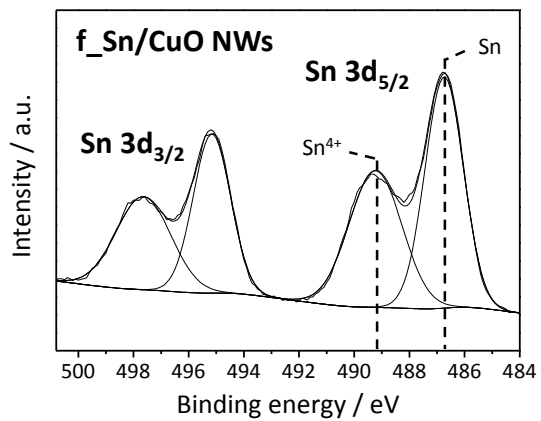
Figure 3.18. XPS Sn 3d spectrum of f_Sn/CuO NWs electrode.
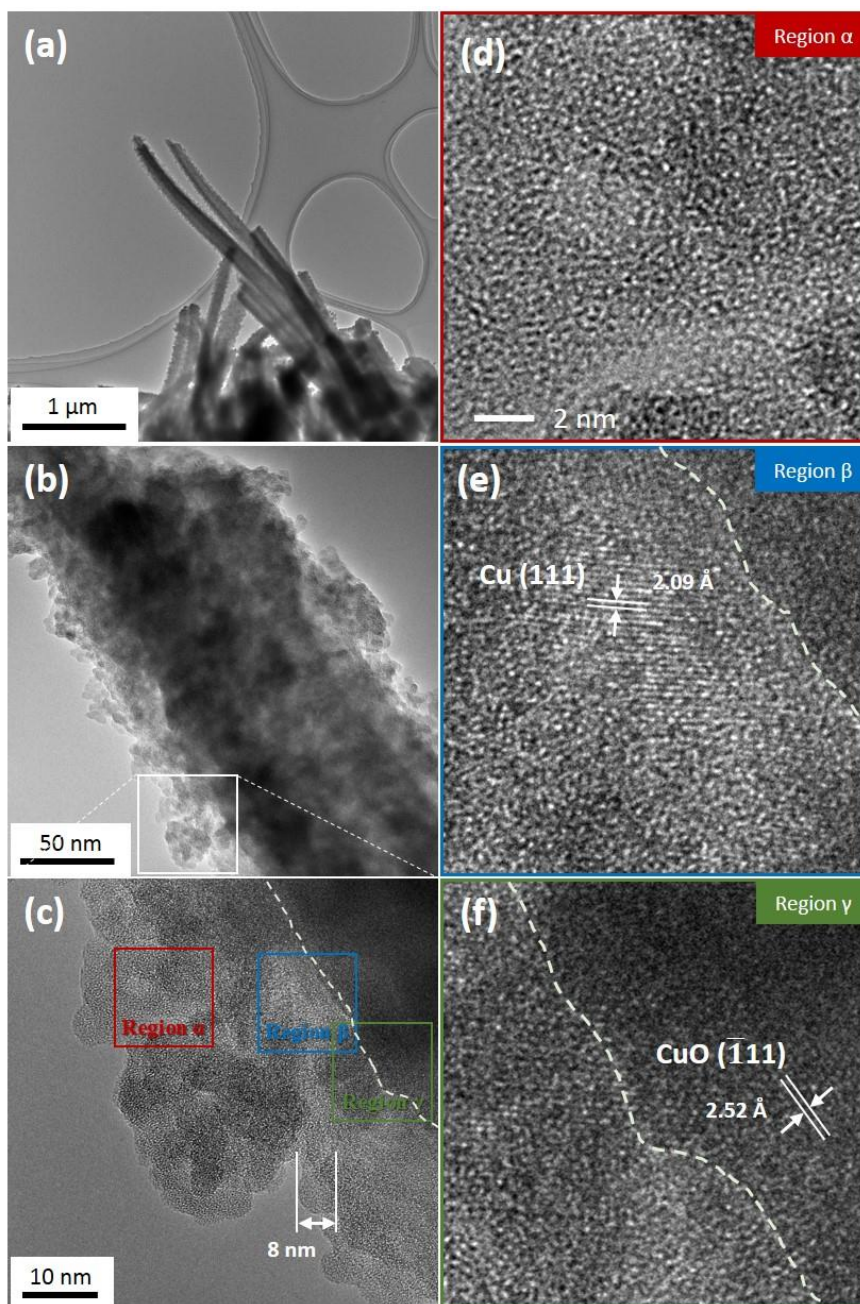
Figure 3.19. TEM images of (a, b, c) Sn/CuO NWs and high magnification images

with (d) region α (Sn), (e) region β (Cu), and (f) region γ (CuO).
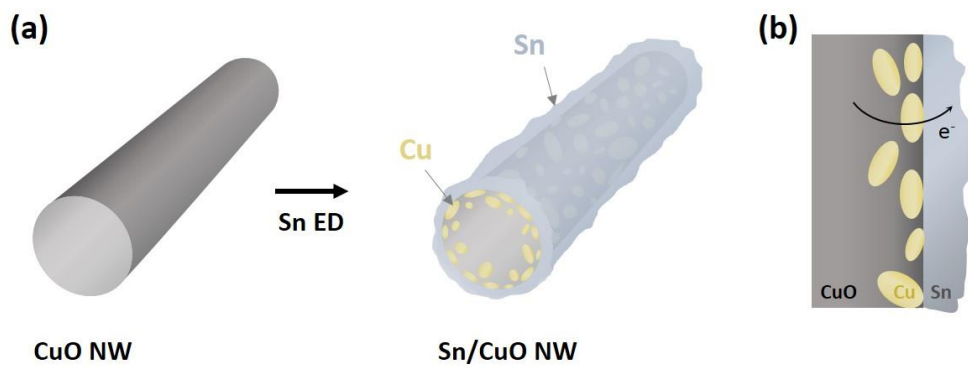
Figure 3.20. Schemes of (a) CuO NW and Sn/CuO NW and (b) electron pathway

around outer surface of Sn/CuO NW.
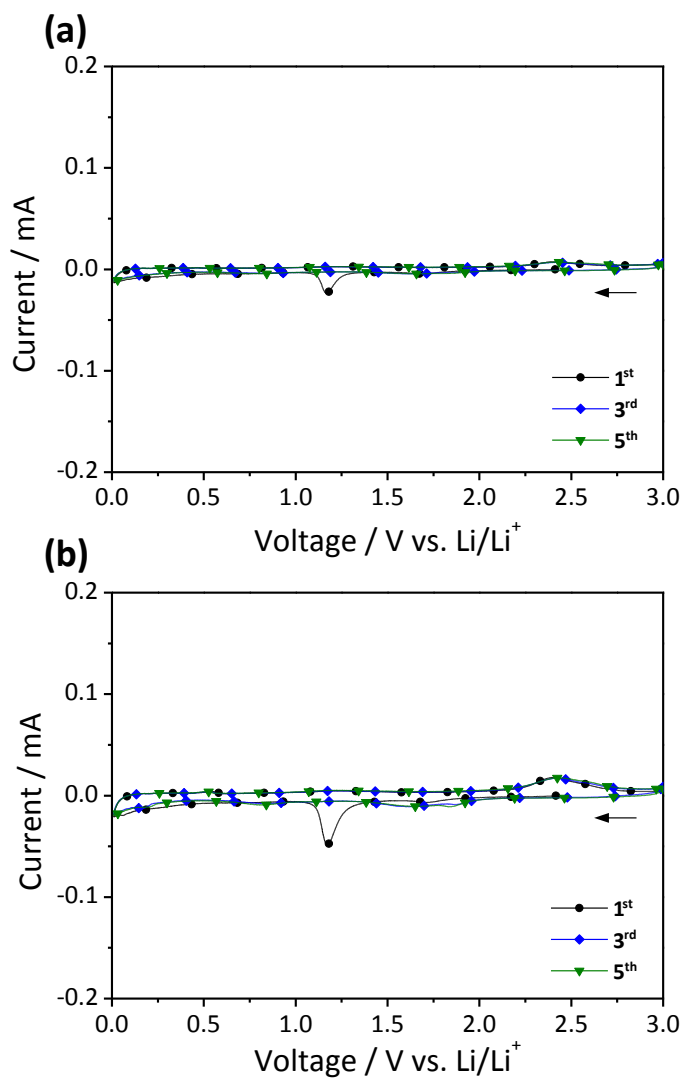
Figure 3.21. Cyclic voltammograms of f_CuO NWs electrode after twice reduction

with (a) linear sweep voltammetry (20 mV/s) and (b) chronopotentiometry (-10

mA/cm^2) at scan rate of 0.1 mV/s for 5 cycles.
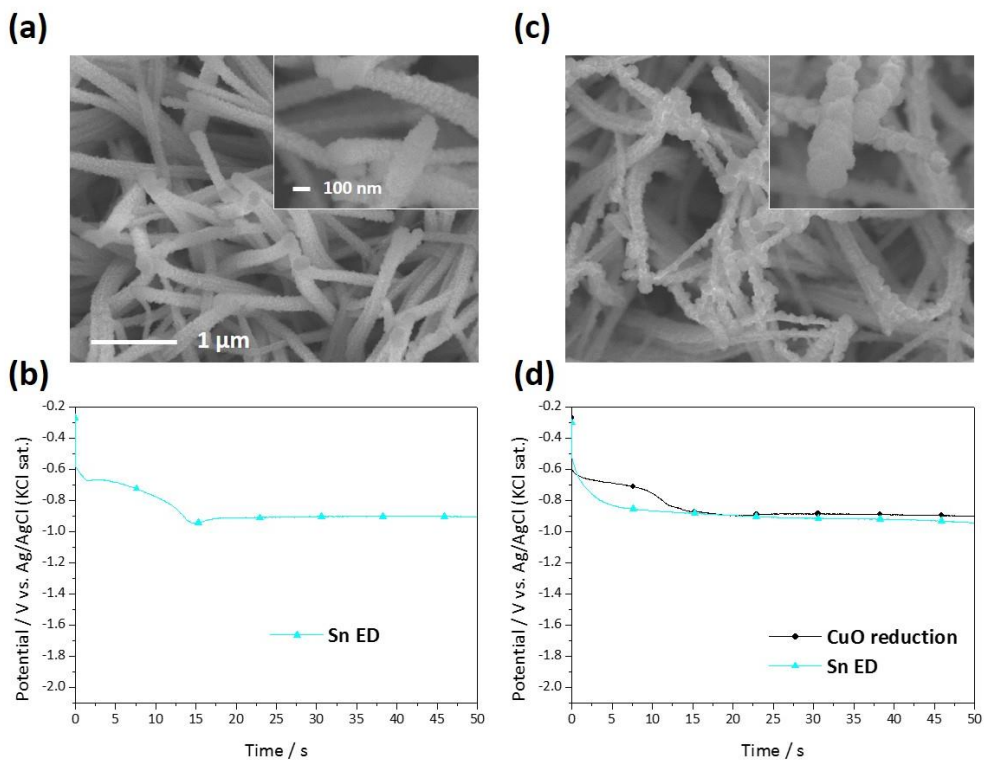
Figure 3.22. (a) FE-SEM surface image of electrodeposited Sn on f_CuO NWs electrode and (b) potential profile during Sn ED. (c) FE-SEM surface image of electrodeposited Sn on f_CuO NWs electrode after reduction of f_CuO NWs electrode with -10 mA/cm^2 for 50 s and (d) potential profiles during reduction of f_CuO NWs electrode and Sn ED.
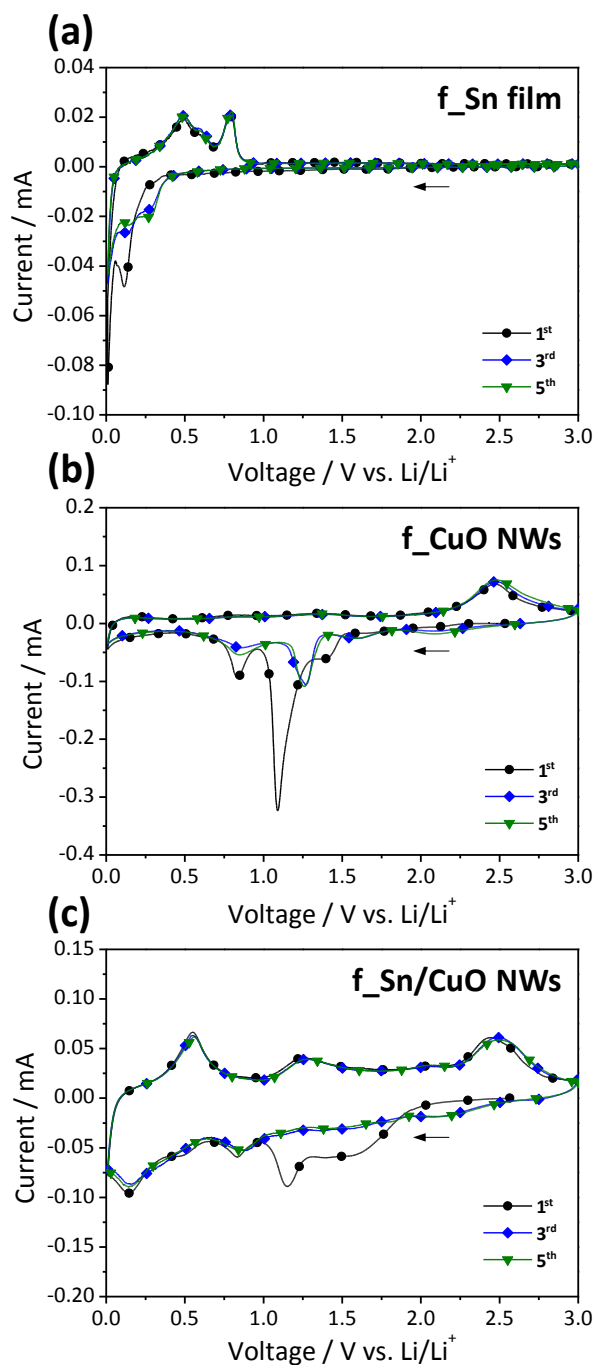
Figure 3.23. Cyclic voltammograms of (a) f_Sn film electrode, (b) f_CuO NWs electrode, and (c) f_Sn/CuO NWs electrode at scan rate of 0.1 mV/s.
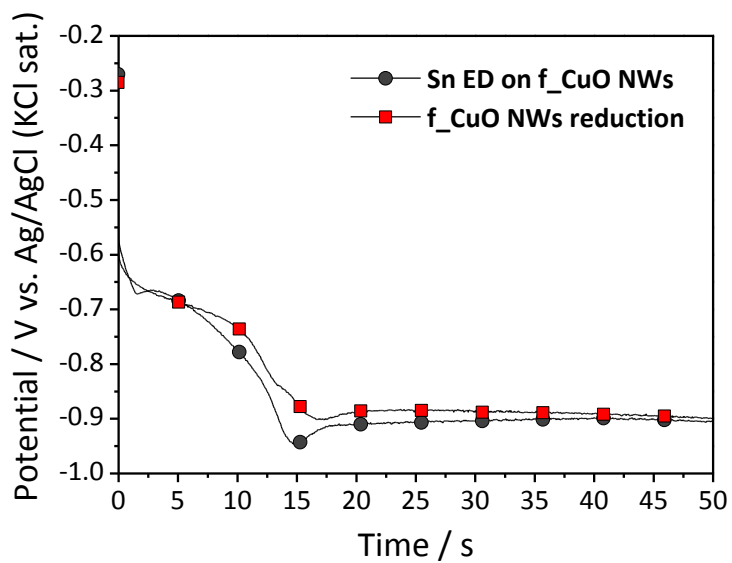
Figure 3.24. Potential profiles of Sn ED on f_CuO NWs electrode and reduction of

f_CuO NWs electrode at same chronopotentiometry with -10 mA/cm^2.
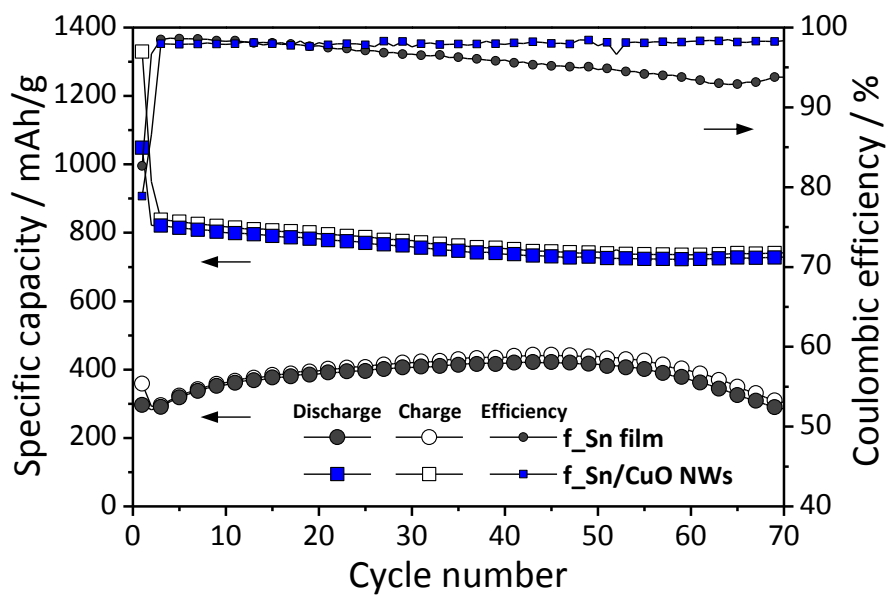
Figure 3.25. Specific capacity and Coulombic efficiency of f_Sn film electrode and

f_Sn/CuO NWs electrode at 0.1 C-rate for the formation step followed by 1 C-rate

cycling.
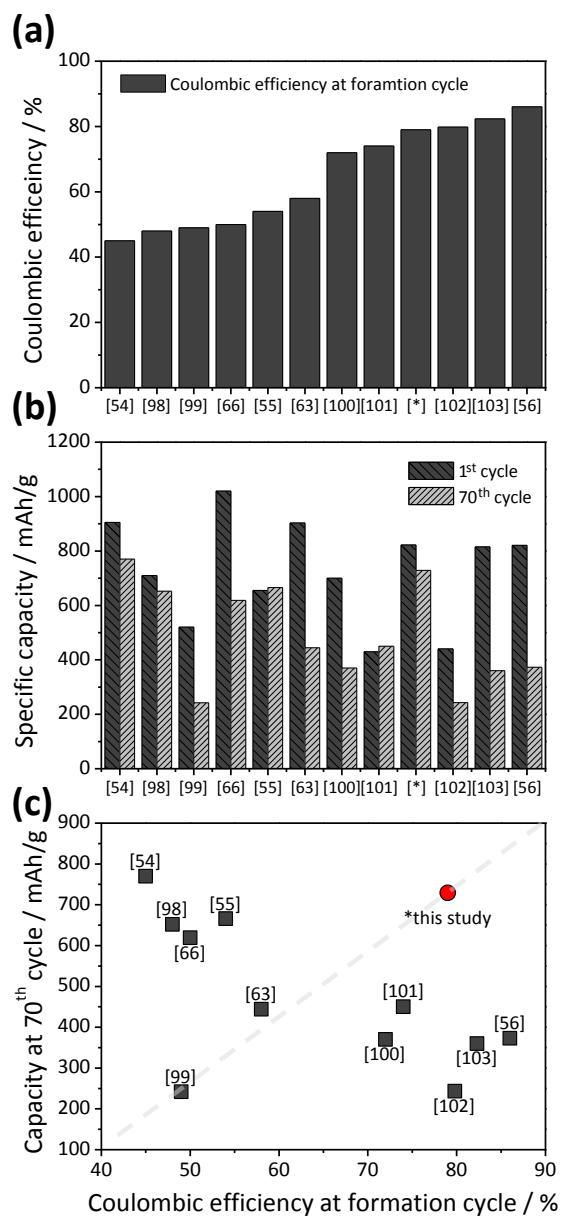
Figure 3.26. Information of several Sn-based electrodes reported in the literatures of

[54], [55], [56], [63], [66], [98], [99], [100], [101], [102], [103], and this study [*].

(a) Coulombic efficiency, (b) specific capacity at 1st and 70th cycle, and (c)

Coulombic efficiency at formation cycle vs. capacity at 70th cycle plot.
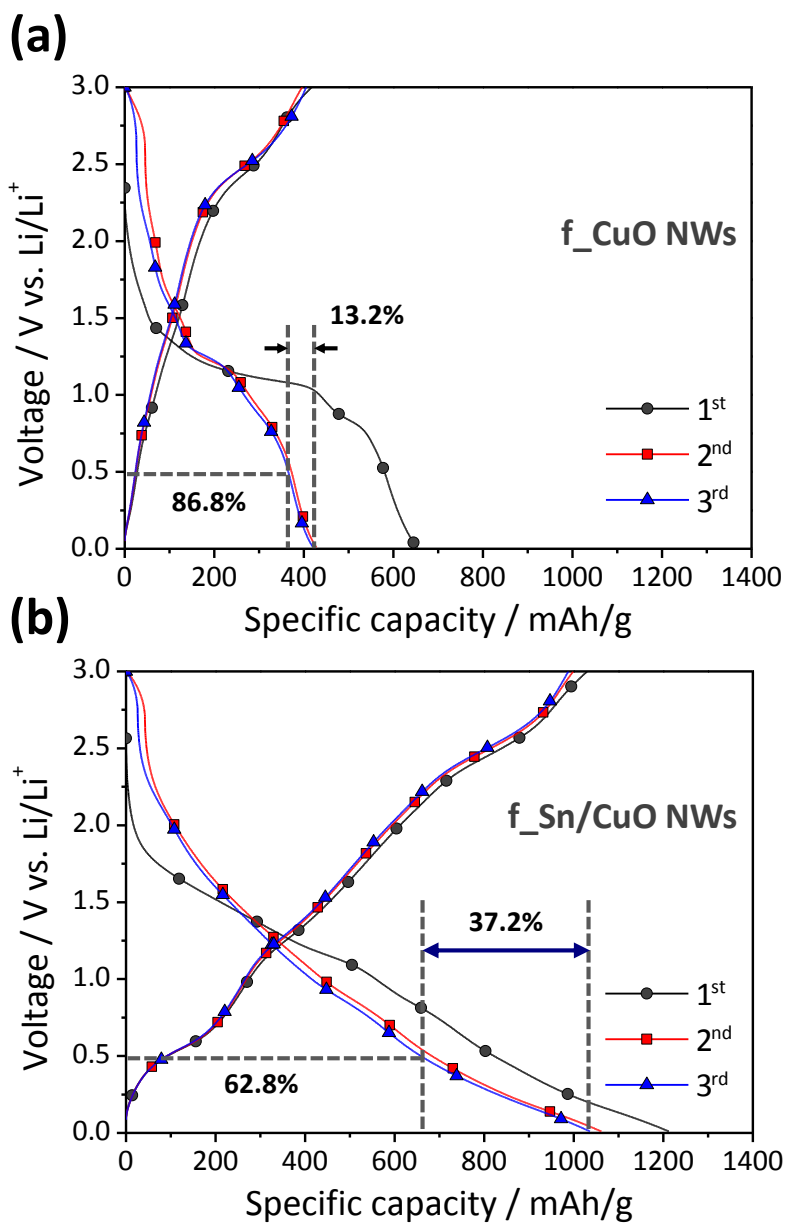
Figure 3.27. Voltage profiles of (a) f_CuO NWs electrode and (b) f_Sn/CuO NWs

electrode at first three cycles during cyclic voltammetry with scan rate of 0.1 mV/s.
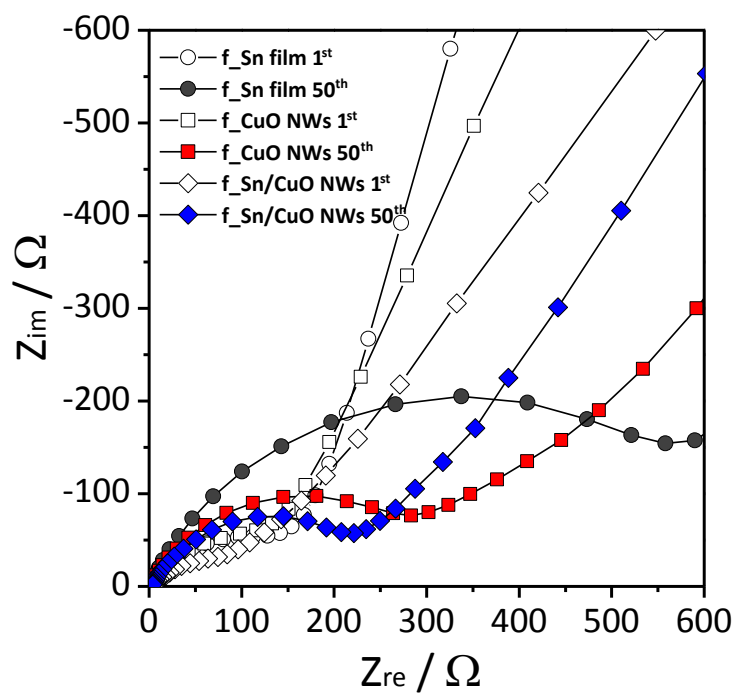
Figure 3.28. EIS analysis of f_Sn film electrode, f_CuO NWs electrode and f_Sn/CuO NWs electrode at 1st and 50th cycle.
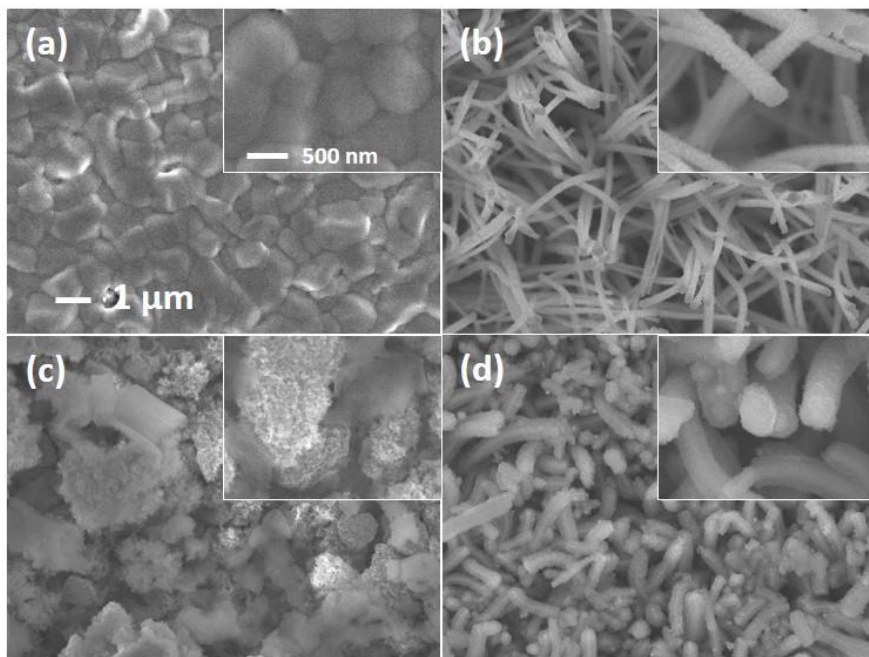
Figure 3.29. FE-SEM surface images of (a, c) f_Sn film electrode and (b, d)

f_Sn/CuO NWs electrode before cycle and after 70th cycle, respectively.
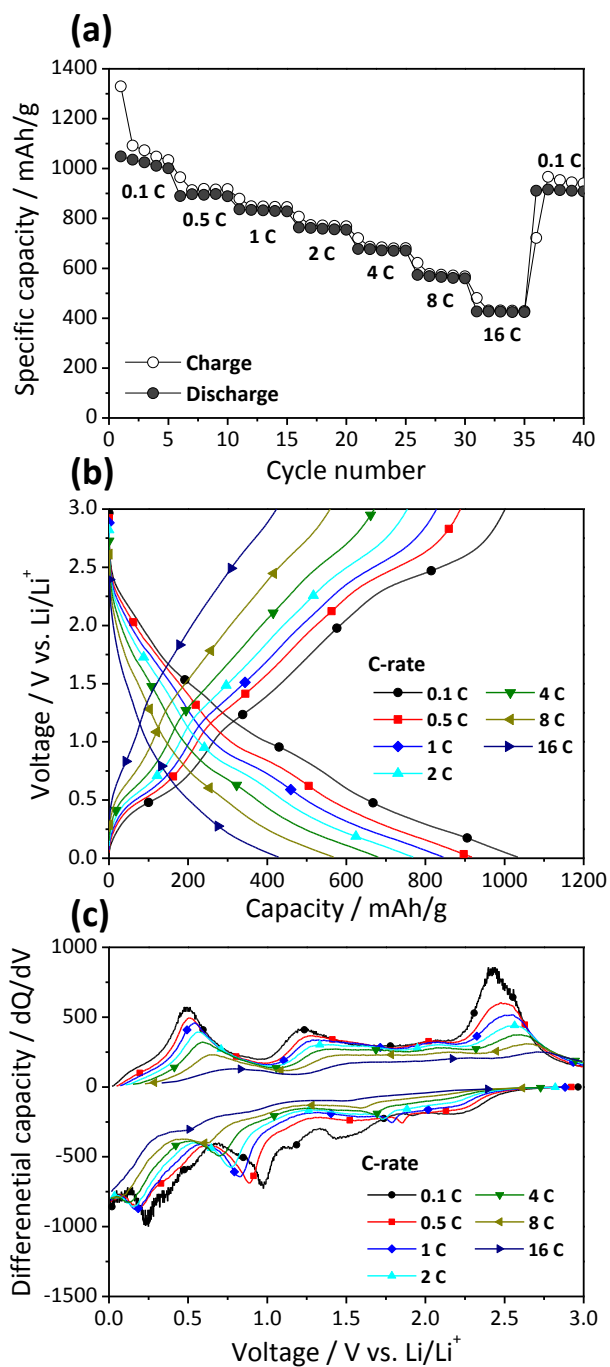
Figure 3.30. (a) Rate capability, (b) voltage profile, and (c) differential capacity of

f_Sn/CuO NWs electrode with 0.1, 0.5, 1, 2, 4, 8, and 16 C-rate.

1 1 2

3.3. Sn/CuO nanowires electrode on patterned substrate

3.3.1. Long-term cycling stability of Sn/CuO nanowires electrode on Cu foil

In previous section 3.2, the f_Sn/CuO NWs electrode showed the improved cycle characteristics due to stress relaxation originated from enlarged surface area and resistance reduction resulted from nanowire structure. However, after 100th cycle, a unique behavior was observed. Figure 3.31 exhibits the specific capacity with f_Sn/CuO NWs electrode up to 200th cycle. It was observed that capacity suddenly decreased around 100 cycles and continuously decreased to 200 cycles. The discharge capacity of f_Sn/CuO NWs electrode at 200th cycle was 550 mAh/g which was 68% retention compared to initial capacity with 1 C-rate. In order to analyze the abrupt capacity fading, the surface of the f_Sn/CuO NWs electrodes which was cycled with 100th cycle and 200th cycle were observed by FE-SEM. The nanowire structure could not be maintained and aggregated as shown in Figure 3.32. Figure 3.32 (a, b) shows the surface morphology of f_Sn/CuO NWs electrode after 100th cycle. At low magnitude images, it seemed that the surface looked like film. There

are agglomerated nanowires and many cracks on the surface. After 200th cycle, the surface of the electrode was severely fade, as shown in Figure 3.32 (c, d). This was due to the combination of conversion and alloying reactions during lithiation and delithiation and structure collapse and aggregation between adjacent nanowires.

The main cause for nanowire aggregation was likely to pressing step when the coin cell was assembled with cell body and cell cap. Figure 3.33 (a) shows schematic presenting visually that the nanowires are laid down by squeezing, which is able to promote degradation. In this state, the structure could maintain up to 70th cycle, however, as the cycle progresses afterwards, the structure gradually became recombination and collapsed. In order to improve this problem, a method of mitigating the pressing phenomenon of the nanowires during the cell assembly was required. So, the patterned substrate which was fabricated in section 3.1.1 was applied. Among the patterned substrates, pyramid-patterned substrate having 100 μm width (P-100) which showed the most increased surface (+40%) was used. The expected structure shows in Figure 3.33 (b) which can maintain the nanowire structure well, so that good cycle performance was anticipated.
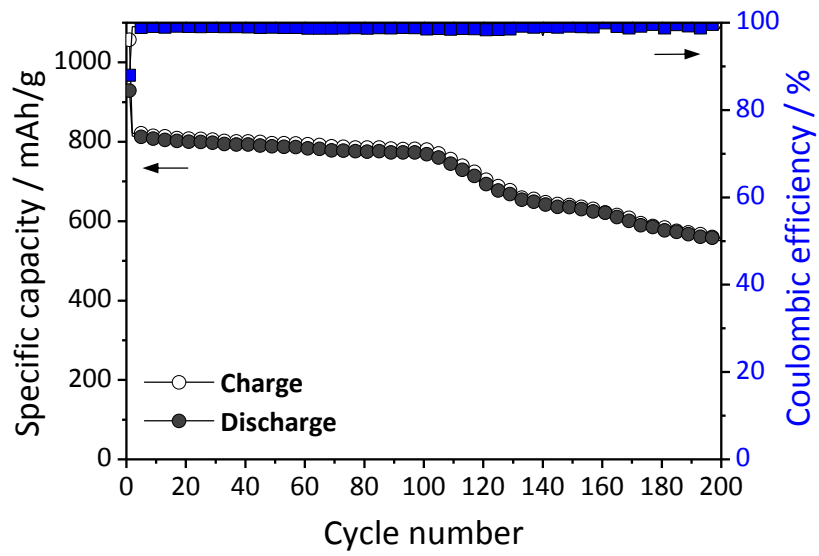
Figure 3.31. Specific capacity and Coulombic efficiency of f_Sn/CuO NWs electrode up to 200th cycle at 1 C-rate.
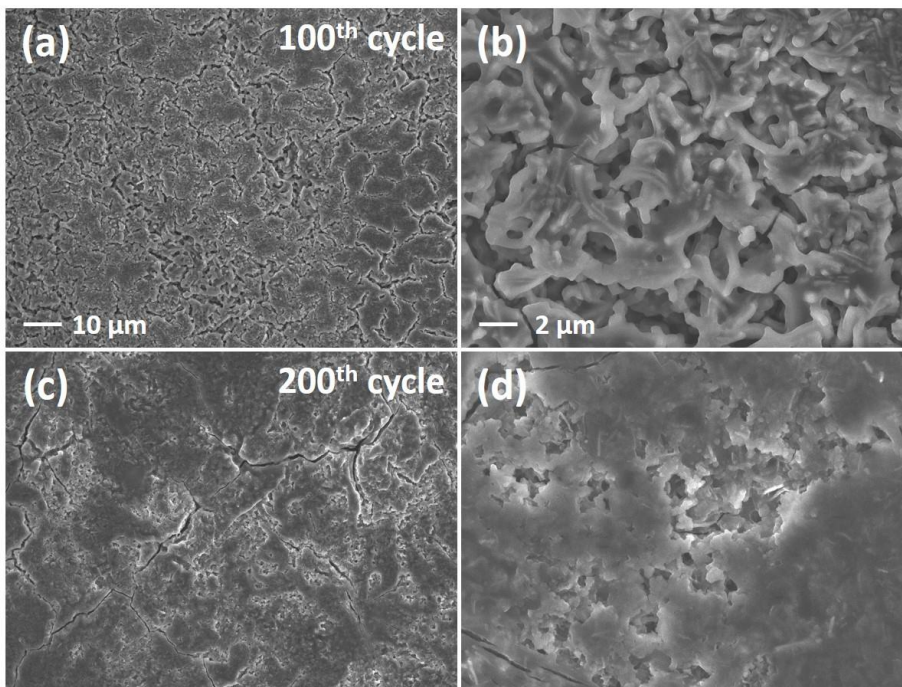
Figure 3.32. FE-SEM surface images of f_Sn/CuO NWs electrode after (a, b) 100th cycle and (c, d) 200th cycle.
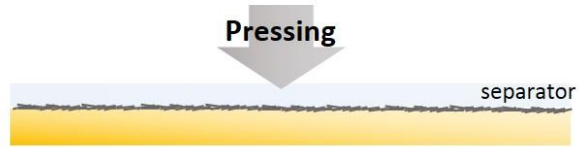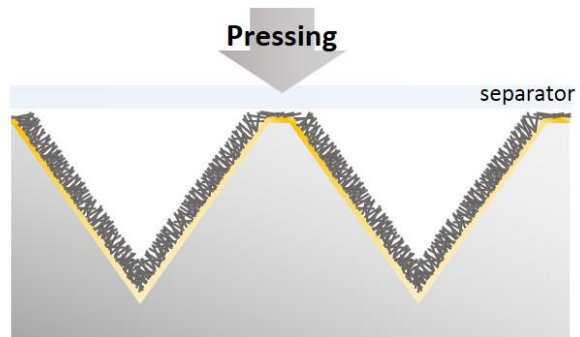
Figure 3.33. Schematics of cross-sectional view in case of (a) f_Sn/CuO NWs electrode and (b) p_Sn/CuO NWs electrode which consists of Sn/CuO NWs electrode and pyramid-patterned substrate.

3.3.2. Preparation of Sn/CuO nanowires electrode on pyramid-patterned substrate

Prior to fabrication of the p_Sn/CuO NWs electrode, the nanowires were formed on plain substrate. The experimental conditions were same as in section 3.1.1, which were TaN/Ta/TaN layer and Cu layer in sequence. In the Cu anodization using the Cu foil, the experiment was carried out with the up-holder system, however, in case of the substrate size with 1 x 1 cm^2, it was difficult to conduct experiment without leakage of the solution. So, the down-holder system was used as shown in Figure 2.5. The substrate was fixed to the RDE with kapton tape shielding the side wall resulting in exposure of only one side of the substrate. Figure 3.34 shows the FE-SEM images of the surface and cross-section with anodization time. Nano rods began to form on the surface and split into nanowires at 75 s. When proceeded up to 300 s, it was confirmed that the nanowires grew more and more and covered the surface. As the anodization progresses, the thickness of the Cu layer decreased due to the dissolution of Cu and after 300 s, the thickness was decreased by ~0.4 μm. This was because Cu was dissolved in anodization to form $Cu(OH)_2$.

Nanowire formation on the patterned substrate was proceeded as shown in Figure

3.35. The patterned substrate of pyramid shape with 100 μm (P-100) was used. In the case of the patterned substrate, the Cu layer at inclined plane was thinner than the horizontal surface during PVD, so that the Cu layer was sufficiently deposited by 4 μm. Figure 3.36 shows FE-SEM images of p_Cu layer, p_Cu(OH)$_2$ NWs electrode, and p_CuO NWs electrode. As can be seen in Figure 3.36 (a), the Cu layer at oblique side was covered by ~2 μm compared to 4 μm at horizontal side. Figure 3.36 (b, d) show the cross-section and surface images of p_Cu(OH)$_2$ NWs electrode, and it was confirmed that the nanowires were successfully grown at concave and convex regions of pyramid-patterned substrate with a length of 5 μm. Figure 3.36 (c, e) show the cross-section and surface images of p_CuO NWs electrode with curved nanowires.

Then, Sn was electrodeposited on p_CuO NWs electrode. However, the Sn was not fully covered on the CuO NWs. Figure 3.37 (a) indicates the schematic of pattern. The pattern was divided by three regions which were top, middle, and bottom, and confirmed the presence of Sn at each position. At 0 rpm with no convection, it was found that Sn was electrodeposited only in the top position except middle and bottom positions. As mentioned before, during Sn electrodeposition, the reduction of CuO also occurred forming oxygen. These oxygen bubbles hindered contact between CuO

NWs and solution resulting in no existence of Sn. Therefore, Sn electrodeposition was carried out with convention increasing rpm to remove oxygen bubbles. Figure 3.37 (b) shows the top, middle, and bottom surface images at 0, 60, 100, and 600 rpm. Square filled with white color means existence of Sn and that with black color means no existence of Sn on nanowires. As the rpm increased, Sn was electrodeposited more and more toward the bottom, rather absence of Sn at top position. So, optimum condition was obtained at 50 rpm between 0 and 600, thus Sn was evenly deposited on top, middle, and bottom positions.
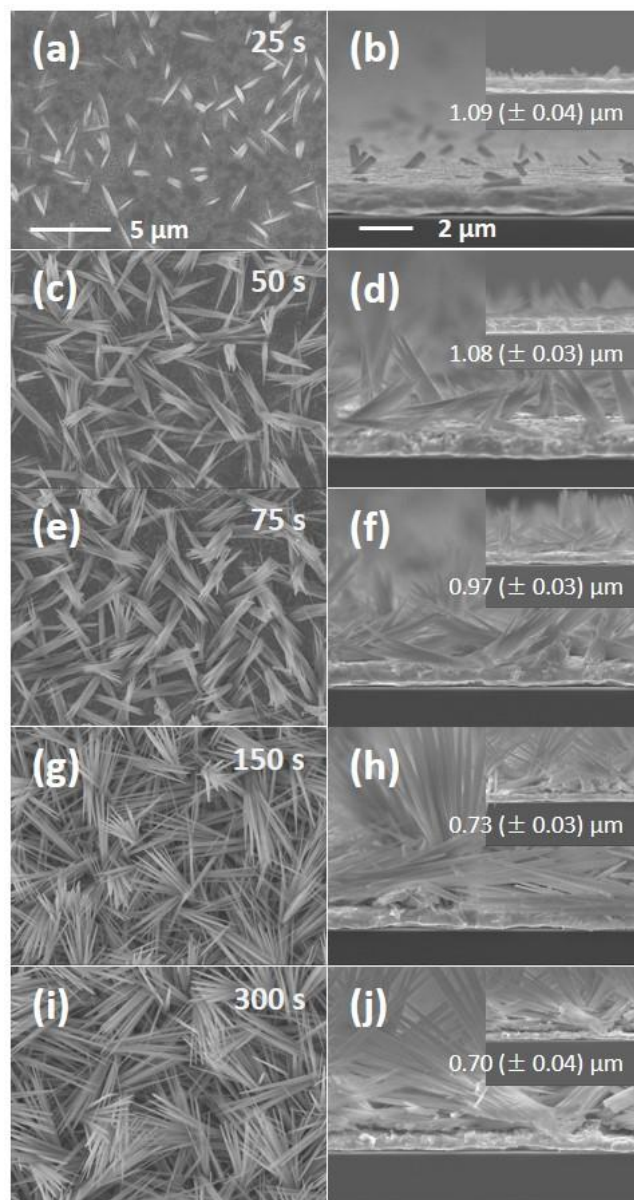
Figure 3.34. FE-SEM surface and cross-sectional images of Sn/CuO NWs anodizing

for (a, b) 25 s, (c, d) 50 s, (e, f) 75 s, (g, h) 150 s, (i, j) 300 s, respectively. Inset shows

a high magnification.
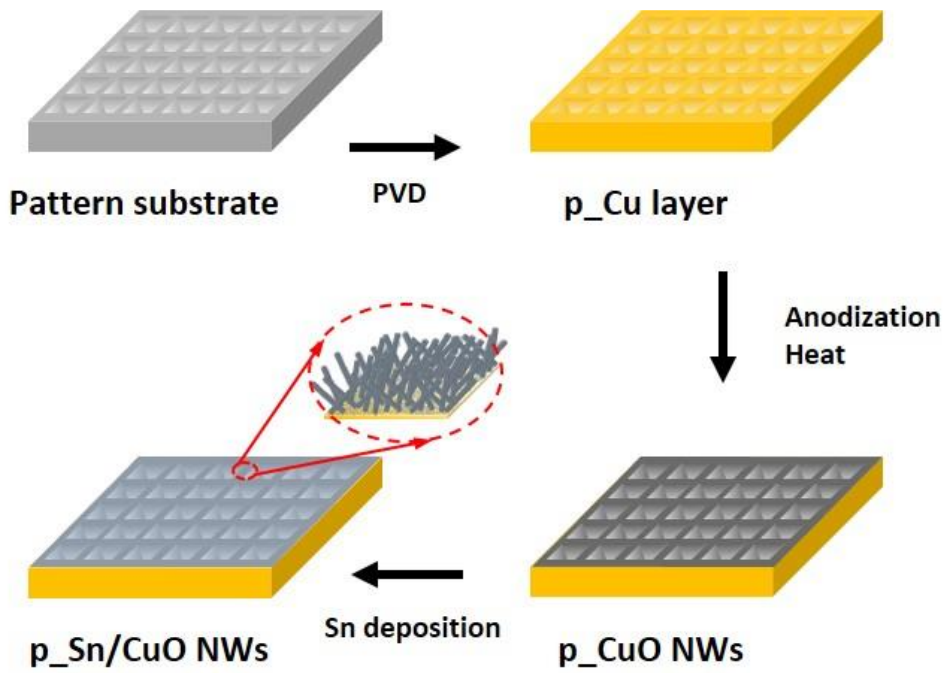
Figure 3.35. Schematic diagram of the fabrication process of p_Sn/CuO NWs electrode.
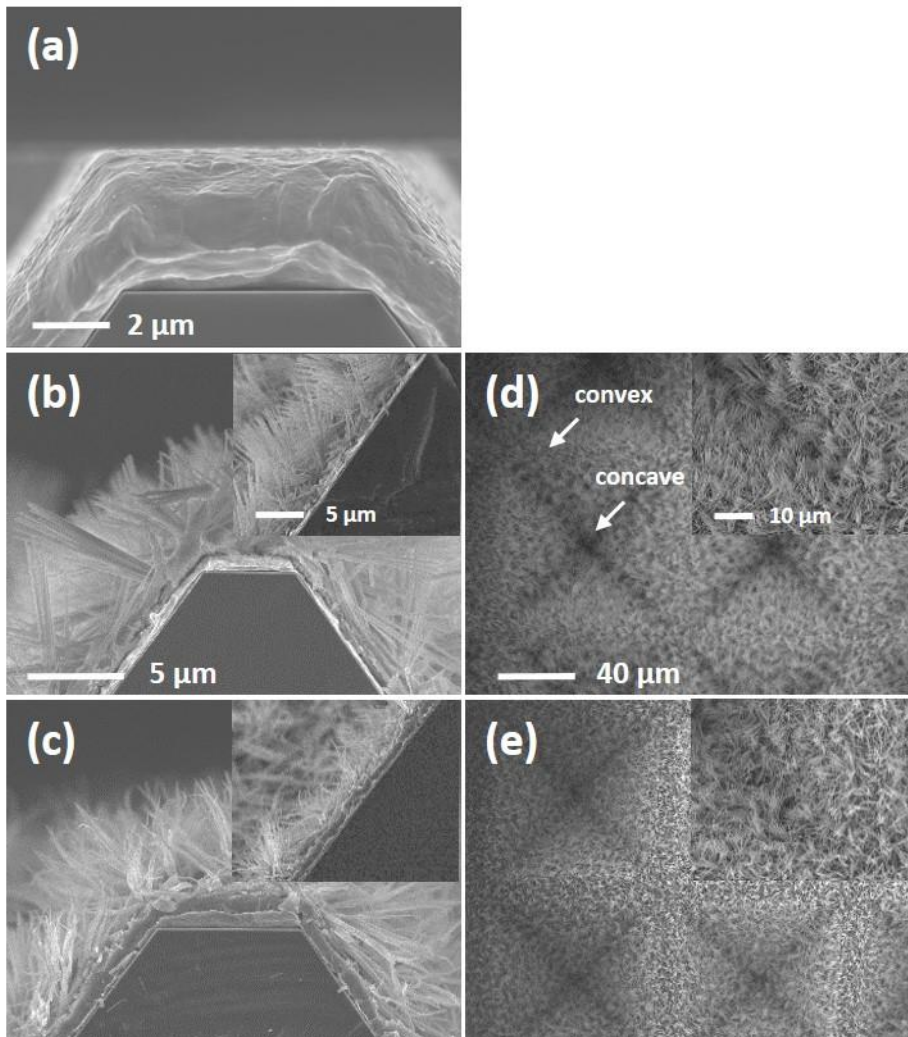
Figure 3.36. FE-SEM cross-sectional images of (a) p_Cu layer, (b) p_Cu(OH)$_2$ NWs,

and (c) p_CuO NWs. The corresponding surface images of (d) p_Cu(OH)$_2$ NWs and

(e) p_CuO NWs. Inset shows a high-magnification.
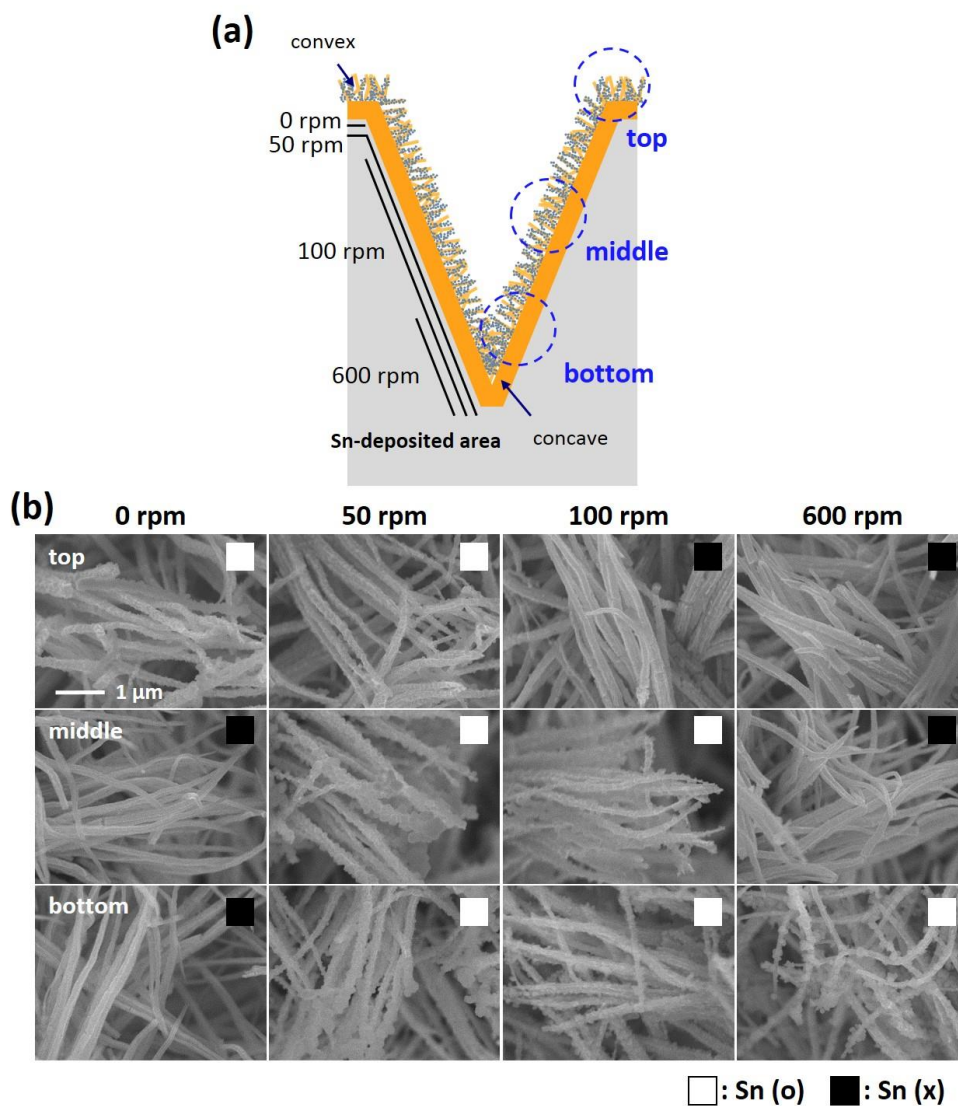
Figure 3.37. (a) Schematic of cross-sectional region of p_Sn/CuO NWs electrode and (b) FE-SEM surface images of top, middle, and bottom region of p_Sn/CuO NWs electrode as indicating in (a). In the FE-SEM images, the square at the right top means the deposited Sn was observed (black) or not (white).

3.3.3. Electrochemical behavior of Sn/CuO nanowires electrode on pyramid-patterned substrate

To investigate the effect of pyramid-patterned substrate on the cycle performance of p_Sn/CuO NWs electrode, the voltage profiles were observed, as shown in Figure 3.38. The f_Sn/CuO NWs electrode and the p_Sn/CuO NWs electrode showed a similar profile. The discharge capacity of p_Sn/CuO NWs electrode was 1201 mAh/g, and the Coulombic efficiency was 78%, indicating large irreversible capacity at formation step. This is because of the enlarged surface area originated from pyramid-patterned substrate. After the formation step, the voltage profile and capacity had a similar trend.

Figure 3.39 shows the specific capacity and Coulombic efficiency of f_Sn/CuO NWs electrode and p_Sn/CuO NWs electrode. The capacity retention of p_Sn/CuO NWs electrode at 1 C-rate for 200 cycles was 92%. The slope was well maintained up to 200th cycle. This was remarkable improvement compared the f_Sn/CuO NWs which showed 68% retention at 200th cycle. It was expected that the patterned substrate alleviated nanowire aggregation providing space. After 200th cycle, the surface morphology was observed as shown in Figure 3.40. Compared to the

f_Sn/CuO NWs electrode at 200th cycle, there were not cracks in top surface and nanowires were well maintained in concave regions. At the top region, though the nanowires were collapsed, severe degradation was not observed.

In summary, the binder-free p_Sn/CuO NWs electrode by means of anodization and electrochemical deposition in the same manner with f_Sn/CuO NWs electrode. As the pyramid-patterned substrate alleviated nanowire aggregation providing space, the long-term stability of the electrode was improved. The p_Sn/CuO NWs electrode showed good cycle retention during 200 cycles with 92% retention at 1 C-rate. This work shows that the p_Sn/CuO NWs electrode has a potential as an anode for high performance Li-ion batteries.
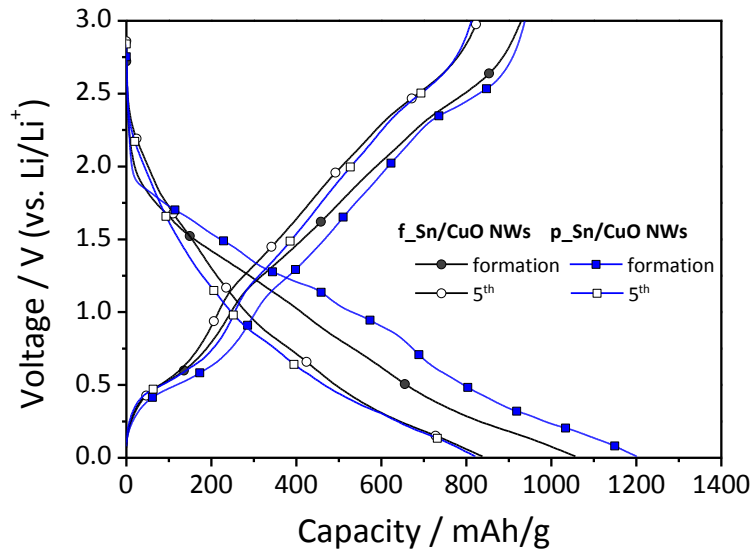
Figure 3.38. Voltage profiles for f_Sn/CuO NWs and p_Sn/CuO NWs electrode at

formation and 5th cycle (formation: 0.1 C-rate, cycling: 1 C-rate).
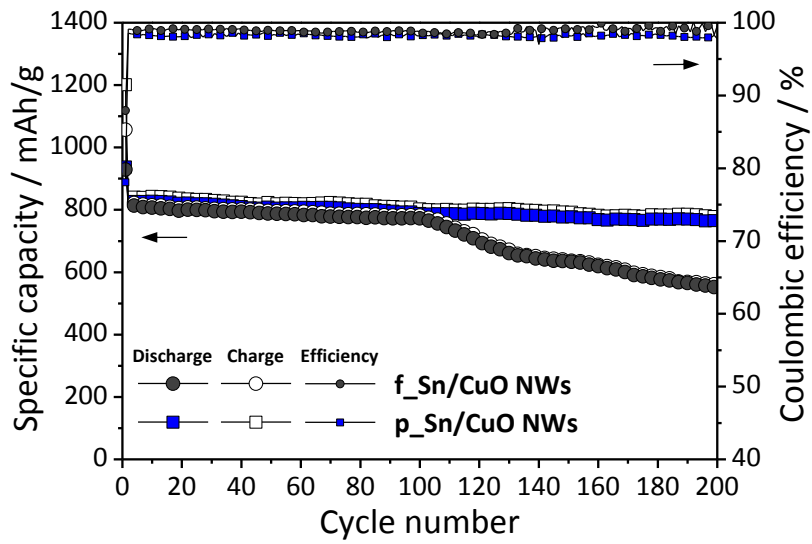
Figure 3.39. Specific capacity and Coulombic efficiency of f_Sn/CuO NWs and

p_Sn/CuO NWs electrode at 0.1 C-rate for the formation cycle followed by 1 C-rate

cycling to 200th cycle.
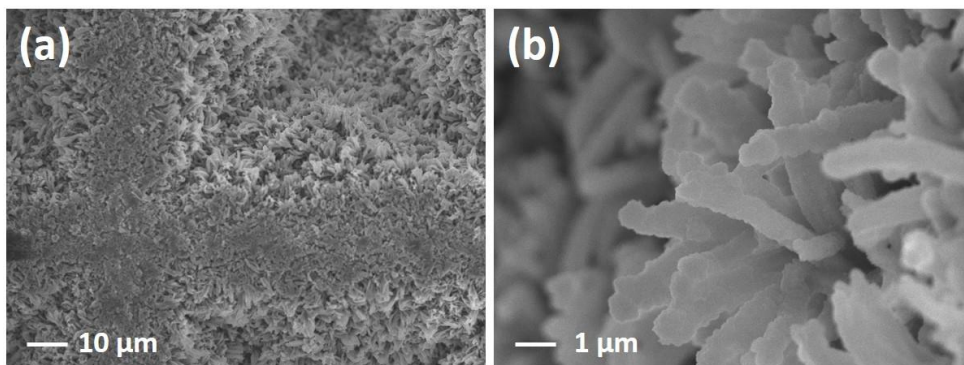
Figure 3.40. FE-SEM surface images of (a) p_Sn/CuO NWs electrode after 200th cycle and (b) magnification at slope region.

CHAPTER IV. Conclusions

In this study, micro-scale and nano-scale refinement of substrate were introduced with MEMS process and electrochemical methods for improving the drawback of nanoscale designs which are low energy density, self-aggregation, and limited electrical conductivity.

A micro-scale patterned substrate was manufactured with Si substrate. The patterned substrate with sawtooth and pyramid shapes showed relaxation effect of stress induced during cycling. Especially, the pyramid patterns increased ~40% of surface area and the concave regions with low Li-ion flux and thin layer effectively enhanced maintenance of the Si active material. The patterns on the substrate improved the rate capability as well as cycleability of the Si film electrode.

A nano-scale modification was also carried out to increase energy density and electrical conductivity. Conducting agent and binder free 1-D nanowires were synthesized on Cu foil by Cu anodization. The nanowires of $Cu(OH)_2$ were converted to CuO with dehydration and Sn was electrodeposited onto the CuO nanowires surface. Because the deposition potential of Sn was similar with CuO reduction, selectively reduced Cu nodes between CuO nanowire and Sn layer can be obtained. The Cu nodes enhanced the electrical conductivity connecting CuO and Sn

due to high conductivity. At 1 C-rate, the Sn/CuO nanowires electrode showed 89% of capacity retention up to 70th cycle. In addition, 56% of capacity retention could be obtained at 16 C-rate. The 1-D nanowire structure and reduced Cu nodes enhanced electrical conductivity resulting in outstanding cycle retention and good rate capability.

However, the Sn/CuO nanowires electrode was not appropriate for long-term stability. At 100th cycle, abrupt decrease of capacity was observed and there were many cracks and aggregated nanowires from surface morphology analysis. This problem was ameliorated by using patterned substrate. The main factor of the problem was collapsed nanowire during cell assembly. So, the patterned substrate that can provide space for nanowires was applied. With the same experimental conditions, Sn/CuO nanowires electrode on patterned substrate was fabricated. The Sn/CuO nanowires electrode on patterned substrate showed good capacity retention up to 200th cycle with 92% of capacity retention which was better than Sn/CuO nanowires electrode on Cu foil. In the same manner, the surface morphology analysis was conducted with Sn/CuO nanowires electrode on patterned substrate after 200th cycle. There was no crack and the 1-D nanowire shape was well maintained. Therefore, combination with micro-scale modification of patterned substrate and

nano-scale modification of 1-D nanowires remarkably enhanced energy density,

electrical conductivity, and suppressed self-aggregation, so that outstanding cycle

performance could be obtained.

REFERENCES

[1] J.-M. Tarascon, M. Armand, *Nature*, **414**, 359 (2001).

[2] M. Armand, J.-M. Tarascon, *Nature*, **451**, 652 (2008).

[3] J. B. Goodenough, K.-S. Park, *J. Am. Chem. Soc.*, **135**, 1167 (2013).

[4] C. M. Julien, A. Mauger, K. Zaghib, and H. Groult, *Inorganics*, **2**, 132 (2014).

[5] P. Kalyani, N. Kalaiselvi, *Sci. Technol. Adv. Mater.*, **6,** 689 (2005).

[6] R. Alcantara, P. Lavela, J. Tirado, E. Zhecheva, and R. Stoyanova, *J. Solid State Electrochem.*, **3**, 121 (1999).

[7] S. Kim, M. Kim, I. Choi, and J. J. Kim, *J. Power Sources*, **336**, 316 (2016).

[8] Q. Zhong, A. Bonakdarpour, M. Zhang, Y. Gao, and J. Dahn, *J. Electrochem. Soc.*, **144**, 205 (1997).

[9] M. R. Palacin, *Chem. Soc. Rev.*, **38**, 2565 (2009).

[10] H. Li, H. Zhou, *Chem. Comm.*, **48**, 1201 (2012).

[11] K. -L. Lee, J. -Y. Jung, S. -W. Lee, H. -S. Moon, and J. -W. Park, *J. Power Sources*, **129**, 270 (2004).

[12] S. W. Lee, M. T. McDowell, J. W. Choi, and Y. Cui, *Nano Lett.*, **11**, 3034 (2011).

[13] J. -H. Min, Y. -S. Bae, J. -Y. Kim, S. -S. Kim, and S. -W. Song, *Bull. Korean Chem. Soc.*, **34**, 1296 (2013).

[14] U. Kasavajjula, C. Wang, A. and J. Appleby, *J. Power Sources*, **163**, 1003 (2007).

[15] M. Yoshio, S. Kugino, and N. Dimov, *J. Power Sources*, **153**, 375 (2006).

[16] H. Jung, M. Park, Y.-G. Yoon, G.-B. Kim, and S.-K. Joo, *J. Power Sources*, **115**, 346 (2003).

[17] H. Morimoto, S. -I. Tobishima, and H. Negishi, *J. Power Sources*, **146**, 469 (2005).

[18] M. Winter, J. O. Besenhard, *Electrochim. Acta*, **45**, 31 (1999).

[19] J. Sangster, C. W. Bale, *J. Phase Equilib.*, **19**, 70 (1998).

[20] D. Larcher, L. Y. Beaulieu, D. D. MacNeil, and J. R. Dahn, *J. Electrochem. Soc.*, **147 (5)**, 1658 (2000).

[21] C. K. Chan, X. F. Zhang, and Y. Cui, *Nano Lett.*, **8**, 307 (2008).

[22] M. He, K. Kravchyk, M. Walter, and M. V. Kovalenko, *Nano Lett.*, **14**, 1255 (2014).

[23] C. -M. Park, S. Yoon, S. -I. Lee, and H. -J. Sohn, *J. Power Sources*, **186**, 206 (2009).

[24] C. J. Wen, R. A. Huggins, *J. Solid State Chem.*, **37**, 271 (1981).

[25] R. A. Huggins, W. D. Nix, *Ionics*, **6**, 57 (2000).

[26] J. K. Lee, W. Y. Yoon, and B. K. Kim, *J. Electrochem. Soc.*, **159**, A1844 (2012).

[27] C. K. Chan, H. Peng, G. Liu, K. Mcilwrath, X. F. Zhang, R. A. Huggins, and Y. Cui, *Nat. Nanotechnol.*, **3**, 31 (2008).

[28] K. Kang, H. -S. Lee, D. -W. Han, G. -S. Kim, D. Lee, G. Lee, Y. -M. Kang, and M. -H. Jo, *Appl. Phys. Lett.*, **96**, 053110 (2010).

[29] H. Chen, Y. Xiao, L. Wang, and Y. Yang, *J. Power Sources*, **196**, 6657 (2011).

[30] M. -H. Park, K. Kim, J. Kim, and J. Cho, *Adv. Mater.*, **22**, 415 (2010).

[31] T. Jiang, S. Zhang, X. Qiu, W. Zhu, and L. Chen, *Electrochem. Commun.*, **9**, 930 (2007).

[32] Y. Q. Zhang, X. H. Xia, X. L. Wang, Y. J. Mai, S. J. Shi, Y. Y. Tang, C. G. Gu, and J. P. Tu, *J. Power Sources*, **213**, 106 (2012).

[33] R. A. Huggins, *J. Power Sources*, **81-82**, 13 (1999).

[34] H. D. Yoo, E. Markevich, G. Salitra, D. Sharon, and D. Aurbach, *Mater. Today*, **17**, 110 (2014).

[35] E. Peled, *J. Electrochem. Soc.*, **126**, 2047 (1979).

[36] S. Zhang, M. He, C.-C. Su, and Z. Zhang, *Curr. Opin. Chem. Eng.*, **13**, 24 (2016).

[37] X. Song, S. Sun, W. Zhang, H. Yu, and W. Fan, *J. Phys. Chem. B*, **108**, 5200 (2004).

[38] X. Wu, H. Bai, J. Zhang, F. Chen, and G. Shi, *J. Phys. Chem. B*, **109**, 22836 (2005).

[39] R. Rodriguez-Clemente, C. J. Serna, M. Ocana, and E. Matijevic, *J. Cryst. Growth*, **143**, 277 (1994).

[40] W. Zhang, X. Wen, S. Yang, Y. Berta, and Z. L. Wang, *Adv. Mater.*, **15**, 822 (2003).

[41] S. Jin, X. Zhu, and Y. Qian, *Int. J. Electrochem. Sci.*, **9**, 2859 (2014).

[42] X. Jiang, T. Herricks, and Y. Xia, *Nano Lett.*, **2**, 1333 (2002).

[43] Y. Chang, M. L. Lye, and H. C. Zeng, *Langmuir*, **21**, 3746 (2005).

[44] J. Y. Xiang, J. P. Tu, X. H. Huang, and Y. Z. Yang, *J. Solid State Electrochem.*, **12**, 941 (2008).

[45] N. K. Allam, C. A. Grimes, *Mater. Lett.*, **65**, 1949 (2011).

[46] P. Xu, K. Ye, M. Du, J. Liu, K. Cheng, J. Yin, G. Wang, and D. Cao, *RSC Adv.*, **5**, 36656 (2015).

[47] S. M. Pawar, J. Kim, A. I. Inamdar, H. Woo, Y. Jo, B. S. Pawar, S. Cho, H. Kim, and H. Im, *Sci. Rep.*, **6**, 21310 (2016).

[48] Y. Wang, T. Jiang, D. Meng, J. Kong, H. Jia, and M. Yu, *RSC Adv.*, **5**, 16277 (2015).

[49] G.-Q. Yuan, H.-F. Jiang, C. Lin, and S.-J. Liao, *J. Cryst. Growth*, **303**, 400 (2007).

[50] K. V. Gurav, U. M. Patil, S. W. Shin, G. L. Agawane, M. P. Suryawanshi, S. M. Pawar, P. S. Patil, C. D. Lokhande, and J. H. Kim, *J. Alloys Compd.*, **573**, 27 (2013).

[51] D. P. Singh, A. K. Ojha, and O. N. Srivastava, *J. Phys. Chem. C*, **113**, 3409 (2009).

[52] Z. Li, Y. Xin, Z. Zhang, H. Wu, and P. Wang, *Sci. Rep.*, **5**, 10617 (2015).

[53] L. Liu, X. Huang, X. Guo, S. Mao, and J. Chen, *J. Power Sources*, **328**, 482 (2016).

[54] F.-H. Du, Y.-S. Liu, J. Long, Q.-C. Zhu, K.-X. Wang, X. Wei, and J.-S. Chen, *Chem. Commun.*, **50**, 9961 (2014).

[55] C. Wu, J. Maier, and Y. Yu, *Adv. Funct. Mater.*, **25**, 3488 (2015).

[56] D. H. Nam, R. H. Kim, D. W. Han, and H. S. Kwon, *Electrochim. Acta*, **66**, 126 (2012).

[57] C. D. Gu, Y. J. Mai, J. P. Zhou, Y. H. You, and J. P. Tu, *J. Power Sources*, **214**, 200 (2012).

[58] S. T. Chang, I. C. Leu, and M. H. Hon, *Electrochem. Solid-State Lett.*, **5 (8)**, C71 (2002).

[59] S. T. Chang, I. C. Leu, C. L. Liao, J. H. Yen, and M. H. Hon, *J. Mater. Chem.*, **14**, 1821 (2004).

[60] F.-F. Cao, S. Xin, Y.-G. Guo, and L.-J. Wan, *Phys. Chem. Chem. Phys.,* **13**, 2014 (2011).

[61] F.-F. Cao, J.-W. Deng, S. Xin, H.-X. Ji, O. G. Schmidt, L.-J. Wan, and Y.-G. Guo, *Adv. Mater.*, **23**, 4415 (2011).

[62] H. Cheng, Z. G. Lu, J. Q. Deng, C. Y. Chung, K. Zhang, and Y. Y. Li, *Nano Res.*, **3**, 895 (2010).

[63] Q. Deng, Z. Huang, X. Dai, Y. Wang, Z. Li, and J. Li, *J. Solid State Electr.*, **19**, 1765 (2015).

[64] M.-S. Park, G.-X. Wang, Y.-M. Kang, D. Wexler, S.-X. Dou, and H.-K. Liu, *Angew. Chem.*, **119**, 764 (2007).

[65] J. Y. Huang, L. Zhong, C. M. Wang, J. P. Sullivan, W. Xu, L. Q. Zhang, S. X. Mao, N. S. Hudak, X. H. Liu, A. Subramanian, H. Fan, L. Qi, A. Kushima, and J. Li, *Science*, **330**, 1515 (2010).

[66] X. Zhou, L. Yu, and X. W. Lou, *Nanoscale*, **8**, 8384 (2016).

[67] H. Wang, Q. Pan, Q. Wu, X. Zhang, Y. Huang, A. Lushington, Q. Li, and X. Sun, *J. Mater. Chem. A*, **5**, 4576 (2017).

[68] X. Hu, G. Zeng, J. Chen, C. Lu, and Z. Wen, *J. Mater. Chem. A*, **5**, 4535 (2017).

[69] H. Wang, J. Wang, D. Cao, H. Gu, B. Li, X. Lu, X. Han, A. L. Rogach, and C.

Niu, *J. Mater. Chem. A*, **5**, 6817 (2017).

[70] N. Oehl, P. Michalowski, M. Knipper, J. Kolny-Olesiak, T. Plaggenborg, and J.

Parisi, *J. Phys. Chem. C*, **118**, 30238 (2014).

[71] Y. Huang, Q. Pan, H. Wang, C. Ji, X. Wu, Z. He, and Q. Li, *J. Mater. Chem. A*,

4, 7185 (2016).

[72] J. Park, J. Eom, and H. Kwon, *Electrochim. Acta*, **55**, 1825 (2010).

[73] S. Singh, N. Verma, A. Singh, and B. C. Yadav, *Mater. Sci. Semicond. Process.*,

18, 88 (2014).

[74] I. A. Courtney, W. R. McKinnon, and J. R. Dahn, *J. Electrochem. Soc.*, **146 (1)**,

59 (1999).

[75] N. Zhang, Q. Zhao, X. han, J. Yang, and J. Chen, *Nanoscale*, **6**, 2827 (2014).

[76] H.-C. Shin, J. Dong, and M. Liu, *Adv. Mater.*, **15**, 1610 (2003).

[77] W. Zhang, G. Ma, H. Gu, Z. Yang, and H. Cheng, *J. Power Sources*, **273**, 561

(2015).

[78] A. Xiao, S. Zhou, C. Zuo, Y. Zhuan, and X. Ding, *Mater. Res. Bull.*, **70**, 795

(2015).

[79] Q. Zhang, K. Zhang, D. Xu, G. Yang, H. Huang, F. Nie, C. Liu, and S. Yang, *Prog. Mater. Sci.*, **60**, 208 (2014).

[80] Y. Liu, Y. Qiao, W. Zhang, P. Hu, C. Chen, Z. Li, L. Yuan, and X. Hu, *J. Alloy. Compd.*, **586**, 208 (2014).

[81] J. G. Zhao, S. H. Yang, and S. G. Yang, *Cryst. Res. Technol.*, **47**, 1064 (2012).

[82] X. Wang, D.-M. Tang, H. Li, W. Yi, T. Zhai, Y. Bando, and D. Golberg, *Chem. Commun.*, **48**, 4812 (2012).

[83] S. Grugeon, S. Laruelle, R. Herrera-Urbina, L. Dupont, P. Poizot, and J-M. Tarascon, *J. Electrochem. Soc.*, **148 (4)**, A285 (2001).

[84] D. Su, X. Xie, S. Dou, and G. Wang, *Sci. Rep.*, **4**, 5753 (2014).

[85] I. Barycka, I. Zubel, *Sens. Actuators A*, **48**, 229 (1995).

[86] I. Choi, M. J. Lee, S. M. Oh, and J. J. Kim, *Electrochim. Acta*, **85**, 369 (2012).

[87] J. Li, A. K. Dozier, Y. Li, F. Yang, and Y. -T. Cheng, *J. Electrochem. Soc.*, **158**, A689 (2011).

[88] Y. Wang, T. Jiang, D. Meng, H. Jin, and M. Yu, *Appl. Surf. Sci.*, **349**, 636 (2015).

[89] Y. Cudennec, A. Lecerf, *Solid State Sci.*, **5**, 1471 (2003).

[90] W. M. Skinner, C. A. Prestidge, and R. St. C. Smart, *Surf. Interface Anal.*, **24**, 620 (1996).

[91] W. Yang, J. Wang, W. Ma, C. Dong, G. Cheng, and Z. Zhang, *J. Power Sources*, **333**, 88 (2016).

[92] M.-S. Park, Y.-M. Kang, J.-H. Kim, G.-X. Wang, S.-X. Dou, and H.-K. Liu, *Carbon*, **46**, 35 (2008).

[93] A. Jahel, C. M. Ghimbeu, A. Darwiche, L. Vidal, S. H.-Garreau, C. V.-Guterl, and L. Monconduit, *J. Mater. Chem. A*, **3**, 11960 (2015).

[94] X. P. Gao, J. L. Bao, G. L. Pan, H. Y. Zhu, P. X. Huang, F. Wu, and D. Y. Song, *J. Phys. Chem. B*, **108**, 5547 (2004).

[95] Y. Zhao, Y. Zhang, H. Zhao, X. Li, Y. Li, L. Wen, Z. Yan, and Z. Huo, *Nano Res.*, **8**, 2763 (2015).

[96] N. Wan, X. Lu, Y. Wang, W. Zhang, Y. Bai, Y.-S. Hu, and S. Dai, *Sci. Rep.*, **6**, 18978 (2016).

[97] J. Park, J. Eom, and H. Kwon, *Electrochem. Commun.*, **11**, 596 (2009).

[98] D. H. Youn, A. Heller, and C. B. Mullins, *Chem. Mater.*, **28**, 1343 (2016).

[99] L. Yin, S. Chai, F. Wang, J. Huang, J. Li, C. Liu, and X. Kong, *Ceram. Int.*, **42**, 9433 (2016).

[100] J. Zhang, Z. Ma, W. Jiang, Y. Zou, Y. Wang, and C. Lu, *J. Electroanal. Chem.*, **767**, 49 (2016).

[101] Z. Shen, Y. Hu, R. Chen, X. He, Y. Chen, H. Shao, X. Zhang, and K. Wu, *Electrochim. Acta*, **225**, 350 (2017).

[102] T. Zeng, P. Ji, X. Hu, and G. Li, *RSC Adv.*, **6**, 48530 (2016).

[103] R. Liu, W. Su, P. He, C. Shen, C. Zhang, F. Su, and C.-A. Wang, *J. Alloys Compd.*, **688**, 908 (2016).

[104] B. Beverskog, I. Puigdomenech, *J. Electrochem. Soc.*, **144**, 3476 (1997).

국문초록

친환경, 고에너지에 대한 수요가 증가함에 따라 리튬 이온 전지에 대한 연구가 활발히 진행되고 있다. 현재 음극으로 사용되고 있는 흑연 (372 mAh/g)은 다른 음극 활물질에 비해 상대적으로 낮은 이론 용량을 가지고 있어 용량을 향상시킬 수 있는 가능성이 크다. 이를 위해 높은 이론 용량을 가지는 음극 합금 물질에 대한 여러 연구가 진행되어 왔지만, 용량이 큰 만큼 부피 변화에 의한 전극의 퇴화 현상도 심하였다. 활물질의 퇴화 현상을 줄이기 위해 나노 크기의 활물질을 이용하여 절대적인 부피 변화를 줄이는 방법, 완충 물질과 함께 전극을 만들어 발생하는 응력을 감소시키는 방법, 다공성 구조를 만들어 공간을 통해 스트레스를 완화하는 방법 등 많은 연구가 진행되었다. 하지만 이러한 시도 역시 활물질 사이의 접촉을 유지하기 위해 다량의 도전재와 바인더를 첨가해야 해 에너지 밀도를 낮추고, 높은 표면 에너지에 의해 자기 응집이 일어나 입자의 크기가 커지며, 입자 사이의 접촉 수가 많아 접촉 저항이 커져 전기 전도도에 제한적인 단점이 있었다. 본 연구에서는 이러한 나노 크기의 개선 방법의 문제점을 극복하기 위해 마이크로 크기와 나노 크기의 개선 방법 조합해 전지의 성능을 향상시키고자 하였다.

전극의 용량 향상을 위해 합금 물질 중 큰 이론 용량을 보이는 실리콘

(4200 mAh/g)과 주석(994 mAh/g)을 이용하여 전극을 제작하였고, 전극의 특성을 향상시키기 위해 구조적 개선을 진행하였다. 먼저 반도체 공정에서 주로 사용되는 미세전자기계시스템 공정을 이용하여 기판에 마이크로 크기의 톱니 모양과 피라미드 모양의 패턴을 만들고 그 위에 실리콘 활물질을 물리 기상 증착법을 이용하여 필름 형태로 올림으로써 실리콘 활물질의 퇴화를 완화시키고자 하였다. 톱니 모양 패턴과 피라미드 모양 패턴은 전극 표면적을 각각 10%와 40% 증가시켜 전지의 충·방전 시 발생하는 응력을 완화시켰고, 피라미드 모양 패턴 기판을 이용해 제작한 전극의 경우 50번째 사이클까지 약 500 mAh/g의 용량을 유지하였다. 뿐만 아니라 기판에 형성된 패턴의 경우 충·방전동안 기판 모양은 유지되므로 패턴이 지속적으로 응력 완화에 도움을 줄 수 있는 장점이 있었다. 특히 패턴의 오목한 부분에서 활물질의 퇴화 현상이 줄어들었는데, 그 결과 피라미드 모양의 패턴 전극을 사용하여 20번째 사이클에서 실리콘 활물질의 피복률을 약 65%까지 유지하였고 높은 충·방전 속도에서 다른 패턴 전극보다 높은 용량 유지율을 보였다.

　마이크로 크기의 구조 개선뿐만 아니라 나노 와이어 구조를 통한 나노 크기의 구조 개선을 진행하였다. 나노 크기에서는 구조적으로 다루기 힘든 실리콘 대신 음극 활물질로서 주석을 이용하여 실험을 진행하였다.

구리를 산화시키는 방법으로 구리 산화물 나노 와이어 구조를 형성하였고, 전기 도금을 통해 주석/구리 산화물 형태의 나노 와이어 활물질을 제작하였다. 주석뿐만 아니라 구리 산화물 역시 리튬 이온 전지에서 음극 활물질로 사용될 수 있고 다른 도전재나 바인더의 사용 없이 주석이 직접 구리 산화물과 접촉하고 있어 전극에서 에너지 밀도를 향상시킬 수 있었다. 주석/구리 산화물 나노 와이어 전극은 70번째 사이클까지 약 89%의 용량 유지율을 나타내었고, 속도 특성 결과에서도 16 C-rate에서 56%의 용량 유지율을 확인할 수 있었다.

하지만 장기 사이클에서 나노 와이어 구조 전극의 퇴화 현상이 관찰되었다. 200번째 사이클까지 충·방전을 진행할 경우 68%의 용량 유지율을 보였고, 특히 약 100번째 사이클 부근에서 급격한 용량 퇴화가 관찰되었다. 이는 주사전자현미경을 통해 전극 제작 시 압착하는 과정에서 나노 와이어들이 압착되고 눌려져 충·방전동안 나노 와이어의 구조가 허물어지기 때문인 것을 확인하였다. 이러한 문제점을 개선하기 위해 앞서 만들었던 마이크로 크기의 패턴 기판 위에 나노 와이어를 제작하였다. 표면적 증가가 가장 컸던 피라미드 모양 패턴 기판을 사용하여 나노 와이어 구조를 형성하였고, 전지의 충·방전을 진행한 결과 200번째 사이클까지 용량 유지율 92%를 유지하였고 100번째 사이클 부근에서 급격한 전극

퇴화도 보이지 않았다. 이로써, 마이크로 크기와 나노 크기의 조합된 구조 개선을 통해 합금 음극 물질을 이용하여 높은 용량, 향상된 속도 특성 및 장기 특성을 가지는 전극을 성공적으로 얻을 수 있었다.

주요어: 리튬 이온 전지, 음극, 합금 물질, 실리콘, 주석, 기판 구조, 나노 와이어

학 번: 2011-21014

Appendix

Preparation of black pigment with the Couette-Taylor vortex for electrophoretic displays

1. Introduction

Electrophoretic displays (EPDs) are a type of electric paper, which renders the images through the motion of charged pigments. EPDs have been intensively researched because of their advantages: high contrast, wide viewing angle, less eye fatigue, low power consumption, and excellent flexibility [1-13]. EPDs basically consist of two parallel electrodes, a dielectric fluid, and two charged pigments which are white and black. Two kinds of pigments have opposite surface charges, therefore, their corresponding motions under an electric field are exactly opposite. Two main properties of pigments that are important in rendering images in EPDs are zeta potential and density. The zeta potential affects the switching time of a display and the density matched with the dielectric fluid reduces power consumption.

The switching time of an EPD is determined by the speed of the charged pigments under an electric field. The electrophoretic motions of pigments are strongly related to the size and zeta potential of the pigments, the viscosity of the dielectric fluid, and

1 4 7

the magnitude of the electric field [14]. Among these variables, the zeta potential of the pigments is critical in the performance of the EPD. Because the speed under an electric field is a function of the magnitude of the electric field and the zeta potential of charged pigments, a higher zeta potential induces a more rapid movement of the charged pigments [15]. Generally, the zeta potential of a pigment is manipulated by the addition of a charge control agent (CCA), which adsorbs onto the surface of the pigment [16]. The absorption of CCA over carbon black is mediated with a polymer interlayer, thus, a uniform polymer coating on carbon black is important to get the proper zeta potential with small deviation.

The bistability, which determines the stability of an image during the power-off period, could be achieved by controlling the density of the pigments making them identical with that of the dielectric fluid [4]. Because motions caused by gravity do not take place, the images previously rendered by the electric field are maintained when the electric field is turned off. Therefore, additional power is not required to maintain images displayed on an EPD.

In controlling the density of carbon black, which is usually heavier than the dielectric fluid, a polymer coating is usually applied to lower the density of the carbon black. To keep the pigment size uniform, a uniform polymer coating over

carbon black is also important in controlling the density. Generally, polymerization

on carbon black is carried out through two consecutive steps: first the attachment of

a polymerizable functional group on the surface followed by polymerization. Radical

polymerization in the second step has been widely adopted because it is easily carried

out and controls the thickness of the coated polymer which determines the density

of the pigments [17-19]. In many previous studies, polymerization has been

performed in a batch reactor with strong agitation [20,21]. However, in grafting

polymerization performed by a batch reactor, relatively large sizes, wide densities or

size distributions, and low productivity are inevitable. Therefore, the size and density

distributions should be reduced through a uniform polymer coating to obtain better

pigments for EPDs.

   To coat the carbon black uniformly with a polymer for an improved zeta potential

and a uniform density and size, a Couette-Taylor vortex reactor (CTVR) was used

for the polymerization of the pigments' surfaces in this study. A CTVR is a type of

reactor that basically consists of two cylinders shown in Figure 1. During the process,

the inner cylinder is rotated while the outer cylinder is kept stationary, and it

develops the Couette-Taylor vortex between two cylinders. The formation of the

Couette-Taylor vortex can be predicted by Taylor number, $Ta = \Omega(r_o-r_i)^2/\sqrt{2}\nu$, where

Ω is the angular velocity of the inner cylinder, r_o and r_i are the radius of the outer and inner cylinders, and ν is the kinematic viscosity of solution. A Couette-Taylor vortex can be obtained with a Taylor number over 41.19 [22-24]. Because the kinematic viscosity and radii of cylinders are fixed, the rotating speed of the inner cylinder determines the generation of vortex. The axial flow rate, which is the feeding rate of the reactants through the inlet, should be additionally considered to understand the characteristics of the CTVR. Compared to a batch reactor, the Couette-Taylor vortex can intensify the agitation and induce uniform fluidic motion, implying that the mass transfer of the reactant is uniform and enhanced [25-27]. In addition, a high wall shear stress can be obtained, which is expected to improve the dispersion of particles in the solution [28-30]. The agitation and shear stress usually increase with a higher Taylor number in a Couette-Taylor vortex system [31]. Based on these characteristics of the Couette-Taylor vortex, it was expected that the CTVR could reduce the size and density distributions of the polymer-coated pigments. Furthermore, it also improves the productivity because continuous production is possible with the CTVR.

In this study, we investigated the properties of black pigments synthesized in a batch reactor, batch CTVR, and continuous CTVR. The changes in the size, density, and distribution according to CTVR process variables were clarified. In continuous

CTVR, the influence of the axial flow rate was additionally clarified. Finally, we

used the three black pigments obtained from each process in EPDs with white TiO_2

particles, and the response times under the electric field were compared.

Couette-Taylor vortex

inlet

axial flow

outlet

Ω

r_i

r_o

rotating
inner cylinder

stationary outer cylinder
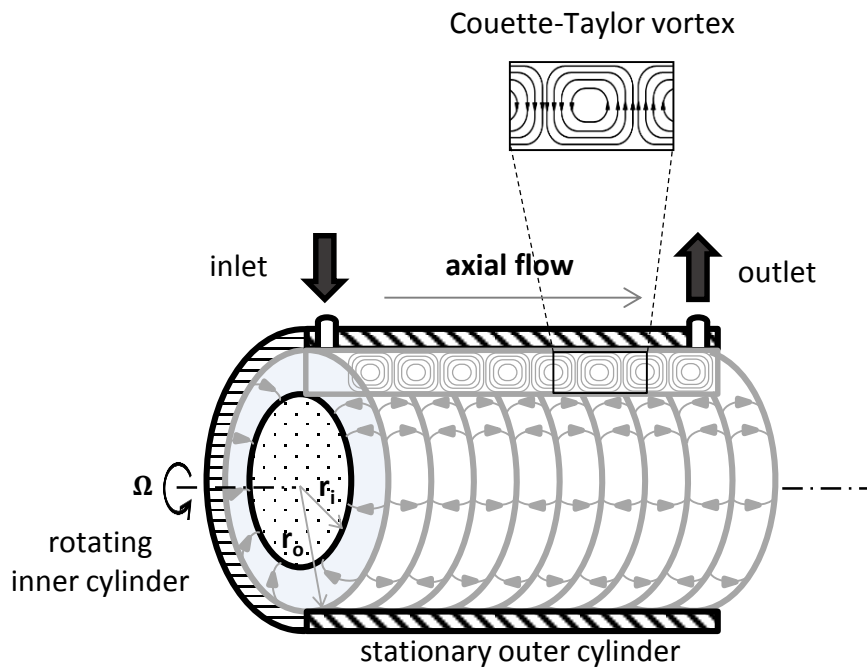
Figure 1. The schematic diagram of the Couette-Taylor vortex reactor (CTVR). r_i, r_o,

and Ω are the radius of the inner and outer cylinders, and angular velocity of the

inner cylinder, respectively.

2. Experimental

The polymerization step used in this study is shown in Figure 2. The initial attachment of a polymerizable functional group (step 1) was performed in a batch reactor, followed by polymerization (step 2) which was done in three different reactors: a batch reactor, batch CTVR, and continuous CTVR.

18.7 g of carbon black (Degussa, printex L6) was dispersed in 400 ml of de-ionized water. To attach 4-vinylaniline onto the surface of the carbon black (step 1), 0.8 ml of hydrochloric acid (HCl, SAMCHUN, 37%) and 0.4 g of 4-vinylaniline (Sigma Aldrich, 97%) were added. After heating the solution up to 40°C, 1.3 ml of aqueous solution containing 2.52 M of sodium nitrite ($NaNO_2$, Sigma Aldrich) was slowly added for 10 minutes followed by stirring for 16 hours [32]. The amine group in 4-vinylaniline reacts with sodium nitrite under acidic condition, forming diazonium ion. 4-vinylaniline attaches to the surface of carbon black through the reaction between diazonium ion and the nucleophilic group on the surface of carbon black. The double bond in attached 4-vinylaniline is an initiation site for further polymerization in step 2. After that, the solution was centrifuged at 8,000 rpm for 20 minutes with acetone (SAMCHUN, 99.5%) to collect the pretreated carbon black and eliminate unreacted reagents. This step was repeated two times, and the collected

carbon black was dried for 12 hours at 40°C under vacuum condition.

Regardless of the type of reactor, the polymerization (step 2) was performed with toluene (DAEJUNG, 99.5%) solution containing the pretreated carbon black, 2-ethylhexyl acrylate (EHA, Sigma Aldrich, 98%), and azobisisobutyronitrile (AIBN, SAMCHUN, 98%). The concentrations of carbon black, EHA, and AIBN were 100 g/l, 2.88 M, and 0.032 M, respectively. The temperature of solution was maintained at 70°C with a thermostat. After the polymerization reaction was completed, tetrahydrofuran (THF, DAEJUNG, 99%) was added, and the mixture was centrifuged at 10,000 rpm for 20 minutes. The collected black pigments were rinsed with acetone. The centrifuging and rinsing steps were repeated twice.

The total volume of solution for step 2 was 144 ml for the batch reactor and the batch CTVR. Agitation was applied by an overhead stirrer with a rotating speed of 300 rpm for the batch reactor. As mentioned above, agitation of CTVR was achieved by rotating the inner cylinder, and the rotating speeds were 30, 60, 90, and 300 rpm and the corresponding Taylor numbers were 304, 608, 911, and 3036, respectively. Both reactors had a fixed reaction time of 1 hr for step 2.

In the case of the continuous CTVR, the axial flow rates were 1.8, 2.4, and 3.6 ml/min with a fixed rotating speed of 300 rpm. The residence time in the reactor was

determined by the axial flow rate. Initially, the CTVR was filled with solution for step 2, and the products were collected according to the residence time. Because the total volume of the CTVR was 144 ml, the residence times were 80, 60, and 40 min for 1.8, 2.4, and 3.6 ml/min of the axial flow rate, respectively. When the collection time is below the residence time, the reaction time was identical to the collection time. In contrast, the reaction time was identical to the residence time when the collection time is over the residence time.

The density, size distribution, zeta potential and functional group of the pigment surface after polymerization, were investigated to characterize the synthesized black pigments. The average density of the black pigments was inspected by a gas pycnometer (AccuPyc II 1340, Micromeritics), and the surface functional group was investigated with a FT-IR spectrophotometer (Nicolet 6700, Thermo Scientific). The size and distribution, and the zeta potential were measured by a zeta-potential & particle size analyzer (ELS-Z, OTSUKA).

Finally, the synthesized black pigments were used in EPDs. The white pigment was a polymer-coated TiO_2, which was fabricated following the procedures reported by our group [9]. The slurry solution for the EPD consisted of 6 mg/ml of synthesized black pigment, and 120 mg/ml of white pigment with 0.25 wt% of Span 80 (Sigma

Aldrich) in tetrachloroethylene (TCE, Sigma Aldrich, 99%). 20 μl of slurry solution

was placed between two ITO electrodes, and the gap between two electrodes was

fixed to 60 μm. The color changes were investigated by applying electric field using

a power supply (PWS-3005D, JEILMI), and the response times of the electrophoretic

display were compared with a video microscope (SV-35, SOMETECH).
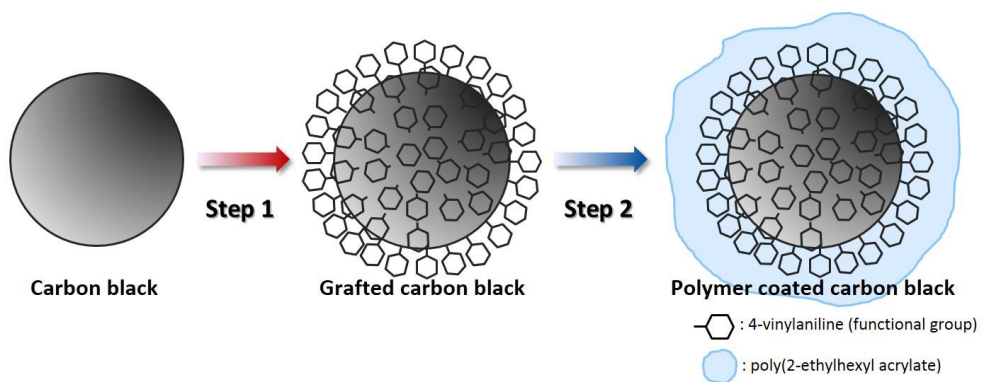
Figure 2. A schematic diagram of polymerization on carbon black used in this study.

3. Results and Discussion

To investigate the influences of strong agitation and uniform fluidic motion driven by the CTVR, the properties of black pigment such as the density, size, and size distribution after polymerization (step 2) were compared. Figure 3 exhibits the size distribution and density of the black pigments synthesized by the batch reactor and batch CTVR, highlighting that the size and density decreased with the CTVR. The densities and average sizes were 1.81 g/cm^3 and 422 ± 43 nm for batch reactor and 1.63 g/cm^3 and 293 ± 21 nm for the batch CTVR. An enhanced dispersion led to the decrease in the size of carbon black by inhibiting agglomeration. This was supported by the size distribution of the polymerized carbon black shown in Figure 3 (a).

The polymerization reaction in step 2 takes place in solution, thus, the polymerization could happen following two pathways, i.e. homogeneous polymerization, or polymerization on the surface of the carbon black covered by a polymerizable functional group. The selectivity of this polymerization step is determined by the ratio between the total surface area of the carbon black for polymerization and the concentration of EHA. That is, when the active area was increased due to the improved dispersion, polymerization occurred selectively on the surface. In contrast, homogeneous polymerization was dominant in the agglomerated

carbon blacks. Therefore, the decrease in the density with the CTVR observed in

Figure 3 (b) was originated from the improvement of carbon black dispersion by

uniform fluidic motion.

Figure 4 displays the size distribution and density of the black pigments with

varying angular velocities of the inner cylinder, and the corresponding Taylor

number (at the upper y-axis in Figure 4 (b)). The acceleration of the inner cylinder,

corresponding to a higher value of the Taylor number, signified the rapid motion of

the vortex without a change in the size of the vortex [33]. Figure 4 (a) indicates that

a higher angular velocity reduced the size of the black pigments by improving the

dispersion of the carbon black. The average sizes were 402 ± 58, 362 ± 25, 327 ± 24,

and 293 ± 21 nm for angular velocities of 30, 60, 90, and 300 rpm, respectively. The

variation in density according to angular velocity, exhibited in Figure 4 (b), could

also be explained by the enhanced dispersion as interpreted in the previous paragraph.

The increase in the Taylor number signified a more intense fluidic motion, leading

to a larger active area for polymerization from the enhanced dispersion of carbon

black. It induced the high selectivity of polymerization on the surface of carbon black

with diminishing the heterogeneous polymerization, which finally resulted in a

reduction in the density. The black pigments synthesized with an angular velocity of

300 rpm were used for further experiments.

Continuous CTVR is an effective way to supplement the low productivity of the batch system, therefore, the effects of continuous CTVR during the polymerization step on carbon black were clarified. As mentioned above, the axial flow rate, i.e. the feeding rate, determined the residence time as well as the productivity of continuous CTVR. Prior to the reaction, the reactor was filled with a solution, which was identical to the feeding solution, and then, the experiments were performed with axial flow rate of 3.6, 2.4, and 1.8 ml/min. 20 ml of the product solution was sampled at designated collection times to measure the properties of the black pigments.

The changes in the size and density of the black pigments according to the axial flow rate and the collection time are shown in Figure 5. The size distribution of the carbon black collected over the residence time is shown in Figure 5 (a). It was clearly observed that the size of the black pigment was reduced with a low axial flow rate, and the average particle sizes were 510 ± 53, 402 ± 33, and 381 ± 30 nm for 3.6, 2.4, and 1.8 ml/min of axial flow rate, respectively.

In Figure 5 (b), the changes in the density of black pigments are shown, indicating that the density was varied according to the axial flow rate and collection time. Regardless of the axial flow rate, the density was initially decreased as the collection

time increased. This was due to an insufficient reaction time for the polymerization when the collection time was below the residence time. After the residence time, the densities of the black pigments were converged at 1.70, 1.64, and 1.62 g/cm^3 with axial flow rate of 3.6, 2.4, and 1.8 ml/min, respectively. It is obvious that the saturation density is reduced with low axial flow rate. In addition, it is important to notice that the density is converged before the residence time is reached. This signifies the completion of polymerization before the residence time. Considering this along with the changes in the saturation density and sizes shown in Figure 5, it is reasonable to suggest that the axial flow rate also affects the dispersion of carbon black and polymerization. If there is no effect from the axial flow rate, the density should be saturated exactly at the residence time, and the density and size should be similar to those from the batch CTVR. Based on these results, it can be concluded that the axial flow had a negative effect on the dispersion of carbon black. It was possible that the axial flow rate distorted Couette-Taylor vortex, and it led to the increment of pigment's density and size. Although the density and size from the continuous CTVR were higher than those of the batch CTVR, it was obvious that those were relatively small compared to the results of the batch reactor. Therefore, it is important to note that black pigments with better properties could be synthesized

at a high productivity with continuous CTVR compared to the conventional batch reactor.

Prior to using the black pigments in EPDs, the surface chemistry was investigated by FT-IR because the modification of fluidic motion had a potential to change the reaction path of the polymerization. The FT-IR spectra of EHA monomer and carbon blacks before and after polymerization are exhibited in Figure 6. In the case of the EHA monomer, peaks corresponding to the ester group and hydrocarbons were confirmed near 1730-1750 cm^{-1} and 2800-2900 cm^{-1}. After the polymerization, the peaks related to the ester group and hydrocarbon appeared regardless of the reactors. This implies that the reaction path was not altered by the change in the fluidic motion, and the surface chemistry of the synthesized carbon black was identical. It was ascertained that the variation in fluidic motion only affects the size of the synthesized black pigments under the conditions we investigated.

In addition to the surface chemistry, the bistability of the synthesized black pigments was investigated, and the results are shown in Figure 7. A solution consisting of TCE and CCA was used to assess the dispersion. The density of TCE was 1.62 g/cm^3, and those of the black pigments were 1.81, 1.63, and 1.62 g/cm^3 obtained from the batch reactor, batch CTVR (300 rpm), and continuous CTVR (1.8

ml/min, 300 rpm), respectively. The images, taken one day after the sonication, indicate that all of polymer-coated black pigments were well-dispersed in the solution while the carbon black with a density of 2.1 g/cm^3 sank to the bottom. The results prove that the carbon black prepared with CTVR has acceptable bistability when its density is properly controlled to that of the dielectric fluid.

Finally, the movement of the black pigments under an electrical field was observed with the addition of a white TiO_2 pigment. The zeta potentials of three black pigments were 3.68 ± 12.61 mV (batch CTVR), -2.18 ± 13.87 mV (continuous CTVR), and -21.89 ± 15.32 mV (batch reactor), and that of polymer-coated TiO_2 was -68.87 ± 14.12 mV. The representative images according to the direction of the electric field are shown in Figure 8. White and black colors were successfully achieved in this system. To compare the movement speed of three black pigments, the switching times were measured and it was confirmed that the response times were in the order of batch CTVR (1.21 s) < continuous CTVR (1.26 s) < batch reactor (1.42 s), which was identical to the expectation from the size, uniformity of the polymerization and the zeta potential. The adsorption of charge control agent and following zeta potential variation were also affected by the size and uniformity of polymer-coated carbon black. The combination of black and white having the largest

difference in zeta potential demonstrated the fastest response time among three

combinations we investigated.

(a)

(b)
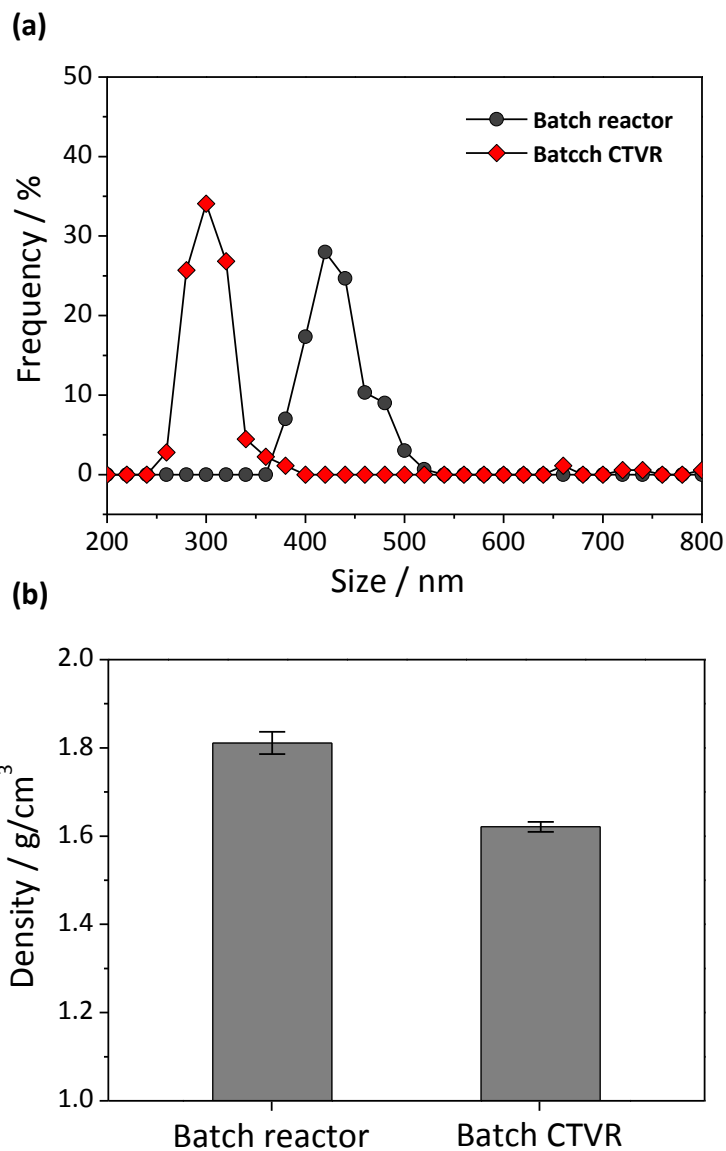
Figure 3. (a) The size distribution and (b) density of polymer-coated carbon black

from the batch reactor and batch CTVR. The angular velocity of the inner cylinder

in the CTVR was 300 rpm, and the reaction time was 1 hr for all reactors.
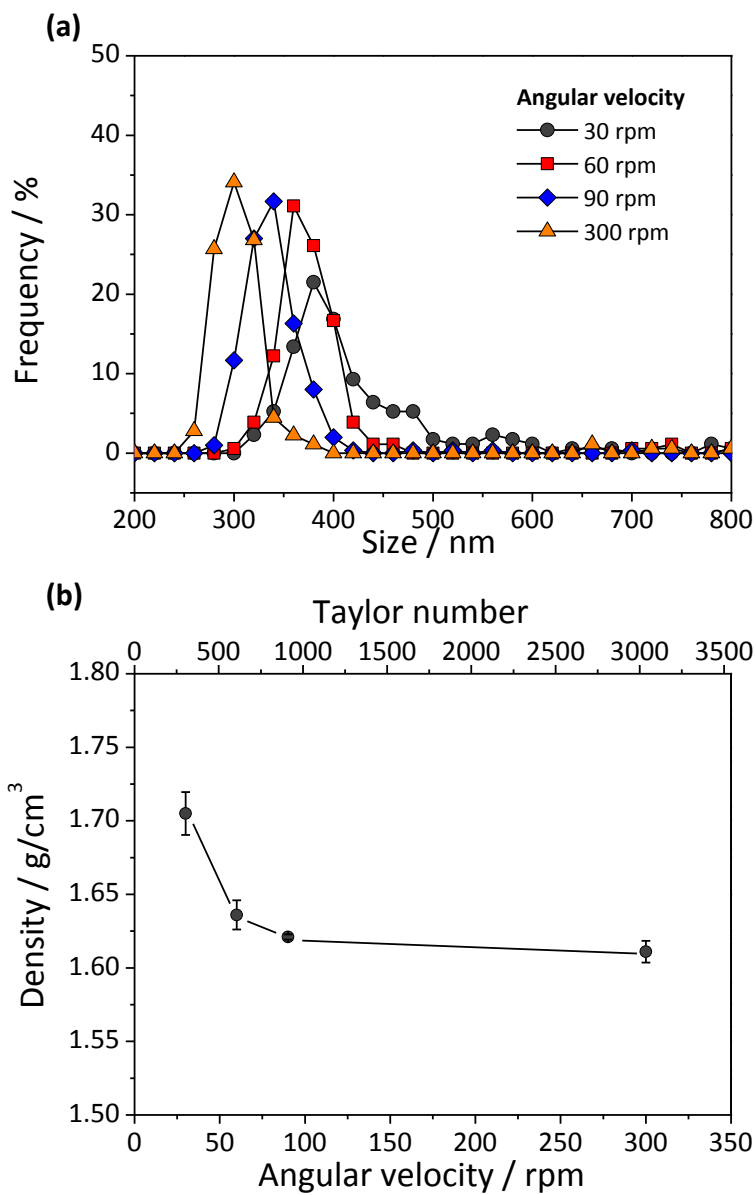
Figure 4. The changes in (a) the size distribution and (b) density of the polymer-coated carbon black obtained by batch CTVR according to the angular velocity. The reaction time was 1 hr.
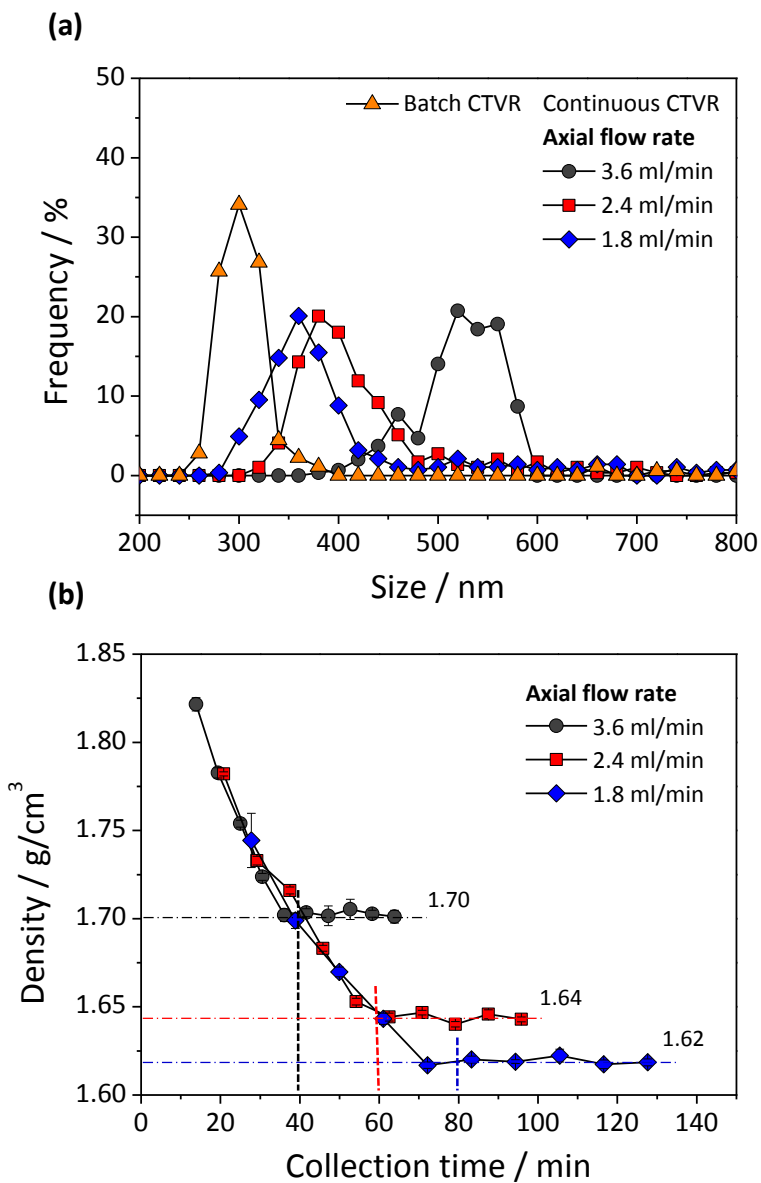
Figure 5. The changes in (a) the size distribution and (b) density of the polymer-

coated carbon black fabricated by continuous CTVR according to the collection time

and axial flow rate. The collection times for black pigments in (a) were 40, 60, and

80 min for axial flow rates of 3.6, 2.4, and 1.8 ml/min, respectively. The vertical dash

lines in (b) indicate the residence times, and the horizontal dash-dot lines point out

the converged average density of the black pigments.
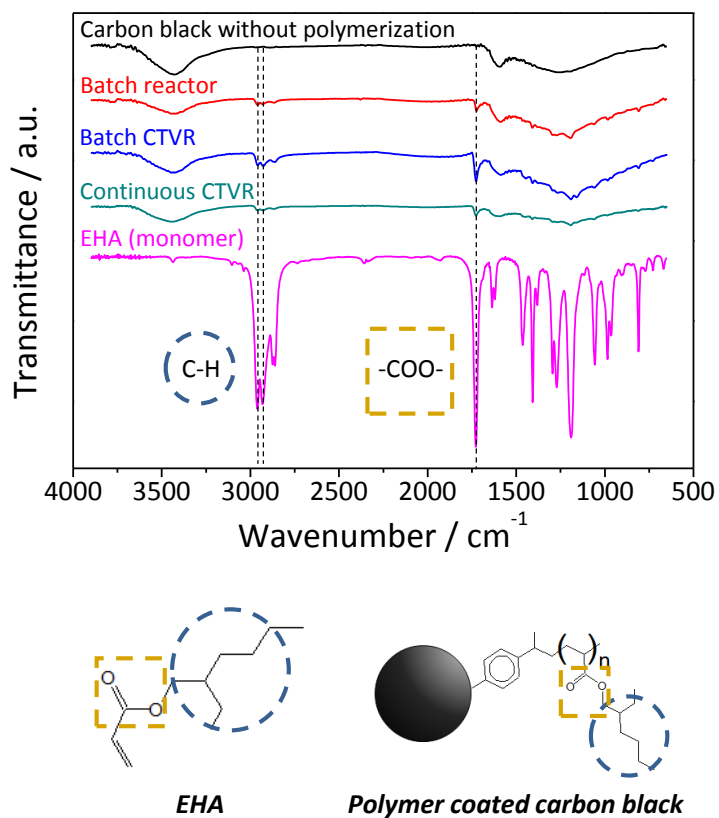
Figure 6. FT-IR spectra of the bare and polymer-coated carbon black; the polymerizations were performed in a batch reactor and CTVR. The polymerizations in CTVR were performed under batch and continuous conditions. The angular velocity of the inner cylinder for CTVR was fixed to 300 rpm. The axial flow rate of the continuous CTVR was 1.8 ml/min, and the collection time was 80 min.
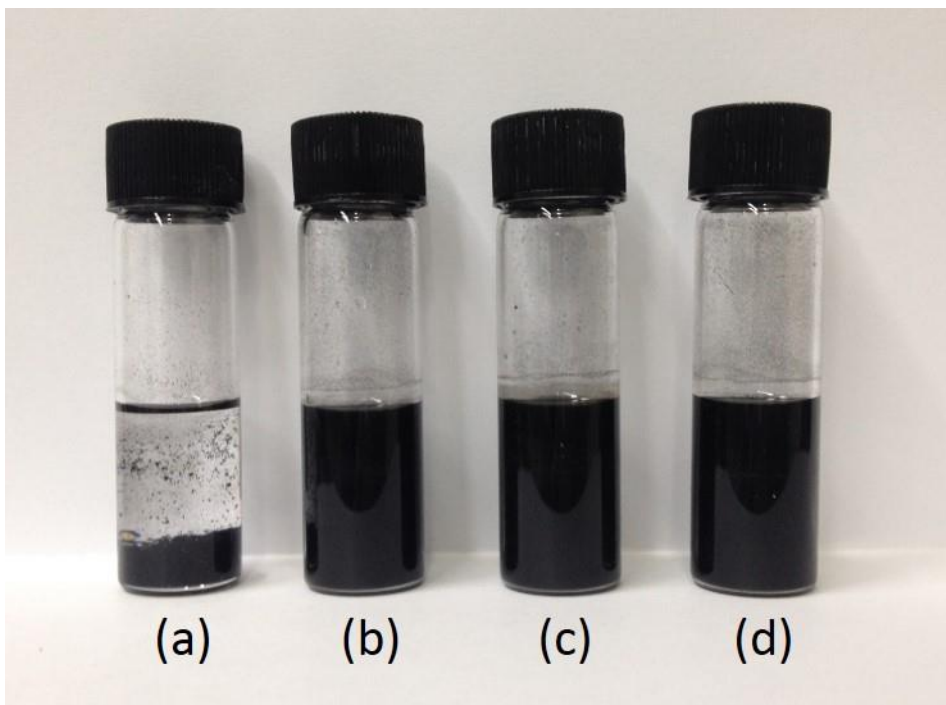
Figure 7. The dispersion of (a) bare carbon black, and polymer-coated carbon black

from (b) the batch reactor, (c) batch CTVR, and (d) continuous CTVR. The black

pigments were dispersed in TCE containing 0.25 wt% of Span 80. The black

pigments were identical to that used in Figure 6.
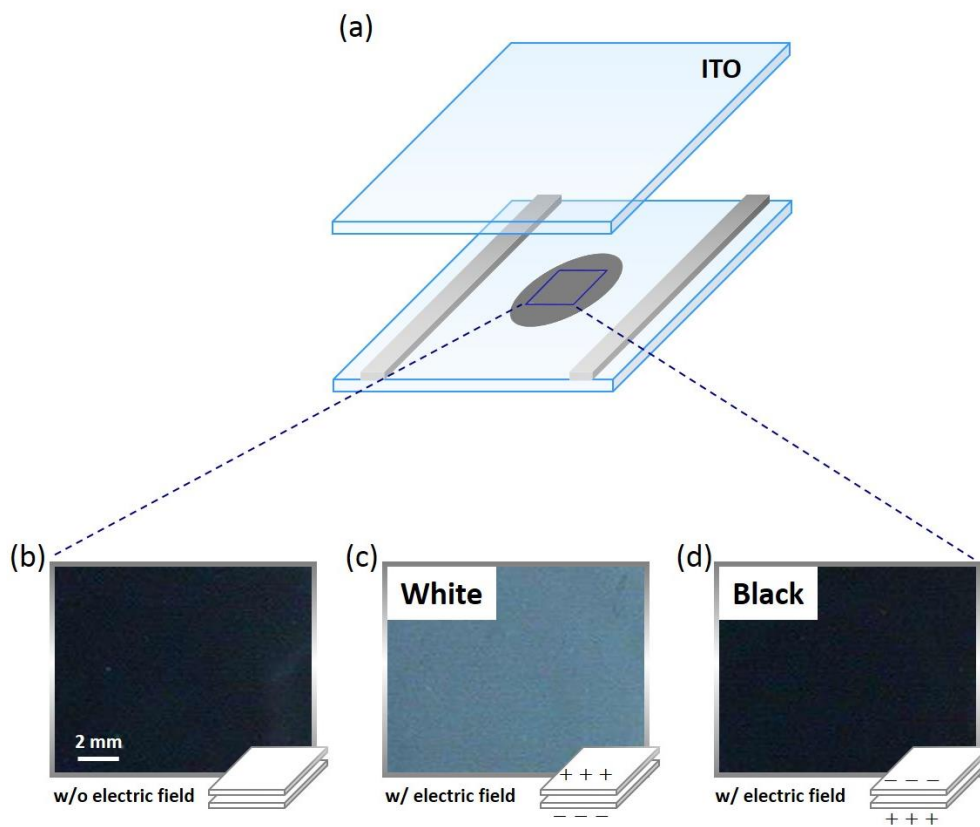
Figure 8. (a) Schematic diagram of the dual particle system and the electrophoretic images (b) without and with electric fields; (c) upper: (+), lower: (-) and (d) upper: (-), lower: (+). The black pigments were synthesized by means of continuous CTVR, and the white pigments were polymer-coated TiO_2 particles. The applied voltage and gap between upper and lower electrodes were 30 V and 60 μm, respectively.

4. Conclusions

In this research, the Couette-Taylor vortex was applied to the polymerization of black pigment for use in EPDs. The influences of variables such as the angular velocity and axial flow rate of CTVR on the size and density of black pigments were clarified. It was confirmed that the high angular velocity of the inner cylinder reduced the size and density, originated from the improved dispersion of the carbon black. The axial flow rate caused a slight increase in the size and density, however, those were still better compared to that obtained from the batch reactor. The reduction of size and density resulted in the amelioration of the black pigment′s movement under an electric field with excellent bistability. Furthermore, the usage of continuous CTVR increased the productivity and improved the properties of the black pigments compared to a conventional batch reactor.

References

[1] T. Bert, H. D. Smet, F. Beunis, and K. Neyts, *Displays*, **27**, 50 (2006).

[2] Y. Chen, J. Au, P. Kazlas, A. Ritenour, H. Gates, and M. McCreary, *Nature*, **423**, 136 (2003).

[3] C.-J. Chung, J.-H. Jean, *J. Am. Ceram. Soc.*, **90**, 3490 (2007).

[4] B. Comiskey, J. D. Albert, H. Yoshizawa, and J. Jacobson, *Nature*, **394**, 253 (1998).

[5] C. A. Kim, M. J. Joung, S. D. Ahn, G. H. Kim, S.-Y. Kang, I.-K. You, J. Oh, H. J. Myoung, K. H. Baek, and K. S. Suh, *Synth. Met.*, **151**, 181 (2005).

[6] J. Y. Kim, J.-Y. Oh, and K.-S. Suh, *Carbon*, **66**, 361 (2014).

[7] K. U. Lee, K. J. Park, O. J. Kwon, and J. J. Kim, *Curr. Appl. Phys.*, **13**, 419 (2013).

[8] S. W. Oh, C. W. Kim, H. J. Cha, U. Pal, and Y. S. Kang, *Adv. Mater.*, **21**, 4987 (2009).

[9] K. J. Park, K. U. Lee, M. H. Kim, O. J. Kwon, and J. J. Kim, *Curr. Appl. Phys.*, **13**, 1231 (2013).

[10] H. H. Sim, Y. J. Kim, and H. J. Choi, *J. Nanosci. Nanotech.*, **12**, 9254 (2012).

[11] C. Sun, Y.-Q. Feng, B. Zhang, X.-G. Li, J.-Z. Shao, J.-J. Han, and X. Chen, *Opt. Mater.*, **35**, 1410 (2013).

[12] G. Yin, Z. Zheng, H. Wang, and Q. Du, *J. Colloid Interface Sci.*, **361**, 456 (2011).

[13] Q. Zhao, T. Tan, P. Qi, S. Wang, S. Bian, X. Li, Y. An, and Z. Liu, *Appl. Surf. Sci.*, **257**, 3499 (2011).

[14] B. J. Yoon, *J. Colloid Interface Sci.*, **142**, 575 (1990).

[15] M. N. Patel, P. G. Smith Jr., J. Kim, T. E. Milner, and K. P. Johnston, *J. Colloid Interface Sci.*, **345**, 194 (2010).

[16] B. J. Park, S. Y. Hong, H. H. Sim, H. J. Choi, and Y. S. Yoon, *Mater. Chem. Phys.*, **135**, 259 (2012).

[17] K. U. Lee, K.J. Park, M. H. Kim, O. J. Kwon, and J. J. Kim, *Dyes Pigment.*, **102**, 22 (2014).

[18] K. Ohkita, N. Tsubokawa, E. Saitoh, and M. Noda, *Carbon*, **13**, 443 (1975).

[19] W. Wang, Z. Dong, P. Xia, D. Yan, and Q. Zhang, *Macromol. Rapid Commun.*, **19**, 647 (1998).

[20] T. Liu, S. Jia, T. Kowalewski, and K. Matyjaszewski, *Langmuir*, **19**, 6342 (2003).

[21] S. Yoshikawa, S. Machida, and N. Tsubokawa, *J. Polym. Sci. pol. chem.*, **36**, 3165 (1998).

[22] P. R. N. Childs, 2011. Rotating flow. Elsevier, Burlington.

[23] M. C. Kim, C. K. Choi, *Korean J. Chem. Eng.*, **23**, 874 (2006).

[24] C. B. Shin, C. K. Choi, *Korean J. Chem. Eng.*, **1**, 83 (1984).

[25] R. J. Campero, R. D. Vigil, *Chem. Eng. Sci.*, **52**, 3303 (1997).

[26] K. Kataoka, N. Ohmura, M. Kouzu, Y. Simamura, and M. Okubo, *Chem. Eng. Sci.*, **50**, 1409 (1995).

[27] X. H. Zhu, D. Y. Arifin, B. H. Khoo, J. Hua, and C.-H. Wang, *Chem. Eng. Sci.*, **65**, 2108 (2010).

[28] L. S. Fellay, M. Vanni, *J. Colloid Interface Sci.*, **388**, 47 (2012).

[29] M. Kristiawan, T. Jirout, and V. Sobolik, *Exp. Therm. Fluid Sci.*, **35**, 1304 (2011).

[30] C. Pomchaitaward, I. Manas-Zloczower, and D. L. Feke, *Chem. Eng. Sci.*, **58**, 1859 (2003).

[31] K. Watanabe, S. Sumio, and S. Ogata, *J. Fluids Eng.-Trans. ASME.*, **128**, 95 (2006).

[32] M. Delamar, R. Hitmi, J. Pinson, and J. M. Saveant, *J. Am. Chem. Soc.*, **114**, 5883 (1992).

[33] E. Dumont, F. Fayolle, V. Sobolik, and J. Legrand, *Int. J. Heat Mass Transf.*, **45**, 679 (2002).

CURRICULUM VITAE

Myeongho Kim

Electronics Processing Research Laboratory

School of Chemical and Biological Engineering, Seoul National University

Republic of KOREA

Personal Information		Office Address
Name:	Myeongho Kim	#302-907, College of Engineering
Date of Birth:	September 20, 1988	Seoul National University
Place of Birth:	Jinhae, Korea	1 Gwanak-ro, Gwanak-gu, Seoul 08826,
Nationality:	Republic of Korea	Republic of Korea
Sex:	Male	Tel: +82-2-880-8940
		E-mail: moungho17@snu.ac.kr

EDUCATION

Doctor of Philosophy (March 2011 ~ August 2017)

    School of Chemical and Biological Engineering, Seoul National University

    Advisor: Prof. Jae Jeong Kim

    Thesis: "Structural Refinement Using Nanowire and Micro-patterned Substrate for Si- or Sn-based Li-alloying Material in Li-ion Batteries"

Bachelor of Engineering (March 2007 ~ February 2011)

    School of Chemical and Biological Engineering, Seoul National University

ACADEMIC ACTIVITIES

2010-present	Korea Institute of Chemical Engineering, Student member
2017-present	The Korean Society of Industrial and Engineering Chemistry, Student member
2013-2016	The Korean Electrochemical Society, Student member
2014-2015	The Electrochemical Society (USA), Student member
2011.9-2011.12	Teaching Assistant: Heat and Mass Transfer
2012.9-2012.12	Teaching Assistant: Chemical and Biological Process Lab.
2013.3-2013.6	Teaching Assistant: Chemical and Biological Process Lab.
2014.9-2014.12	Teaching Assistant: Chemical and Biological Process Lab.

ACCOMPLISHMENT

-International Journal-

[1] <u>Myeongho Kim</u>, Kyung Ju Park, Kang Uk Lee, Myung Jun Kim, Woo-Sik Kim, Oh Joong Kwon, and Jae Jeong Kim, "Preparation of black pigment with the Couette-Taylor vortex for electrophoretic displays", Chemical Engineering Science, 119, 245-250 (2014)

[2] <u>Myeongho Kim</u>, Min Jeong Lee, Insoo Choi, and Jae Jeong Kim, "Sawtooth- or Pyramidal-Patterned Si Negative Electrode Fabricated by MEMS for Li-Ion Secondary Battery", Bulletin of the Korean chemical society, 37, 1747-1753 (2016)

[3] <u>Myeongho Kim</u>, Insoo Choi, and Jae Jeong Kim, "Hetero-structured CuO nanowire decorated with Sn as a highly stable anode material for Li-ion batteries", (submitted)

[4] Kyung Ju Park, Kang Uk Lee, <u>Myeong Ho Kim</u>, Oh Joong Kwon, and Jae Jeong Kim, "Preparation of PS/TiO_2 as a white pigment for electrophoretic displays", Current Applied Physics, 13, 1231-1236 (2013)

[5] Kang Uk Lee, Myung Jun Kim, Kyung Ju Park, <u>Myeongho Kim</u>, Oh Joong Kwon, and Jae Jeong Kim, "Catalytic growth of a colloidal carbon sphere by hydrothermal reaction with iron oxide (Fe_3O_4) catalyst", Materials Letters, 125, 213-217 (2014)

[6] Jongwoo Park, Insoo Choi, Min Jeong Lee, <u>Myeong Ho Kim</u>, Taeho Lim, Kern

H. Park, Jihyun Jang, Seung M. Oh, Sung Ki Cho, and Jae Jeong Kim, "Effect of fluoroethylene carbonate on electrochemical battery performance and the surface chemistry of amorphous MoO_2 lithium-ion secondary battery negative electrodes", Electrochimica Acta, 132, 338-346 (2014)

[7] Kang Uk Lee, Kyung Ju Park, Myeong Ho Kim, Oh Joong Kwon, and Jae Jeong Kim, "Preparation of the carbon sphere coated with iron oxide and tis application for electronic paper", Dyes and Pigments, 102, 22-28 (2014)

[8] Insoo Choi, Sang Hyun Ahn, Myeong Ho Kim, Oh Joong Kwon, and Jae Jeong Kim, "Synthesis of an active and stable Pt_{shell}-Pd_{core}/C catalyst for the electro-oxidation of methanol", International Journal of Hydrogen Energy, 39, 3681-3689 (2014)

[9] Kang Uk Lee, Myung Jun Kim, Kyung Ju Park, Myeongho Kim, and Jae Jeong Kim, "Mobility of black pigments for electrophoretic display depending on the characteristics of carbon sphere", Dyes and Pigments, 121, 276-281 (2015)

[10] SungKyung Kim, Myeongho Kim, Insoo Choi, and Jae Jeong Kim, "Quercetin as electrolyte additive for $LiNi_{0.5}Mn_{1.5}O_4$ cathode for lithium-ion secondary battery at elevated temperature", Journal of Power Sources, 336, 316-324 (2016)

-Conference-

International

[1] Myeongho Kim, Kyung Ju Park, Kang Uk Lee, Myung Jun Kim, Oh Joong Kwon, and Jae Jeong Kim, "Black pigment preparation via Couette-Taylor vortex for electrophoretic display application", 226th Meeting of the Electrochemical Society (ECS) and SMEQ Joint International Meeting, Cancun, Mexico, 2014

[2] Myeongho Kim, Sungkyung Kim, Myung Jun Kim, Insoo Choi, and Jae Jeong Kim, "The structure modification of substrate for alloying materials in Li-ion secondary battery", Pacific Rim Meeting (PRiME) 2016, Hawaii, United States of America, 2016

[3] Kang Uk Lee, Kyung Ju Park, Myung Ho Kim, Oh Joong Kwon, and Jae Jeong Kim, "Research of B/W particles in electrophoretic display", The 64th Annual

Meeting of the International Society of Electrochemistry (ISE), Queretaro, Mexico, 2013

Domestic

[1] Myeong Ho Kim, Oh Joong Kwon, Kyung Ju Park, Kang Uk Lee, and Jae Jeong Kim, "Preparation of black pigment using radical polymerization with Couette-Taylor vortex in electrophoretic display", The Korean Institute of Chemical Engineers Spring Meeting, Jeju, 2012

[2] Myeong Ho Kim, Oh Joong Kwon, Kyung Ju Park, Kang Uk Lee, and Jae Jeong Kim, "Synthesis of black pigment with Couette-Taylor vortex for electrophoretic display application", The Korean Institute of Chemical Engineers Fall Meeting, Busan, 2012

[3] Myeong Ho Kim, Kyung Ju Park, Kang Uk Lee, Oh Joong Kwon, and Jae Jeong Kim, "Synthesis of Black Pigment Using Radical Polymerization with Couette-Taylor Vortex in Electrophoretic Display", The Korean Institute of Chemical Engineers Fall Meeting, Daegu, 2013

[4] Myeongho Kim, Sungkyung Kim, Insoo Choi, and Jae Jeong Kim, "Sawtooth- or pyramidal-patterned Si electrode fabricated by MEMS process for Li-ion battery", The Korean Electrochemical Society Spring Meeting, Gwangju, 2016

[5] Myeongho Kim, Insoo Choi, and Jae Jeong Kim, "Electrochemical synthesis of Sn/CuO nanowires for high performance anode in Li-ion batteries", The Korean Society of Industrial and Engineering Chemistry Spring Meeting, Gwangju, 2017

[6] Min Jeong Lee, Insoo Choi, Jongwoo Park, Myeong Ho Kim, and Jae Jeong Kim, "Si thin film negative electrode fabricated by MEMS process for Li-ion secondary batteries", The Korean Electrochemical Society Spring Meeting, Changwon, 2013

[7] Jongwoo Park, Insoo Choi, Min Jeong Lee, Myeong Ho Kim, Kern H. Park, Seung M. Oh, and Jae Jeong Kim, "Effects of additive on the performance and surface chemistry of amorphous MoO_2 lithium-ion secondary battery negative electrodes", The Korean Electrochemical Society Spring Meeting, Changwon, 2013

[8] Jongwoo Park, Insoo Choi, Min Jeong Lee, Myeong Ho Kim, Kern H. Park, Seung M. Oh, and Jase Jeong Kim, "Additive effects on the electrochemical property

of amorphous MoO_2 negative electrode for lithium-ion secondary batteries", The Korean Institute of Chemical Engineers Spring Meeting, Changwon, 2013

[9] Sungkyung Kim, Myeongho Kim, Myung Jun Kim, and Jae Jeong Kim, "The effect of Quercetin on $LiNi_{0.5}Mn_{1.5}O_4$ positive electrode as an electrolyte additive in Li-ion secondary batteries", The Korean Institute of Chemical Engineers Spring Meeting, Jeju, 2015

[10] Sungkyung Kim, Myeongho Kim, Myung Jun Kim, and Jae Jeong Kim, "The effect of Quercetin as an electrolyte additive on $LiNi_{0.5}Mn_{1.5}O_4$ cathode in Li-ion batteries", The Korean Electrochemical Society Spring Meeting, Gwangju, 2015

[11] Sungkyung Kim, Myeongho Kim, Insoo Choi, and Jae Jeong Kim, "Improvement in cycle life of $LiNi_{0.5}Mn_{1.5}O_4$ cathode for lithium-ion secondary batteries by employing quercetin as an electrolyte additive at the elevated temperature", The Korean Electrochemical Society Spring Meeting, Gwangju, 2016

[12] Tae Young Kim, Hoe Chul Kim, Myeongho Kim, Yu Seok Ham, Youngkeun Jeon, and Jae Jeong Kim, "Effect of acidity on the change in additives chemistry and Cu metallization", The Korean Institute of Chemical Engineers Spring Meeting, Busan, 2016

-Patent-

[1] Insoo Choi, Jae Jeong Kim, Myeongho Kim, and Sungkyung Kim, "A Method for Improving Cycle Life of Cathode for Lithium-Ion Secondary Batteries at the Elevated Temperature and a composition therefor", application number 10-2016-0100085

[2] Insoo Choi, Jae Jeong Kim, Myeongho Kim, and Sungkyung Kim, "LETHIUM BATTERY AND METHOD FOR MANUFACTURING ELECTRODE OF THE LITHIUM BATTERY", application number 10-2016-0135215